Image fiber optic 2-D parallel optical interconnects based on space-CDMA

（空間ＣＤＭＡとイメージファイバとを用いた
二次元並列多重光インターコネクトの研究）

Moriya Nakamura

December 2002

Abstract

This thesis investigates image fiber optic two-dimensional (2-D) parallel optical interconnects based on space-code-division multiple access (space-CDMA). The interconnect systems considered in this thesis provide asynchronous multiple-access data links of 2-D optical signals for inter-chip to inter-cabinet interconnections and 2-D processor arrays systems. This thesis consists of seven chapters as follows.

Chapter 1 reviews the background of this thesis and provides the outline of the thesis.

Chapter 2 investigate the interference noise of 2-D orthogonal code, namely, Optical Orthogonal Signature Patterns (OOSPs) which is used in the space-CDMA scheme. Probability density function of the interference noise is theoretically derived. Multiplexing characteristics of the space-CDMA system are investigated from a aspect of bit errors caused by the interference noise.

Chapter 3 discusses the characteristics of image fibers as 2-D parallel optical data transmission media. Advantages and drawbacks of image fibers are investigated comparing 2-D parallel optical transmission media including image fibers, 2-D fiber arrays, and lens systems. Further more, image fiber skew characteristics, which is one of the most important parameters of parallel transmission media, is investigated.

Chapter 4 proposes a novel concept of the image-fiber branching and a simple construction using graded index (GRIN) rod lenses. This image fiber coupler has several features including compact and reliable assembly and ease of optical alignment. This is one of the basic passive optical devices in image fiber optic systems.

Chapter 5 discusses 2-D optical amplifier based on Er-doped image-fiber amplifier (EDIFA). In this chapter, measured gain characteristics of test EDIFAs are presented. Applications and pumping method are also discussed.

Chapter 6 shows several experimental demonstrations of image fiber optic 2-D parallel optical interconnects based on space-CDMA. The experimental demonstrations include a transmission experiment using a 100-m-long image fiber. 512-Mbps 2-D parallel transmission using 8 × 8 VCSEL/PD arrays is also demonstrated.

Chapter 7 summarizes all the conclusions obtained in this thesis.

This research was conducted at the Communications Research Laboratory.

Tokyo, Japan

December, 2002

Moriya Nakamura

Acknowledgements

The author would like to express his deepest appreciation to Professor Dr. Ken-ichi Kitayama of the Graduate School of Engineering, Osaka University for his valuable instructions, discussions, and constant encouragement. The author also wishes to express heartfelt appreciation to Professor Dr. Kenji Taniguchi, Professor Dr. Kazuyoshi Itoh, and Professor Dr. Tetsuzo Tanino of the Graduate School of Engineering, Osaka University, and Professor Dr. Fumio Kishino of the Graduate School of Information Science and Technology, Osaka University for their helpful suggestions.

The author wishes to express sincere thanks to his supervisors of Communications Research Laboratory (CRL), Dr. Takashi Iida, Dr. Tadashi Shiomi, Dr. Hajime Fukuchi, Dr. Toshikazu Itabe, and Dr. Naoki Ohtani for their guidance, continuing encouragement, and valuable discussions.

The author is also indebted to Dr. Tsutomu Hara, Mr. Yuji Kobayashi, and Mr. Yasunori Igasaki of Hamamatsu Photonics K. K., Mr. Takashi Tsumanuma, Mr. Naoki Shamoto, and Mr. Keiji Kaneda of Fujikura Ltd., and Dr. Toshimichi Otsubo of CRL for their technical assistance and useful discussions.

Appreciation is also due to Dr. Toshiaki Kagawa of NTT for providing VCSEL/PD arrays.

Finally, the author would like to express sincere gratitude to his friends of Osaka University and CRL for their continuous support.

Contents

List of figures

List of tables

Chapter 1

Introduction

Parallel optical interconnection is an important technique for high-performance computing and switching systems because its high-speed optical transmission without parallel/serial data conversion enables an increased data throughput. There have been various reports on parallel optical interconnection modules using fiber ribbons and one-dimensional (1-D) laser diode (LD)/photo diode (PD) arrays. However, for massively parallel processing systems using smart pixel technology, whose structure is a two-dimensional (2-D) processor array, the use of 2-D parallel optical interconnections is essential because the data to be transmitted are 2-D [1]. Additionally, 2-D parallel transmission can dramatically increase the channel capacity in comparison with 1-D parallel transmission.

2-D parallel optical interconnects have been studied mainly in the area of free-space optical interconnects using lens systems [2], [3]. 2-D parallel optical transmission using lens systems can take full advantage of the parallelism of optics. However, lens systems are not flexible in system implementations because the arrangement of each component is restrained by lens parameters such as focal length and, especially, it is difficult to apply them to inter-processor-board and inter-cabinet interconnections. That is why there is a need for a fiber-based 2-D parallel optical transmission medium that is bendable, and can transmit 2-D data in parallel.

Image fiber is an important candidate for fiber-based 2-D parallel optical transmission medium. An image fiber has several thousands to several tens of thousands of cores in a common cladding, and it can transmit 2-D optical signals in parallel. Image fibers have been used as a direct-image transmission medium for, e.g., medical endoscopy and industrial inspection. Some experimental demonstrations of image-fiber based optical interconnects have been reported [4-8]. In these demonstrations, however, image fibers were used only for point-to-point connection with one transmitter and one receiver, and multiple access of one-to-many connection remains to be

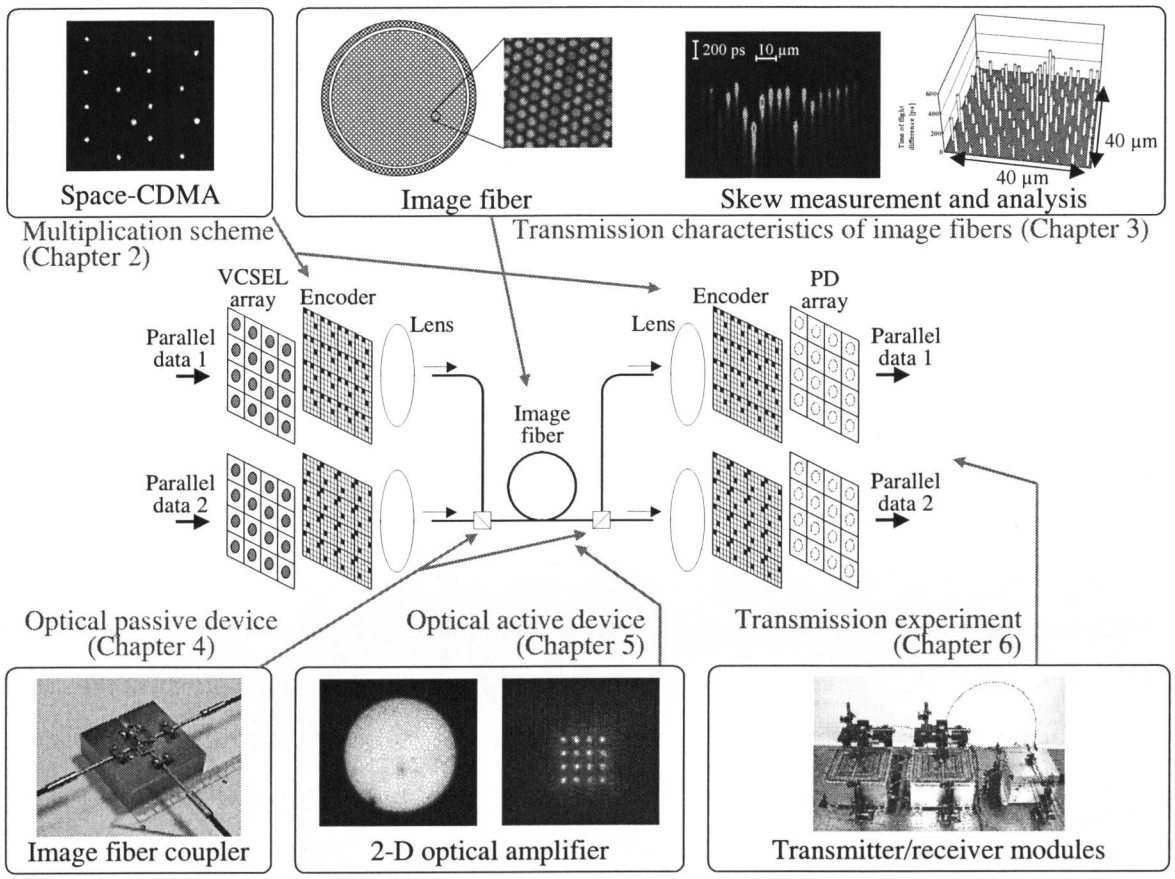

Fig. 1.1: Overview of this thesis.

developed.

One method to realize the 2-D multiple access is to use a network switch [9]. Another is to employ multiplexing schemes [10]. A novel multiplexing scheme called space-code-division multiple access (space-CDMA) has been proposed for multiplexing 2-D parallel optical signals [11], [12]. In the space-CDMA scheme, bit-signals in 2-D parallel data are encoded using 2-D spatial orthogonal code called optical orthogonal signature patterns (OOSPs), and multiplexed. The receivers can decode only an intended parallel signal by correlating the received pattern with the corresponding OOSP [11]. By using the space-CDMA scheme, a number of optical 2-D channels can be established simultaneously with individual clock speed, and asynchronous transmission is possible. This thesis investigates image fiber optic 2-D parallel optical interconnects based on space-CDMA. Figure 1.1 schematically shows the overview of this thesis.

In Chapter 2, the interference noise of 2-D orthogonal code, namely, OOSPs which is used in space-CDMA scheme is theoretically investigated [12]. Probability density function of the interference noise is derived. Multiplexing characteristics of the space-CDMA system is investigated from a aspect of bit errors caused by the interference noise. Bit-error-rate (BER)

performance is calculated in terms of the decision threshold, the code length, the code weight, and the number of users. It is shown that the BER characteristics can be improved by *prethresholding* method.

In Chapter 3, characteristics of image fibers as 2-D parallel optical data transmission media is studied [13-15]. 2-D parallel optical transmission media including image fibers, 2-D fiber arrays, and lens systems are compared, and the advantages and drawbacks are studied [14]. Image fiber skew characteristics, which is one of the most important parameters of parallel transmission media, is also investigated [13]. A novel measurement method for image fiber skew is proposed, and the characteristics is investigated experimentally and theoretically. The measurement results reveal that a test 100-m-long image fiber having 3×10^4 cores has skew of 5 ps/m, and the time-of-flight distributes randomly in the whole area of the image circle. It is shown that the skew of an image fiber is increased by bending, and the bending-induced skew does not depend on the radius of curvature and the shape of the curve but only on how many turns it is wound. The numerical calculation shows that the winding must be restricted to less than 5 turns to achieve a transmission speed over 1 Gbps/ch. Lastly we will propose a twisted image fiber and a 8-shaped bobbin for suppressing skew due to bending.

In Chapter 4, a novel concept of image-fiber branching and a simple construction using graded index (GRIN) rod lenses is proposed [16-19]. One of the key devices in the image fiber based 2-D parallel optical interconnects is the image-fiber branching device, namely, image fiber coupler. Image fiber couplers are needed to realize one-to-many and/or many-to-many data links such as space-CDMA systems. Image fibers can be branched simply by using beam-splitters (BSs) and lenses which image one end to other ends of the image fibers. However, the compact and reliable assembly and ease of optical alignment are required. The proposed image fiber coupler consists of GRIN rod lenses, a miniature cube BS, and V-grooves. This lens system has the focal points on the end surfaces of the GRIN rod lenses. Therefore, optical alignment with image fibers can be achieved simply by butt-joints on the V-grooves. Required lens parameter conditions such as numerical aperture (NA), lens diameter, and size of BS are clarified by theoretical analysis. Fabricated test image fiber coupler is experimentally characterized to clarify contrast degradation and vignetting loss characteristics.

In Chapter 5, 2-D optical amplifier based on Er-doped image-fiber amplifier (EDIFA) is proposed [20], [21]. Some 2-D parallel optical interconnect systems that interconnect several 2-D opto-electronic devices have been tested previously [22-27]. In these systems, however, branching loss is one of the most serious problems, because the 2-D optical signals are branched repeatedly to enable data links between many devices. Therefore, a 2-D optical amplifier is needed to compensate

for this loss. The 2-D optical amplifiers can be used in the same way as conventional Er-doped fiber amplifiers (EDFAs) in optical communication systems, and they also compensate for transmission loss. Additionally, 2-D optical amplifiers are applicable in image-processing and 2-D optical-data-processing systems. They will thus become key devices in future optical computing systems.

The proposed EDIFA is compared with a conventional 2-D optical amplifier based on a semiconductor optical amplifier having a vertical-cavity surface-emitting laser (VCSEL) structure. Pumping methods for the EDIFA are also proposed. Specifications of the fabricated test EDIFAs are shown. The measured gain characteristics of the test EDIFAs are presented. The measurements are compared with the characteristics of a single-core reference Er-doped fiber pulled from the same core preform. Finally, ways to achieve higher-gain EDIFAs are suggested.

In Chapter 6, several experimental demonstrations of image fiber optic 2-D parallel optical interconnects based on space-CDMA are described [24-31]. Four channels of 64-bit (8 × 8) parallel optical signals are multiplexed and transmitted through an 9-m-long image fiber using a experimental space-CDMA system in which Xe lamps and spatial light modulators (SLMs) are used to generate 2-D optical signals [24]. Experimental demonstrations of transmission through a 100-m-long image fiber [25] and decoding using prethresholding method which is theoretically investigated in Chapter 2 are also described [12]. High-speed space-CDMA system using 2-D VCSEL/PD arrays is investigated [26], [27]. In the experiment, 512-Mbps 2-D parallel transmission using 8 × 8 VCSEL/PD arrays is demonstrated. Two spatially encoded four-bit (2 × 2) parallel optical signals are emitted from the VCSEL arrays and transmitted through image fibers. After multiplexing/demultiplexing operations, the two parallel signals are individually retrieved. BER performance and tolerance of lateral misalignment are given. The transmitter/receiver structure and the optical alignment method are also described.

In Chapter 7, the overall conclusions obtained in this thesis are summarized.

Chapter 2

Space-CDMA and its theoretical performance

2.1 Introduction

Optical code-division multiple access (CDMA) allows many users, which technically collide with one another, to transmit and to be accessed simultaneously with no waiting time in an asynchronous manner. Its features include addressability by many users in the network, the ability to support bursty traffic, and natural increase in communication security. In conventional time-domain optical CDMA, each bit of input data is encoded into a waveform which corresponds to a signature sequence. All the encoded signals from transmitters are multiplexed and broadcast to all receivers. Each receiver can regenerate the intended data from the multiplexed signals by using its own signature sequence [32-35].

A novel type of CDMA, a space-CDMA, has been proposed and experimentally demonstrated for parallel transmission aiming at application to future high-throughput two-dimensional (2-D) parallel data links connecting massively parallel processors having a number of data bits regularly aligned on 2-D grids [11], or so-called bit planes [1]. In this scheme, each pixel in the bit planes is encoded into a signature pattern, namely, an optical orthogonal signature pattern (OOSP). The encoded patterns from the transmitters are multiplexed and transmitted through an image fiber.

In this chapter, the interference noise of OOSPs and the multiplexing characteristics of space-CDMA system are investigated [12]. In Section 2.2, the space-CDMA scheme and the orthogonality of OOSPs are reviewed. In Section 2.3, the noise of interfering OOSPs is analyzed and their probability density functions are derived. In Section 2.4, bit errors caused by interference noise are evaluated in terms of the decision threshold, the code length, the code weight, and the number of users. In Section 2.5, *prethresholding* method is introduced to suppress interference noise.

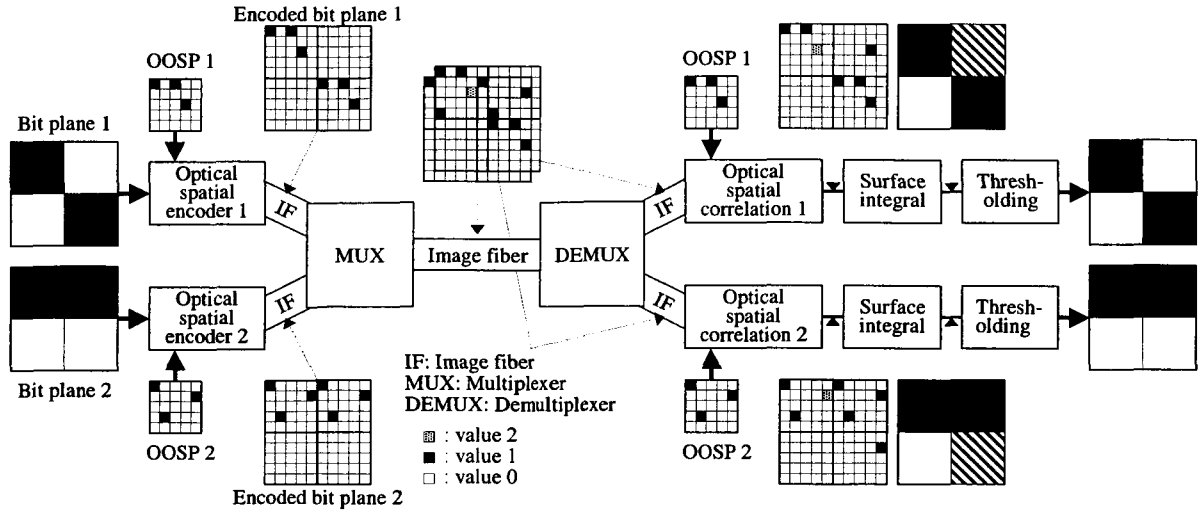

Fig. 2.1: Block diagram of the space-CDMA.

It is showen that the bit error rate characteristics of the space-CDMA system can be improved by the method. Section 2.6 is devoted to the study of the relation between the number of users and required system resolution.

2.2 Concept of space-CDMA

2.2.1 Space-CDMA scheme

2-D parallel data links based on an innovative optical space-CDMA have been proposed for future optical data links for massively parallel computer networks as well as for data transfer from optical page-oriented memories to other memories or to processors [11]. Figure 2.1 shows the schematic for the space-CDMA system. Each pixel in the input bit planes is encoded into a signature pattern, called the OOSP. The smaller pixels in OOSPs are called chip pixels. The encoded patterns from the transmitters are multiplexed and transmitted through an image fiber. The receiver correlates the received pattern with its own OOSP. The input bit plane is regenerated after thresholding is operated on the correlation output. It is noteworthy that the OOSPs are mutually orthogonal, so that it is possible to demultiplex these patterns, even if they are multiplexed with some shift.

This 2-D parallel optical link allows the transfer of 2-D bit planes without serial to parallel conversion, and hence, this resolves the "I/O bottleneck" of parallel processors caused by wiring crisis. Additionally, each receiver side can be linked to the intended bit plane by selecting the

corresponding signature pattern. Using this space-CDMA scheme, some experiments of 2-D parallel optical interconnects have been demonstrated, which will be described in Chapter 6.

2.2.2 OOSPs

The fundamental rules that govern OOSPs are: that they should retain orthogonality, and that a large number of assignable signature patterns is preferred. These rules must be achieved under two constraints that:

(1) Signature patterns must be distinguishable from any space-shifted versions of themselves in the 2-D plane and

(2) Any two different signature patterns in a set must be distinguishable from one another, even if any spatial shift exists in the 2-D plane.

Here, the possibility of rotation of encoded pattern after transmission is ruled out. These constraints require that autocorrelation peak must be much higher than the correlation side lobes, and any peaks in the cross-correlation function must be much lower than the peak for the autocorrelation function. These requirements can be expressed in binary discrete correlation forms as [11]

$$\sum_{i=1}^{M}\sum_{j=1}^{M} e_{i,j}^{(q)} e_{i+k,j+l}^{(q)} \begin{cases} = w_q & \text{for } k = l = 0 \\ \le \delta_A & \text{for } 1 \le k,l \le M-1 \end{cases}, \tag{2.1}$$

$$\sum_{i=1}^{M}\sum_{j=1}^{M} e_{i,j}^{(q)} e_{i+k,j+l}^{(q')} \le \delta_C \quad \text{for } q \ne q', 0 \le k,l \le M-1 \tag{2.2}$$

where $e_{i,j}^{(q)}$ is the matrix element of qth OOSP $\mathbf{E}^{(q)}$ which can be expressed as

$$\mathbf{E}^{(q)} = \begin{bmatrix} e_{11}^{(q)} & e_{12}^{(q)} & \bullet & \bullet & \bullet & e_{1M}^{(q)} \\ e_{21}^{(q)} & e_{22}^{(q)} & \bullet & \bullet & \bullet & e_{2M}^{(q)} \\ \bullet & \bullet & \bullet & & & \bullet \\ \bullet & \bullet & & \bullet & & \bullet \\ \bullet & \bullet & & & \bullet & \bullet \\ e_{M1}^{(q)} & e_{M2}^{(q)} & \bullet & \bullet & \bullet & e_{MM}^{(q)} \end{bmatrix}. \tag{2.3}$$

All the elements of $\mathbf{E}^{(q)}$ take binary values of 0 or 1, and each value corresponds to each chip pixel of the OOSP. Value w_q is the weight (the number of binary 1's) of OOSP $\mathbf{E}^{(q)}$. Value M is the size of

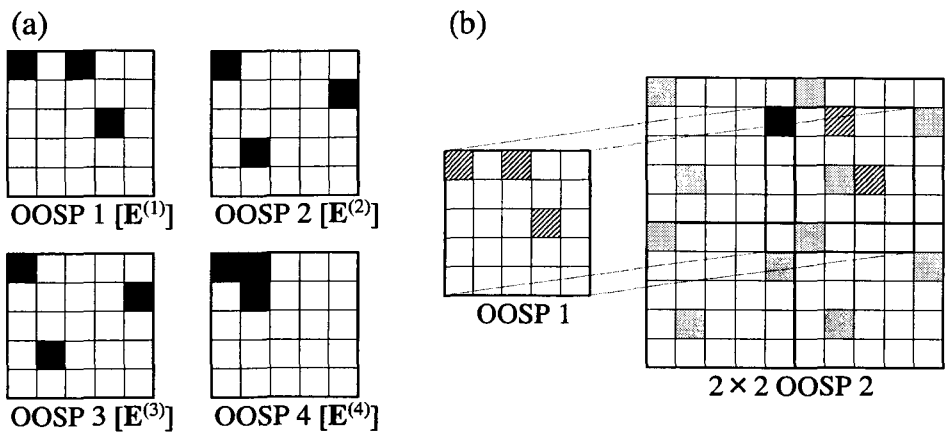

Fig. 2.2: (a) Examples of 5 × 5 OOSPs that have a weight of three. (b) Mutual orthogonality between OOSP 1 and OOSP 2.

OOSPs (or M^2 is called the spreading factor). For $k = l = 0$, Eq. (2.1) represents the autocorrelation. Constraint 1 is represented by Eq. (2.1). That is, the autocorrelation is set to w_q, and the correlation for any space shift must be equal to or less than δ_A. Constraint 2 is represented by Eq. (2.2), in that the cross-correlation for any space shift must be equal to or smaller than δ_C. In a strict sense, $\delta_A = \delta_C = 1$ is required to retain orthogonality. Furthermore, it is assumed that each weight w_q of OOSP in a set have the same value w for the sake of mathematical simplicity. In these condition, the possible maximum number of OOSPs N is bounded by [11]

$$N \leq \frac{M^2 - 1}{w(w-1)}. \tag{2.4}$$

For example, Fig. 2.2(a) shows a set of four OOSPs with $M = 5$ and $w = 3$. As shown in Fig. 2.2(b), the cross-correlation property between OOSP 1 and OOSP 2 is determined by observing the number of spatially overlapped chip pixels each time OOSP 1 is shifted vertically and horizontally, pixel by pixel over the expanded 2 × 2 plane arrangement of OOSP 2. Here, the maximum value of cross-correlation is unity. Therefore, OOSP 1 and OOSP 2 can be said to be mutually orthogonal.

2.3 Probability density function for interference noise

2.3.1 Two interfering OOSPs

As described in Section 2.2, the number of overlapping chip pixels of two different OOSPs is unity at most. The overlapping causes interference noise, resulting the degradation of signal-to-interference noise ratio (SIR). Therefore, to evaluate bit error rate (BER) in a space-CDMA system, the probability density function (PDF) of the overlapping chip pixels is investigated. The derivation of the PDF which will be described below is an extension of the one used for one-dimensional (1-D) signature sequences, or so-called optical orthogonal codes (OOCs) [36], [37].

Assume that a desired signal is encoded by OOSP 1, and OOSP 2 is an undesired signal (see Fig. 2.2(b)). As OOSP 1 is shifted on the expanded plane of OOSP 2 vertically and horizontally with a multiple of l_c, the maximum number of overlapping chip pixels would be one because of the orthogonality of OOSPs as described above, where l_c is the side length of a square chip pixel. The area of overlap corresponds to the interfering noise. The probability of the one overlap is w^2/M^2, because, for each chip pixel of value 1 in OOSP 2, there are w possible chip pixels of OOSP 1 where the overlaps can take place, and there are M^2 relative positions for OOSP 1. It is assumed that the relative position of OOSP 1 is uniformly distributed. Furthermore, if each pixel for the bit planes is modulated by on-off keying with a duty ratio of 1/2 (i.e., if the duty ratio of the bit stream from each pixel of the bit planes is 1/2), then the probability for overlap would be $w^2/2M^2$. For example, OOSPs in Fig. 2.2(b) have three chip pixels of value 1 and there are 9 ($w^2 = 3^2$) possible relative positions where the one overlap take place. The total relative position between OOSP 1 and OOSP 2 is 25 ($M^2 = 5^2$). Consequently, in this case, the probability of the one overlap is $9/(2 \times 25)$. The complement of this event, which corresponds to the probability for non overlap, is $1 - w^2/2M^2$. Therefore, the PDF $P_u(u)$ for u overlapping chip pixels can be defined as

$$P_u(u) = \left(1 - \frac{w^2}{2M^2}\right)\delta(u) + \frac{w^2}{2M^2}\delta(u-1), \tag{2.5}$$

where δ is Diarc delta function. The mean and variance for the random variable u are $m_u = w^2/2M^2$ and $\sigma_u^2 = (w^2/2M^2)(1-w^2/2M^2)$, respectively.

The shifts of OOSPs were restricted to a multiple of l_c. To derive the PDF in a rigorous manner, overlap when the shifts are not integer multiples of l_c have to be investigated. However, in this case the PDFs $P_{ij}(u)$ for all combination of interfering ith and jth OOSPs do not have the same function [36]. For a set of N OOSPs, ${}_N\mathrm{C}_2 = N(N-1)/2$ different PDFs have to be derived. However, concerning the mean m_{ij} and variance σ_{ij}^2 of $P_{ij}(u)$, it can be said that

$$m_u = m_{ij}, \tag{2.6}$$

$$\sigma_{ij}^2 < \sigma_u^2. \tag{2.7}$$

Furthermore, σ_u^2 can be used as an approximation to the actual value σ_{ij}^2 [36]. In general, the variance of interference or noise signal is directly proportional to its own power, i.e., it can be said that the larger the variance, the higher the bit error rate. For mathematical convenience, the PDF $P_u(u)$ as an approximation to derive the upper bound on bit error rate can be used. Therefore, in the discussion below, it is assumed that the shifts of OOSPs are restricted to a multiple of l_c.

2.3.2 *N* interfering signals

In a general space-CDMA system there would be N users. Therefore interference with N interfering OOSPs has to be investigated to evaluate system performance. (In this discussion the effect of quantum noise and thermal noise is neglected. It is assumed that error is only due to the interference noise of OOSPs. Furthermore, all transmitters have the same power at all receiver sides.)

For notational simplicity it is assumed that the desired signal is denoted by $n = 1$ in N interfering signals. The intensity of the total interference noise on the desired signal is sum of interference noise from the other n - 1 interfering signals, i.e.,

$$I_1 = \sum_{n=2}^{N} I_n^{(1)} \tag{2.8}$$

where I_1 is the intensity of the total interference to the desired signal $n = 1$, and $I_n^{(1)}$ is the intensity of the interference noise to the desired signal $n = 1$ from other nth ($n \neq 1$) signal. Each $I_n^{(1)}$ takes a value of 0 or 1 on the PDF shown in Eq. (2.5), and $I_n^{(1)}$ are independent. Hence the PDF for the random variable I_1 can be represented by binomial distribution as

$$P_{I_1}(I_1) = \sum_{i=0}^{N-1} {}_{N-1}\mathrm{C}_i \left(\frac{w^2}{2M^2}\right)^i \left(1 - \frac{w^2}{2M^2}\right)^{N-1-i} \delta(I_1 - i). \tag{2.9}$$

From (9), I_1 can take values $0 \le I_1 \le N-1$, and the mean m_{I_1} and variance $\sigma_{I_1}^2$ for I_1 can be

expressed as

$$m_{I_1} = (N-1)\frac{w^2}{2M^2} \tag{2.10}$$

$$\sigma_{I_1}^2 = (N-1)\frac{w^2}{2M^2}\left(1-\frac{w^2}{2M^2}\right). \tag{2.11}$$

2.4 BER performance of space-CDMA

2.4.1 Theoretical upper bound on BER

In general, an error occurs in a CDMA system when the transmitted datum is 0 and the interference noise is over the thresholding level Th, i.e., $I_1 \geq Th$. Therefore the probability of error, BER, can be expressed as

$$\text{BER} = \frac{1}{2}\int_{Th}^{\infty} P(I_1)dI_1, \tag{2.12}$$

where $P(I_1)$ is the exact PDF of the interference noise I_1. As described in Section 2.3, $P(I_1)$ is hard to derive, and the approximation (upper bound) $P_{I_1}(I_1)$ was calculated. Therefore we can express the upper bound on BER using the approximation

$$\text{BER} < \frac{1}{2}\int_{\text{Th}}^{\infty} P_{I_1}(I_1)dI_1 \tag{2.13}$$

and, from Eq. (2.9),

$$\text{BER} < \frac{1}{2}\sum_{i=\text{Th}}^{N-1} {}_{N-1}\text{C}_i\left(\frac{w^2}{2M^2}\right)^i\left(1-\frac{w^2}{2M^2}\right)^{N-1-i}. \tag{2.14}$$

2.4.2 BER performance of space-CDMA

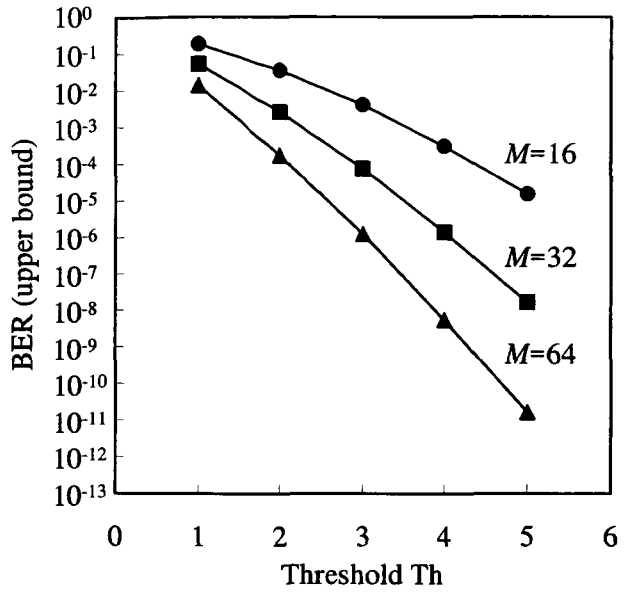

Fig. 2.3: Upper bound on the BER versus the threshold for N = 10, w = 5, and M = 16, 32, 64.

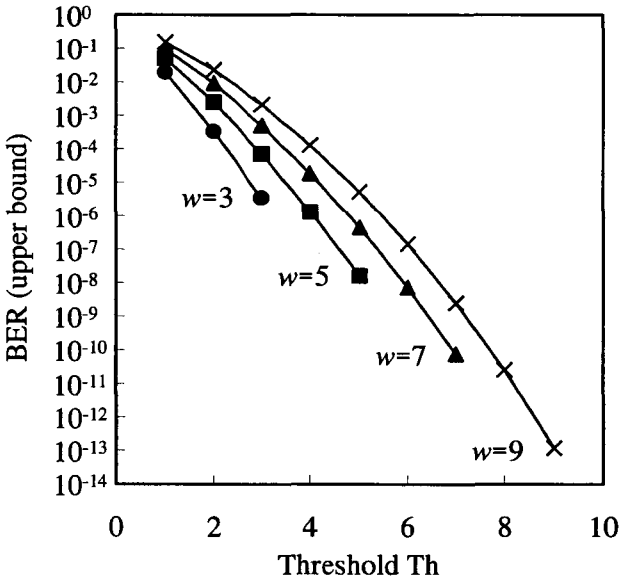

Fig. 2.4: Upper bound on the BER versus the threshold for N = 10, M = 32, and w = 3, 5, 7, 9.

Figure 2.3 shows the upper bound of the BER versus the threshold for a fixed number of users (N = 10) and weight (w = 5) and different matrix sizes of OOSPs (M = 16, 32, 64). When the threshold increases, the smaller the probability becomes that interference noise will exceed the threshold, resulting in the improvement of the BER. When the size of OOSPs increases, the system performance is improved for a constant weight. This is because as the size of the OOSPs becomes larger, a decrease in the probability of overlapping of chip pixels is expected. However, it should be noted that larger OOSP requires a higher spatial resolution on transmission characteristics in the space-CDMA system. Figure 2.4 shows the upper bound of BER versus the threshold for the

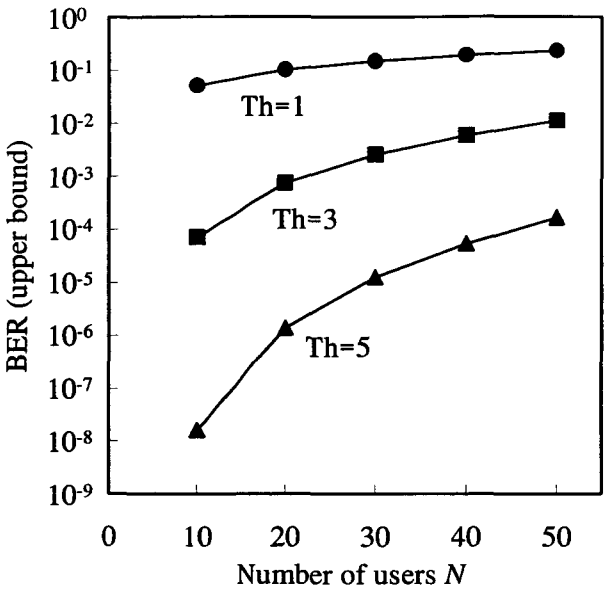

Fig. 2.5: Upper bound on the BER versus the number of users for M=32, w=5, and Th = 1, 3, 5.

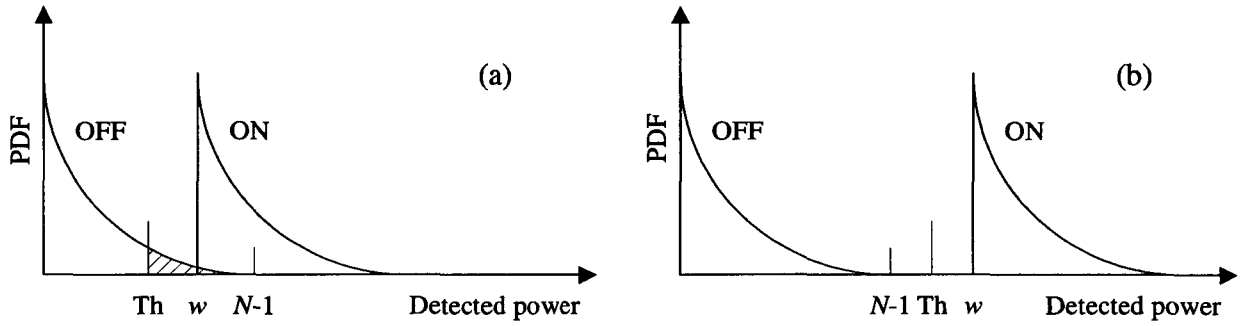

Fig. 2.6: (a) PDF of the detected power. (b) PDF of the detected power in the special case of N - 1 < w.

number of users N = 10 and the sizes of OOSPs M = 32 for a variety of weight w = 3, 5, 7, 9. When the weight increases, the value of BER also increases for the same threshold value because of the increase in the probability that the chip pixels of OOSPs overlap each other. However, with a large weight value the system performance can be improved if the threshold is increased. Figure 2.5 shows the BER (upper bound) versus the number of users for the size of OOSPs M = 32 and a weight w = 5 with a variety of the threshold levels Th = 1, 3, 5.

In general, the larger the threshold value, the better the system performance becomes. However, Th is limited by the weight w because the power w of desired signal have to be detected as ON. Here, the optical power per one chip pixel is defined as unity. This can be explained by Fig. 2.6(a), in which the PDF of the detected power is schematically shown. The power which corresponds to OFF or ON has some width caused by the interference noise expressed by Eq. (2.9). From Eq. (2.8),

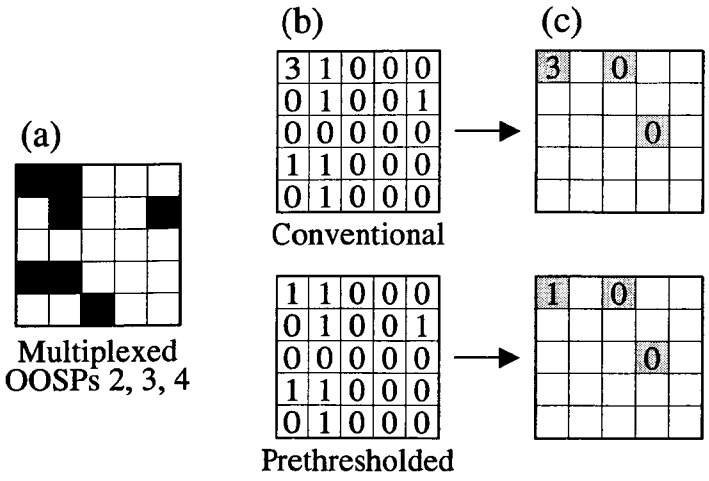

Fig. 2.7: (a) Multiplexed image of three OOSPs (2, 3, and 4). (b) Intensity distribution of the multiplexed image. (c) Distribution correlated with OOSP 1.

the maximum of interference noise is N - 1. The probability of error corresponds to the shaded area. It is noteworthy that if $w > N - 1$, the error caused by the interference can be zero when the threshold is set as $N - 1 < Th \leq w$ [Fig. 2.6(b)].

As described above, in this study it is assumed that error is due only to the interference noise of the OOSPs, neglecting the effect of quantum noise and thermal noise. However, from some experimental study [22], [24], it can be said that the interference noise of OOSPs is dominant. Therefore these results for the BERs are significant when estimating the performance of space-CDMA systems and in designing OOSPs.

2.5 Prethresholding method

2.5.1 BER inprovement using prethresholding method

In this section prethresholding method is introduced to improve the BER performance of the space-CDMA systems. Similar thresholding has been applied in conventional CDMA systems and other data-recovery systems by use of the correlation process [36], [37]. The BER that is due to interference noise can be reduced by the introduction of prethresholding before the correlation process shown in Fig. 2.1. For example, the three OOSPs, 2, 3, and 4 in Fig. 2.2(a) are multiplexed as shown in Fig. 2.7(a). The top of Fig. 2.7(b) shows the four-levels of intensity created by conventional multiplexing, and the bottom shows the intensity distribution obtained by the

prethresholding of each chip pixel. The distribution correlated with OOSP 1 is shown in Fig. 2.7(c). Without prethresholding (shown at the top), an error occurs even if the threshold level is set at three; on the other hand, prethresholding (shown at the bottom) allows decoding without an error when the threshold is between unity and three. This satisfies the constraint for a thresholding level Th of $1 \le Th \le w$.

It is mathematically complicated to derive an explicit expression of the BER for the case in which the shifts of OOSPs are multiples of l_c, the side length of a square chip pixel. However, we can derive the upper bound for the interference signal I_1. The PDF for I_1 can be written as (see Appendix A)

$$P_{I_1}(I_1) \le \sum_{i=1}^{N-1} \left\{ {}_wC_i \prod_{m=1}^{i} \left(1 - q_c^{N-m}\right) \right\} \delta(I_1 - i) \tag{2.15}$$

where the symbol Π denotes the product.

From inequality (2.13) and expression (2.15), the BER when the prethresholding method is used can be expressed as

$$\text{BER} < \frac{1}{2} \sum_{i=Th}^{w} \left\{ {}_wC_i \prod_{m=1}^{i} \left(1 - q_c^{N-m}\right) \right\}. \tag{2.16}$$

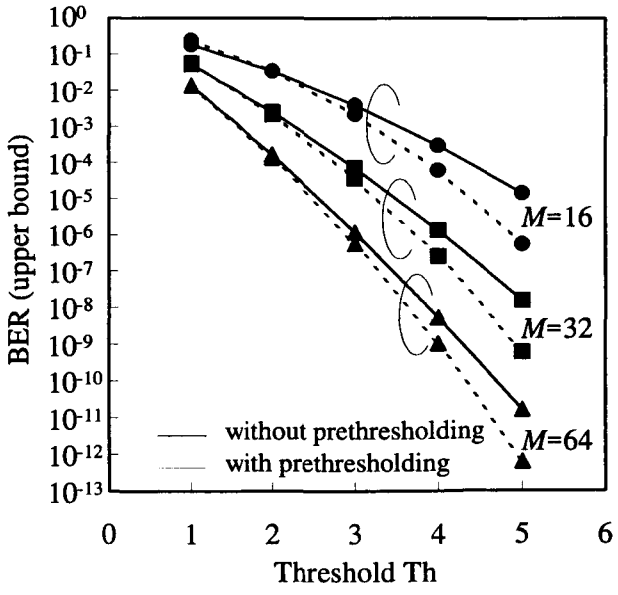

Fig. 2.8: Upper bound on the BER versus the threshold with and without prethresholding for N = 10, w = 5, and M = 16, 32, 64.

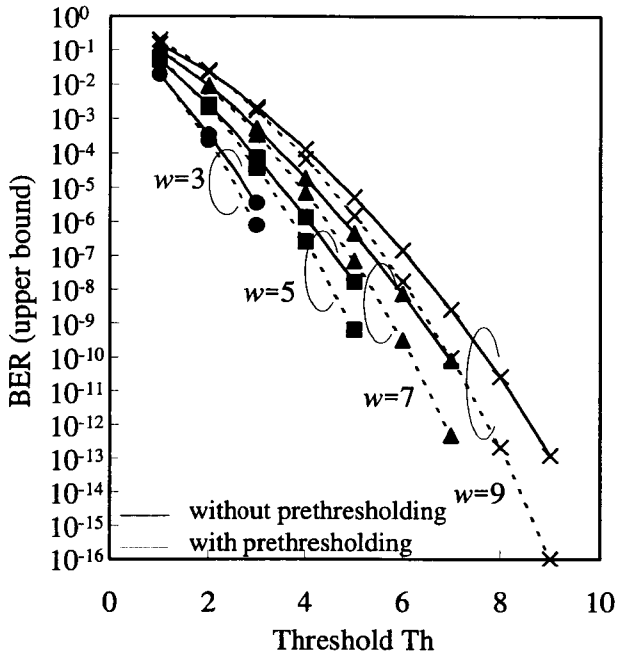

Fig. 2.9: Upper bound on the BER versus the threshold with and without prethresholding for N = 10, M = 32, and w = 3, 5, 7, 9.

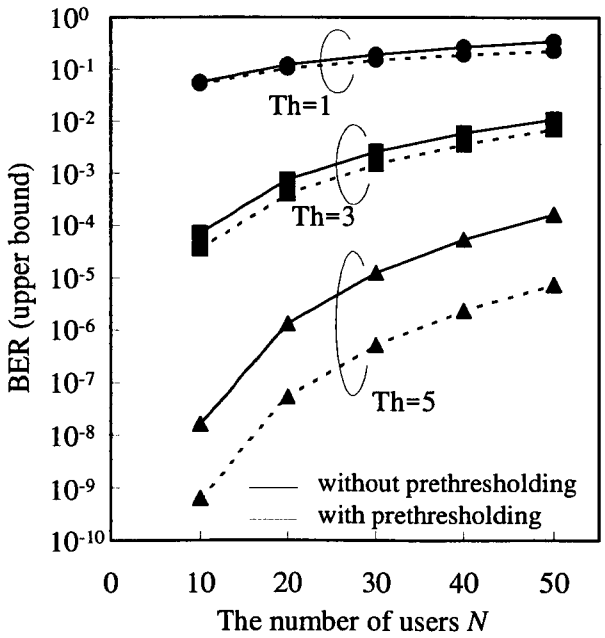

Fig. 2.10: Upper bound on the BER versus the threshold with and without prethresholding for M = 32, w = 5, and Th = 1, 3, 5.

2.5.2 BER performance of space-CDMA with prethresholding method

Figures 2.8 and 2.9 show BERs as functions of the thresholding level Th with and without prethresholding for different values of M and w. In Fig. 2.10, the BER is plotted as a function of the number of users N for various values of Th. These figures show that prethresholding improves the system performance. Prethresholding is particularly effective in the region where the threshold value is large. This can be understood by examining the two extreme case. When Th is set at 1, prethresholding cannot improve the BER because it suppresses the intensity of interfering noise at each position of a chip pixel to only one, which exceeds the threshold value. On the other hand, when Th is set at the maximum value w in the system with prethresholding, the interference from other OOSPs has to hit at all the chip-pixel positions to exceed Th, which is apparently rare case. In general, Th is set as large as possible to derive superior system performance. Therefore, from Figs. 2.8–2.10, it can be said that the prethresholding works effectively to improve the space-CDMA system performance. The efficiency of the method has also been experimentally verified, which will be described in Section 6.2.

2.6 Conclusion

As described above, to improve BER, it is necessary to increase the size of OOSPs M and, at the same time, to select the maximum value of code weight w. However, M ,w and the number of users N have to satisfy the Eq. (2.4). On the other hand, the larger M becomes, the better the spatial resolution that is required. In addition, the resolution is limited by the devices used in the implementation. From Eq. (2.4) the maximum value of w is limited by

$$w \le \left\lfloor \frac{1}{2} + \sqrt{\frac{4M^2 + N - 4}{4N}} \right\rfloor, \tag{2.17}$$

where $\lfloor x \rfloor$ denotes the integer portion of the real value x. As explained above, BER can be determined by the four parameters M, w, N, and Th. In general, BER can be reduced by increasing the threshold level Th; therefore we set Th for its maximum value, Th = w, in this discussion. In this case BER can be expressed as

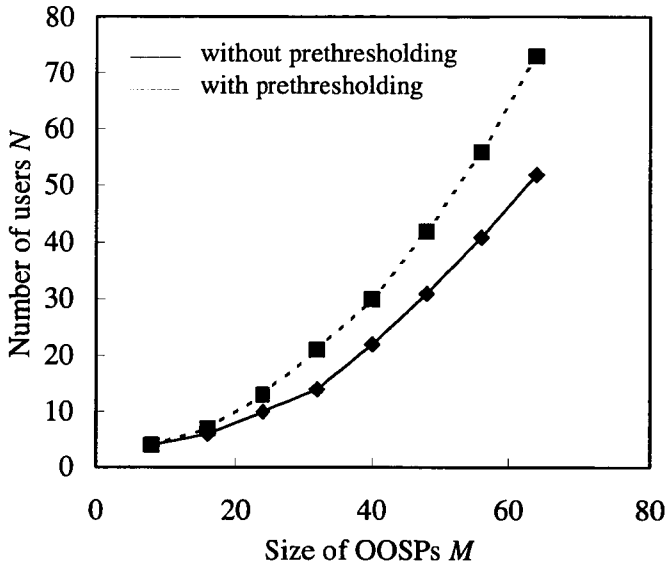

Fig. 2.11: Maximum number of users with the restriction of BER < 10^{-9}.

$$\mathrm{BER} < \frac{1}{2}\sum_{i=w}^{N-1} {}_{N-1}\mathrm{C}_i \left(\frac{w^2}{2M^2}\right)\left(1-\frac{w^2}{2M^2}\right)^{N-1-i}, \quad \text{(without prethresholding)}, \tag{2.18}$$

$$\mathrm{BER} < \frac{1}{2}\prod_{m=1}^{w}\left\{1-\left(1-\frac{w}{2M^2}\right)^{N-m}\right\}, \quad \text{(with prethresholding)}. \tag{2.19}$$

Additionally, the value of w is determined by the equation (2.17). Hence BER can be calculated by only two parameters M and N. Figure 2.11 shows the maximum number of users N versus M with the restriction that BER < 10^{-9}. When N increases, very large size of OOSPs is required, even if prethresholding method is used. Commercial type high contrast image fiber has the resolution of about 50 lp/mm (lp: line pairs). For example, if a thick image fiber with the diameter 3 mm is used, a pattern of about 210 × 210 square matrix can be transmitted in parallel. In a case that the matrix of signal is 8 × 8, the size of OOSPs has to be smaller than 26 (<210/8). In this case, from the Fig. 2.11, the maximum number of users are limited up to 16 to satisfy BER < 10^{-9}. To multiplex larger number of users, the OOSPs with larger size have to be used and it is needed to increase the system resolution. Therefore, it is crucial to develop high-resolution (and high-contrast) image fibers. And it is also important to design OOSPs with low mutual interference which does not require such a high resolution to satisfy a sufficiently low BER [38].

For conclusion, in this Chapter, the multiplexing characteristics of the space-CDMA system was

investigated. The upper bound on BER was calculated for a variety of different parameters to clarify the system performance. Furthermore, the prethresholding method to improve the performance was introduced, and its efficiency was proved by BER analysis. Efficiency was also demonstrated experimentally.

Chapter 3

Image fiber for 2-D parallel optical data link

3.1 Introduction

"2-D parallel" is one of the most intriguing keywords in the area of optical interconnects. Optical interconnects are categorized into fiber based optical interconnects and free-space optical interconnects. 2-D parallel optical interconnects have been studied mainly in the area of free-space optical interconnects using lens systems [2], [3]. 2-D parallel optical transmission using lens systems can take full advantage of the parallelism of optics. However, lens systems are not flexible in system implementations because the arrangement of each component is restrained by lens parameters such as focal length and, especially, it is difficult to apply them to inter-processor-board and inter-cabinet interconnections. That is why there is a need for a fiber-based 2-D parallel optical transmission medium that is bendable, and can transmit 2-D data in parallel.

Image fiber is an important candidate for fiber-based 2-D parallel optical transmission medium. Figure 3.1 shows a cross-sectional view of an image fiber. An image fiber has several thousands to

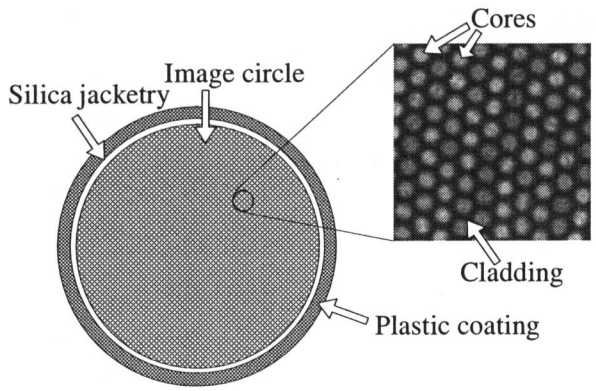

Fig. 3.1: Cross-sectional view of an image fiber.

several tens of thousands of cores in a common cladding, and it can transmit 2-D optical signals in parallel. Image fibers have been used as a direct-image transmission medium for, e.g., medical endoscopy and industrial inspection. Therefore, transmission characteristics of image fibers as optical data transmission media have not been well studied.

In this chapter, characteristics of image fibers as parallel optical data transmission media is studied [13], [14]. Section 3.2 compares 2-D parallel optical transmission media including image fibers, 2-D fiber arrays, and lens systems and studies the advantages of the image fibers [14]. In Section 3.3, image fiber skew characteristics, which is one of the most important parameters of parallel transmission media, is studied [13]. A novel measurement method for image fiber skew is proposed, and the characteristics is investigated experimentally and theoretically. The measurement results reveal that a test 100-m-long image fiber having 3×10^4 cores has skew of 5 ps/m, and the time-of-flight distributes randomly in the whole area of the image circle. It is shown that the skew of an image fiber is increased by bending, and the bending-induced skew does not depend on the radius of curvature and the shape of the curve but only on how many turns it is wound. The numerical calculation shows that the winding must be restricted to less than 5 turns to achieve a transmission speed over 1 Gbps/ch. Lastly we will propose a twisted image fiber and a 8-shaped bobbin for suppressing skew due to bending.

Table 3.1: Comparison of 2-D parallel optical transmission media

Media		Advantages	Drawbacks
Fiber based	Image fiber	No need of precise optical alignment at input or output end Independence of array size and geometric configurations of optical signals Capability of simple branching Low skew	Low coupling efficiency with LD array Transmission distance restricted by crosstalk between core High cost
	2-D fiber array	Good coupling efficiency with LD arrays Low crosstalk	Deviation of core spacing Small array size Difficult to fabricate simple branching devices Difficult to control skew Bulky
Free-Space	Lens system	Massive parallelism Compact assembly	Precise assembly is required Difficult to apply to inter-board and inter-cabinet interconnects Bulky

3.2 Image fiber vs. other 2-D parallel optical transmission media

3.2.1 2-D parallel optical transmission media

Table 3.1 is a summary of the advantages and disadvantages of various 2-D parallel optical transmission methods for optical interconnects. Since free-space optical interconnects can take full advantage of the parallelism possible with optics, massively parallel transmission can be achieved by using lens systems, including spherical lenses, micro-lens arrays, and/or graded index (GRIN) rod lenses to construct imaging systems and beam systems [2] ,[3]. However, assembly requires a high precision, and the arrangement of each component is restricted by lens parameters such as focal length. Therefore, free-space optical interconnects are not suitable for making inter-board and inter-cabinet connections, which require the interconnects with handling-ease as well as a flexibility in the configuration. For making inter-board and inter-cabinet connections, and for intra-board interconnections, therefore, fiber-based optical interconnects might be suitable. To our knowledge, only two fiber based 2-D parallel transmission methods are available at present: image fibers and 2-D fiber arrays. The 2-D fiber array is a bundle of optical fibers, the ends of which are aligned to form a 2-D array [39-42]. The 2-D fiber array can achieve a low degree of crosstalk and efficient coupling. However, it is difficult to control its core pitch precisely when the array size becomes relatively larger. Skew is also a problem because the 2-D fiber is a bundle of discrete optical fibers like a fiber ribbon.

3.2.2 Advantages of image fibers

An image fiber provides a solution to the problems of lens systems and 2-D fiber arrays. An image fiber is a multi-core fiber that has several thousands to several tens of thousands of cores in a common cladding. The typical dimensions are 3 μm in core diameter, 5 μm in spacing between cores, 800 μm in image diameter, etc. Such fiber is widely and typically used as a short-range, direct-image transmission medium for, e.g., medical endoscopy and industrial inspection. An image fiber can also be applied to the transmission of 2-D parallel optical signals. Figure 3.2 is a schematic view of a system for 2-D parallel optical transmission between 2-D VCSEL/PD arrays via an image fiber. An optical signal is incident on a small area within the image circle and is transmitted by some cores because the spacing between cores is only a few micrometers. Optical signals can be transmitted via any point on the image circle so that precise optical alignment is

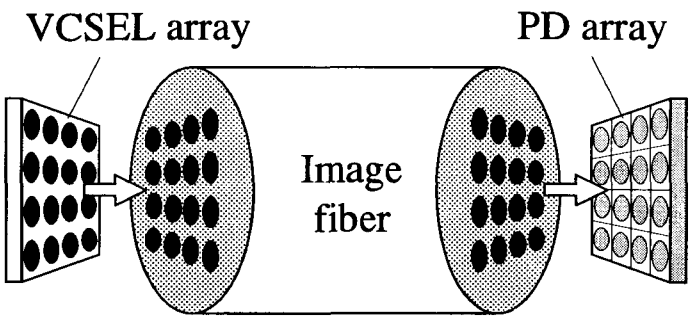

Fig. 3.2: Image fiber optic 2-D parallel interconnection between 2-D VCSEL/PD arrays.

needed neither at the input nor the output end, when the fiber is coupled with 2-D VCSEL/PD arrays. The image fiber that can be used is independent of both the array size and geometric configuration of the optical signals. Simple branching devices can be fabricated by using imaging lenses, which is described in Chapter 4. Furthermore, a low degree of skew can be expected. However, a large coupling loss of over 5 dB that arises because light incident on the cladding area is not transmitted is a drawback [43]. This coupling loss depends on the ratio of the cross-sectional areas of the cores and the cladding. In addition, crosstalk between cores restricts the transmission distance because the longer the image fiber, the greater the crosstalk. In spite of these drawbacks, the image fiber may find suitable applications to inter-board and inter-cabinet interconnections, especially in systems that include 2-D processor arrays, because of the many advantages over the other currently available 2-D parallel optical transmission methods.

3.3 Skew characteristics of image fiber

3.3.1 Skew of image fibers

One of the most important parameters of parallel optical transmission media is skew. Skew is defined as the maximum difference of propagation time between transmission channels, and it limits synchronous parallel transmission speed. In inter-cabinet interconnections, which need a transmission distance of up to 100 m, skew has to be less than 1 ps/m for a transmission speed of 1 Gbps/ch [nonreturn to zero (NRZ) pulsewidth: 1 ns]. Some theoretical analyses of skew of fiber ribbons and attempts to fabricate low-skew fiber ribbons have been reported [44], [45]. However, skew of image fibers has not been well studied. One reason is that the conventional phase method [45], which is used to measure skew, can not be suitably applied because an image fiber has so many cores and the core spacing is only a few microns.

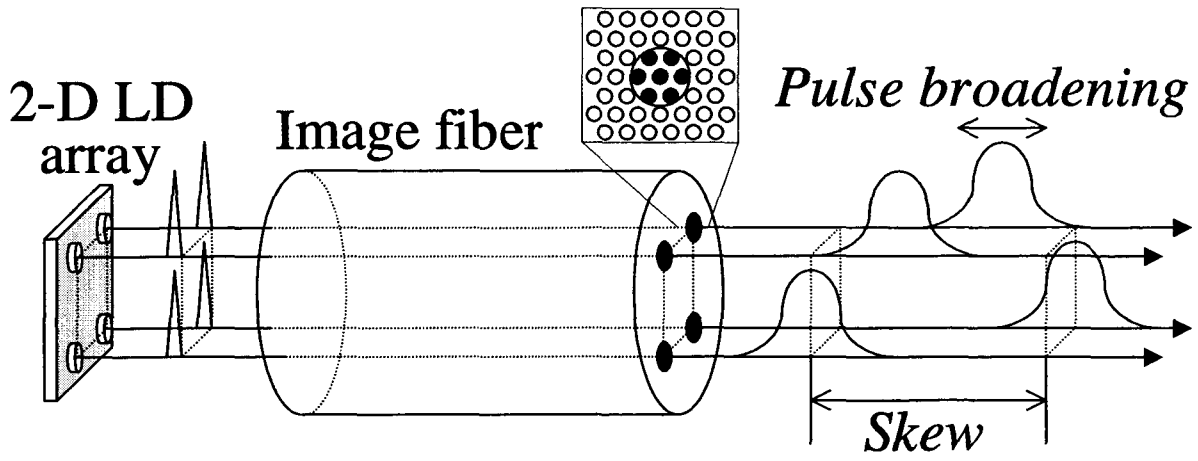

Fig. 3.3:Pulse broadening and skew caused by propagation delay difference between image-fiber cores.

Figure 3.3 schematically shows the propagation delay difference on optical pulses propagated through an image fiber. Each optical pulse having a finite spot-size broadens during the propagation in several cores. Because each core has a different propagation delay caused by fluctuations of relative refractive index and core diameter. Additionally, optical pulses arrive at the output end at different times because of uneven distribution of propagation delay over the whole image circle. This uneven distribution is caused by the residual stress as well as bending. To apply the image fiber to high-speed 2-D optical data link, we need to characterize both the local time-of-flight difference between individual cores in a small area and the global distribution of time-of-flight difference in the whole area of an image circle.

3.3.2 Novel skew measurement method

The time-of-flight difference of fiber ribbons has been measured by using the phase method. The phase method compares the phase of each transmitted signal with that of a reference channel. However, this method is difficult to apply to image fibers because an image fiber has several tens of thousands of cores and the spacing between cores is only a few microns.

To the authors' knowledge, only one attempt to evaluate skew of image fibers has been reported by Kawai et al. [43]. The skew was evaluated from the broadened optical pulse width after the propagation through an image fiber by taking into account the mode dispersion. However, this method has some problems such as: i) inability to measure time-of-flight difference between individual cores, and ii) practical difficulty to measure distribution of time-of-flight difference in whole area of an image circle.

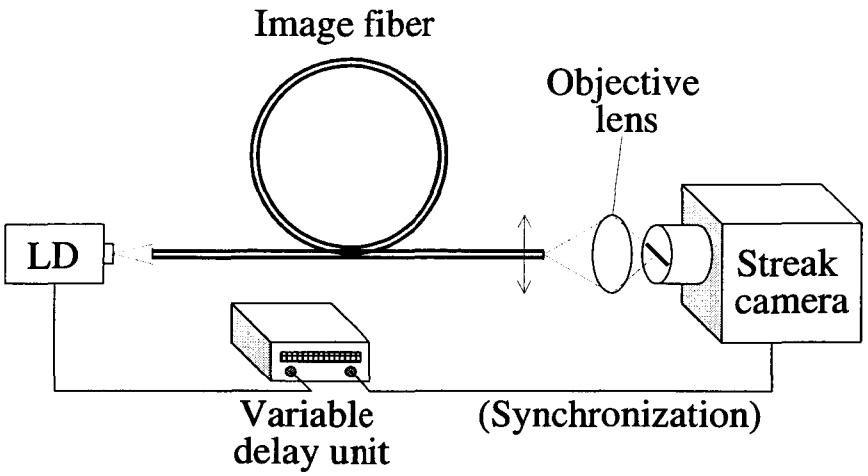

Fig. 3.4: Proposed skew measurement system.

Figure 3.4 schematically shows the proposed measurement method. An optical pulse is launched into all the cores of an image fiber. The output light of the image fiber is imaged on the front-end horizontal slit of the streak camera by an objective lens. The optical pulses which pass through the slit induce electrons on a photoelectric surface, and all the electrons are simultaneously swept vertically in the streak camera. The time-of-flight difference between the cores results in deviations along a vertical line. Thus, all the optical pulses propagated through the cores imaged on a line along the slit are observed simultaneously on a real-time basis. The output endface of the fiber is scanned by moving in the vertical direction in order to measure the image circle area. This measurement method will resolve the problems i) and ii) described above. The precision of the measurement method is restricted only by the time resolution of the streak camera. The streak camera (Hamamatsu Photonics K. K., Model C5680) used in our experiment has a time resolution of 2 ps. The pulse jitter of the LD has the same influence on all the optical pulses propagated through the cores and, consequently, no influence on the relative propagation delay between the optical pulses. The jitter therefore does not effectively degrade the precision of the measurement.

3.3.3 Experimental results

By using the proposed method, we have measured the skew of an image fiber. The measured image fiber is 100-m-long. It has 3×10^4 cores, and the picture diameter is 800 μm. The core diameter and the spacing are 3.0 and 4.4 μm, respectively. The materials of cores and cladding are silica glass. In the measurement, the image fiber was extended almost straight. Optical pulses of the LD was 59 ps in full width at half maximum (FWHM) at the wavelength of 650 nm. The cores are of multi-mode at this wavelength.

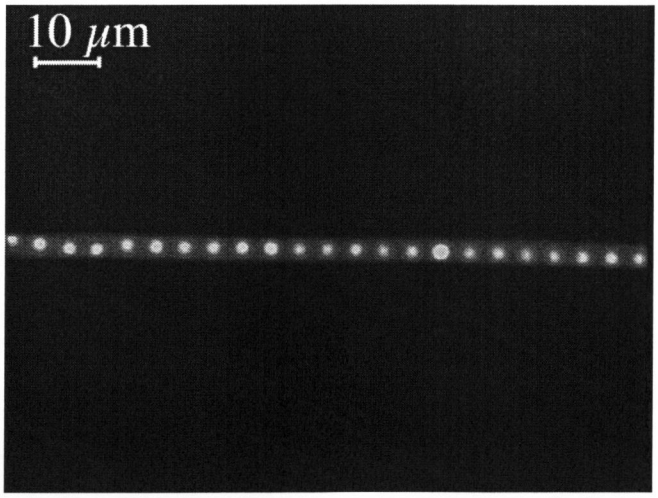

Fig. 3.5: Light spots imaged in a slit of a streak camera.

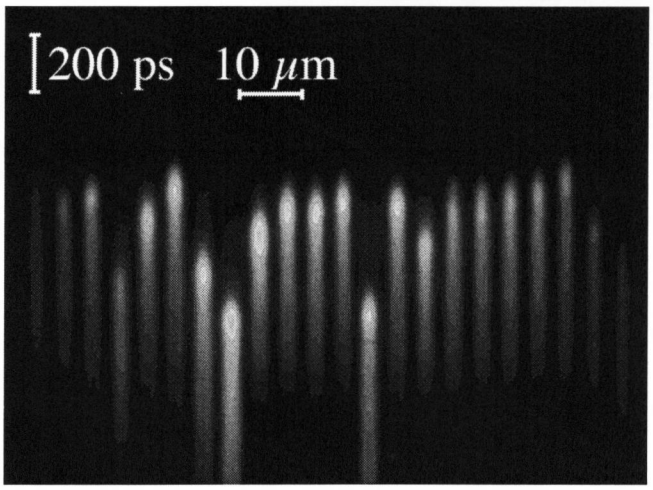

Fig. 3.6: Streak camera trace of optical pulses propagated through image fiber cores.

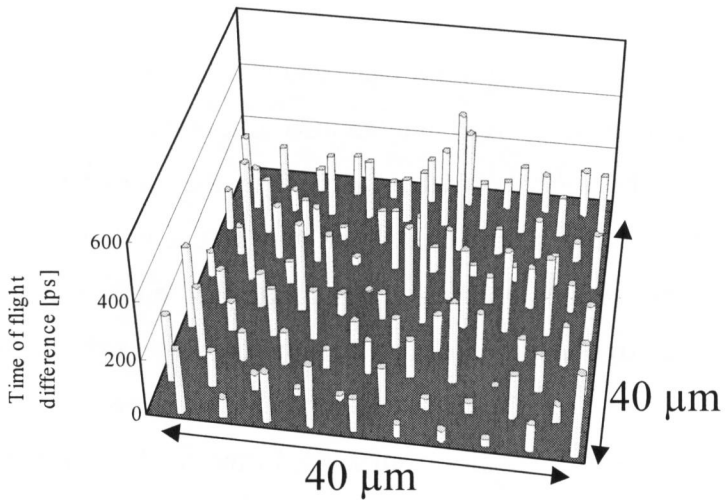

Fig. 3.7: Time-of-flight difference around the center of the test image fiber.

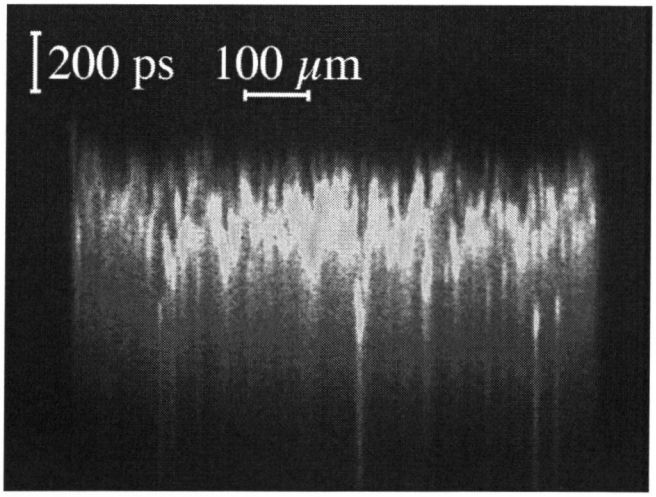

Fig. 3.8: Streak camera trace of optical pulses propagated through the cores traversing the diameter of the image circle.

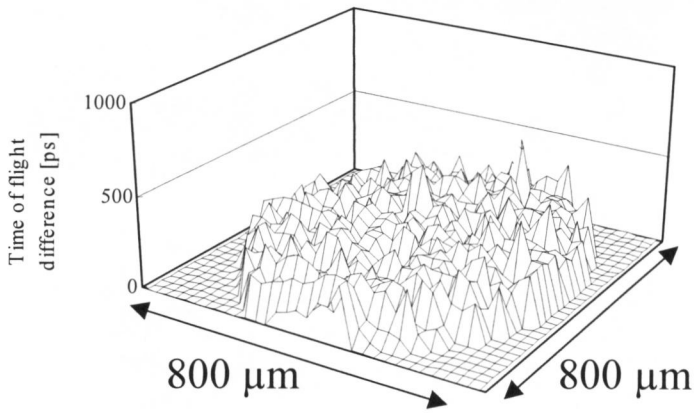

Fig. 3.9: Time-of-flight difference over the image circle (Image fiber was straight).

Figure 3.5 shows the cores focused on a front-end slit, which was observed by a streak camera without sweep. Figure 3.6 shows a streak camera trace of optical pulses propagated through twenty cores of the image fiber. The trace shows that there exists the time-of-flight difference between the observed cores. Each pulse has a trailing tail, which may be due to both the mode dispersion and the chromatic dispersion. The cores in the image fiber are aligned on the hexagonal close-packed (hcp) grids; therefore, the next row of the cores can be measured by vertically moving the image fiber observing the streak camera trace. The measured data can be plotted in a 2-D map of time-of-flight difference. Figure 3.7 shows the 2-D plot of measured time-of-flight difference at the center of the image circle. The data show the values relative to the minimum propagation delay in the area of interest. The skew ranges within 5 ps/m in the small area of 40 × 40 μm (about 100 cores). There

was no significant difference depending on the position over the whole image circle.

By changing the magnification ratio of the objective lens, a larger number of cores can be measured. Figure 3.8 shows a streak camera trace of optical pulses propagated through the cores traversing the diameter of the image circle. By scanning the output endface, a 2-D map of time-of-flight difference all over the image circle can be plotted as shown in Fig. 3.9. The global distribution of measured time-of-flight difference also rages within 5 ps/m.

From Figs. 3.7 and 3.9 the time-of-flight is distributed at random, and the skew ranges within 5 ps/m in whole area of the image circle. With the skew of 5 ps/m, the bit rate-distance product is limited to 20 Mbps·km. One reason for this relatively large skew compared to fiber ribbon's [44] is presumably due to nonuniformity of the core parameters. The test image fiber was fabricated by using some different mother-rods with different parameters. It is noted that this type of image fiber consisting of different cores is fabricated for conventional applications such as endoscope. The skew can be reduced by making the parameters of all the cores uniform.

3.3.4 Discussions on the skew due to bending

To investigate the effect of bending on the skew, the same test 100-m-long image fiber was wound by 100 turns around a 31-cm diameter bobbin, and skew was measured. Figure 3.10 shows the measurement result. By comparing it with Fig. 3.9, the skew is increased monotonically toward the outer diameter by bending up to about 2 ns.

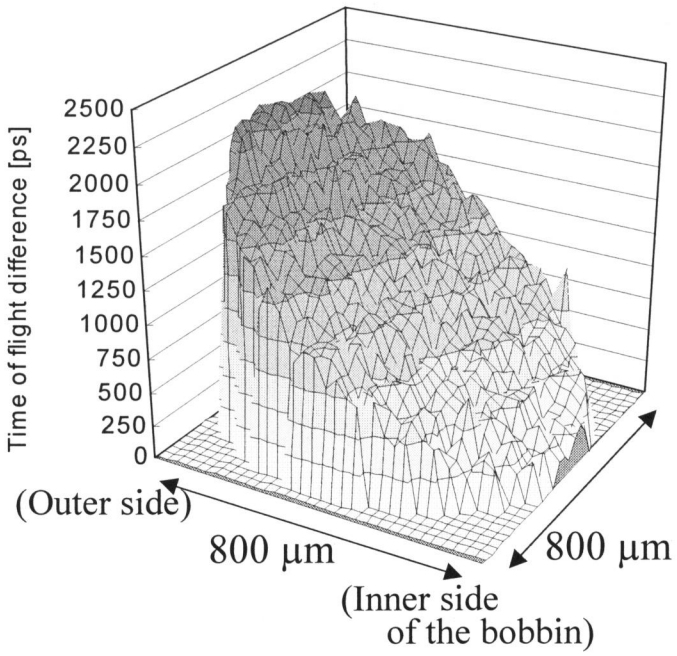

Fig. 3.10: Time-of-flight difference over the image circle (Image fiber was wound by 100 turns around a bobbin).

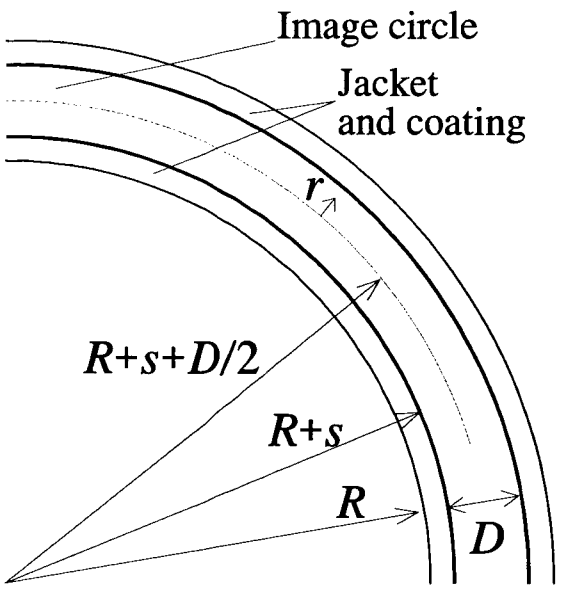

Fig. 3.11: Parameters of an image fiber wound around a bobbin.

Here, the bending-induced skew is theoretically analyzed. Assume that an image fiber is wound by m turns around a bobbin of radius R as shown in Fig. 3.11. The propagation delay τ due to an image fiber of length l is expressed by

$$\tau = \frac{Nl}{c} \tag{3.1}$$

where c and N are the speed of light in vacuum and the group index of the cores, respectively. The bending of the image fiber causes strain Δl in the axial direction and change of core refractive index Δn due to photoelastic effect. The propagation delay difference $\Delta\tau$ due to Δl and Δn is expressed as

$$\Delta\tau = \frac{N}{c}\Delta l + \frac{l}{c}\frac{\partial N}{\partial n}\Delta n\,. \tag{3.2}$$

The strain Δl on a core at a point of r is

$$\begin{aligned}\Delta l &= 2\pi m\left(R + s + \frac{D}{2} + r\right) - 2\pi m\left(R + s + \frac{D}{2}\right) \\ &= 2\pi mr\end{aligned} \tag{3.3}$$

where D and s are the picture diameter and the thickness of the jacket and coating of the image fiber, respectively. Next, we derive Δn. The core refractive index n under the photoelastic effect is expressed as [45], [46]

$$n = \sqrt{n_1^2 + 2n_1CW + C^2W^2} \tag{3.4}$$

where n_1 is the refractive index without strain, C is the lateral photoelastic constant (C = -4.19×10^{-12} m^2/N for silica glass), and W is the tensile stress. When the radius of curvature is larger than the minimum bending radius, $|CW/n_1| << 1$ is satisfied generally (see Appendix B). Therefore, from Eq. (3.4), the refractive index change is approximately expressed as

$$\Delta n = n - n_1 \cong CW. \tag{3.5}$$

Hooke's law and Eq. (3.3) can be used to express the tensile stress W as

$$W = \frac{\Delta l}{l}E = \frac{2\pi mr}{l}E \tag{3.6}$$

where E is Young's modulus (E = 7.60 × 10^{10} N/m^2 for silica glass). From Eqs. (3.5) and (3.6), Δn is written as

$$\Delta n = C\left(\frac{2\pi mr}{l}E\right). \tag{3.7}$$

By using Eqs. (3.2), (3.3), and (3.7), $\Delta\tau$ can be expressed as

$$\begin{aligned}\Delta\tau &= \frac{N}{c}(2\pi mr) + \frac{l}{c}\frac{\partial N}{\partial n}\cdot C\left(\frac{2\pi mr}{l}E\right) \\ &= 2\pi mr\left(\frac{N}{c} + \frac{CE}{c}\frac{\partial N}{\partial n}\right).\end{aligned} \tag{3.8}$$

It should be noted that the change of the propagation delay $\Delta\tau$ does not depend on the radius of the bobbin and the structural parameter of the image fiber such as the picture diameter D and

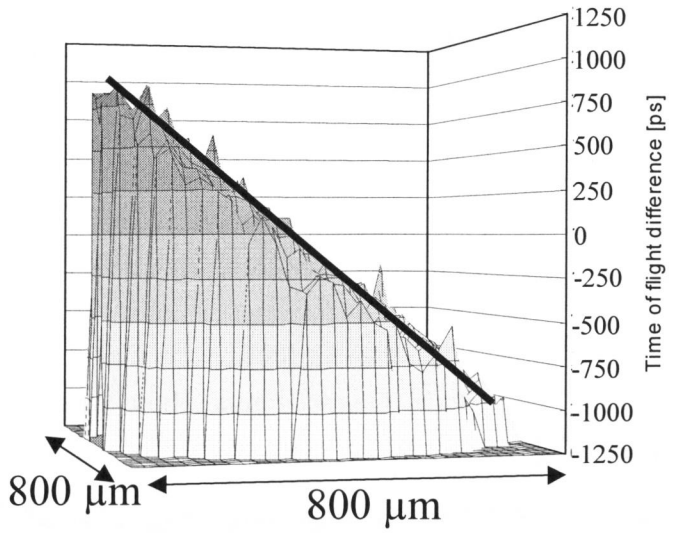

Fig. 3.12: Time-of-flight difference over the image circle. Theoretical data and experimental data (Image fiber was wound by 100 turns around a bobbin).

thickness of jacket and coating s but it depends only on the number of turns of winding m. Figure 3.12 shows the theoretical values obtained from Eq. (3.8) with the experimental result. In the figure, each value is plotted by regarding a datum at the center of the image circle as a reference. It is noted that the calculated values agree well with the experimental result. The maximum difference of the propagation delay $\Delta\tau_{\max}$ occurs between the outermost and innermost parts, and it is expressed as

$$\begin{aligned}\Delta\tau_{\max} &= \Delta\tau\big|_{r=D/2} - \Delta\tau\big|_{r=-D/2} \\ &= 2\pi mD\left(\frac{N}{c} + \frac{CE}{c}\frac{\partial N}{\partial n}\right).\end{aligned} \tag{3.9}$$

Figure 3.13 shows the theoretical values obtained from Eq. (3.9) and the experimental results of the bending-induced skew, plotted as a function of the number of turns. In the experiment, the test 100-m-long image fiber was wound around bobbins of different radius of R = 15.5 cm and R = 25 cm. The theoretical values agree well with the experimental results, and the bending-induced skew depends only on the number of turns m. The maximum difference of the propagation delay for one turn $\Delta\tau_1$ can be expressed as

$$\Delta\tau_1 = 2\pi D\left(\frac{N}{c} + \frac{CE}{c}\frac{\partial N}{\partial n}\right). \tag{3.10}$$

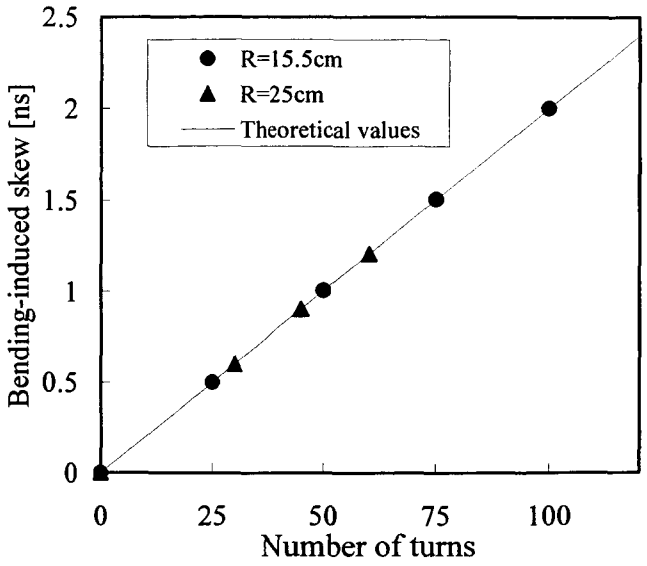

Fig. 3.13: Relation between number of turns and bending-induced skew.

Here, $\Delta\tau_1$ is an intrinsic value for each image fiber and can be used to estimate the increase in skew caused by bending. The increase in skew due to winding of m turns, $\Delta\tau_{max}(m)$, can be expressed as

$$\Delta\tau_{max}(m) = m \times \Delta\tau_1 . \tag{3.11}$$

For the test image fiber used in the measurement above, $\Delta\tau_1 = 19.8$[ps/turn]. For example, if the test image fiber is bent by 90°, consequent increase in skew can be calculated by using Eq. (3.11) as

$$\Delta\tau_{max}(1/4) = \frac{1}{4} \times 19.8 = 4.95\,[\text{ps}] . \tag{3.12}$$

In Eq. (3.10), all the values except the picture diameter D barely change if the image fiber is made of silica glass. Therefore, $\Delta\tau_1$ is characterized mainly by the value of D. The picture diameter D = 800 [μm] of the test image fiber used in the measurement above is typical for common image fibers. Therefore, we can say that $\Delta\tau_1 \cong 20$[ps/turn] is also typical. When an image fiber is used in the application of optical interconnects, it is expected that the winding can be restricted to less than about 5 turns. With this number of turns, the bandwidth limit due to the bending is higher than 1 Gbps/ch from Eq. (3.11). However, if the image fiber is wound around a bobbin over several tens turns for disposal of surplus length, a large skew of over 1 ns occurs and

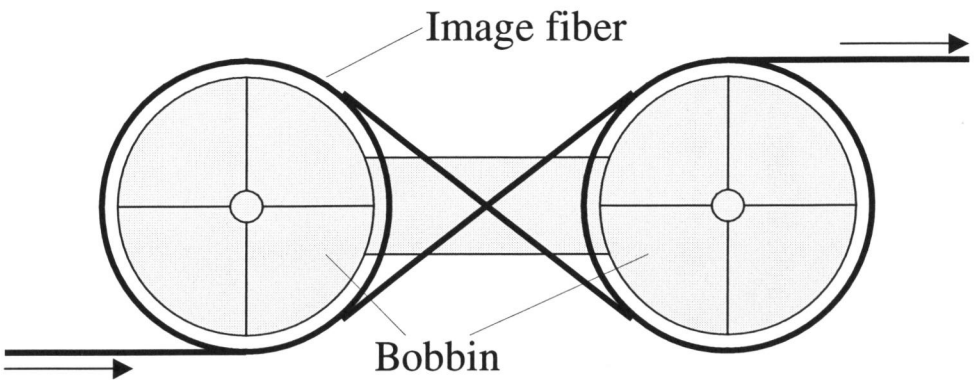

Fig. 3.14: 8-shaped bobbin for winding without increasing skew.

the bandwidth is limited to less than several hundred Mbps/ch.

One method to suppress the bending-induced skew is to twist the image fiber. When the integer multiple of the pitch of the twist is equal to the length of bent part, the increase in skew is completely canceled. Even if this condition is not satisfied, the increase in skew can be suppressed to some extent. However, fixing an image fiber in a twisted condition at every bent part makes handling difficult. It is therefore desired to realize "*twisted image fiber*" which is previously twisted in the drawing process. Another method is to use "*8-shaped bobbin*" proposed in Fig. 3.14. The surplus length of an image fiber can be disposed of without increasing skew by winding the image fiber around the bobbin in a manner to draw an "8". By using these methods, the bandwidth limit due to bending will be alleviated up to over several tens Gbps/ch.

3.4 Conclusion

In this chapter, characteristics of image fibers as parallel optical data transmission media was studied. Advantages of image fibers over the other 2-D parallel optical transmission media was clarified by comparing the advantages and drawbacks. Furthermore, image fiber skew characteristics, which is one of the most important parameters of parallel transmission media, was investigated. The skew measurement results revealed the distribution of time-of-flight difference in the image circle. To obtain high-speed transmission over 1 Gbps/ch through a 100-m-long image fiber, the parameters of all the cores have to be made uniform. Additionally, the principle of the increase in skew due to bending was clarified. Image fiber has been optimized for direct image transmission. Therefore, the parameters have to be re-optimized to realize low-skew image fibers for high-throughput 2-D parallel optical interconnects.

Chapter 4

Image fiber coupler

4.1 Introduction

One of the key devices in the image fiber based 2-D parallel optical interconnects is an image fiber coupler which branches image fibers. Image fiber couplers are needed to realize one-to-many and/or many-to-many data links such as space-CDMA systems. Image fibers can be branched simply by using beam-splitters (BSs) and lenses which image one end to other ends of the image fibers. However, the compact and reliable assembly and ease of optical alignment are required.

In this chapter, a novel concept of the image-fiber branching and a simple construction using graded index (GRIN) rod lenses is proposed [19]. Characteristics of GRIN rod lenses in free-space optical interconnects have been investigated [3], [47], [48]. The image fiber coupler consists of GRIN rod lenses, a miniature cube BS, and V-grooves. This lens system has the focal points on the end surfaces of the GRIN rod lenses. Therefore, optical alignment with image fibers can be achieved simply by butt-joints on the V-grooves. Recently, other types of image fiber couplers was reported by Ai et al. [49], [50]. Section 2 presents the design and implementation of the image fiber coupler. In this section, required lens parameter conditions such as numerical aperture (NA), lens diameter, and size of BS are clarified by theoretical analysis. In Section 3, experimental characterizations are described to clarify contrast degradation and vignetting loss characteristics. Section 4 describes a structure of an image fiber based optical interconnect module and 2-D optical amplifier systems using erbium-doped image fiber amplifier (EDIFA) as applications which use the image fiber couplers not to branch image fibers.

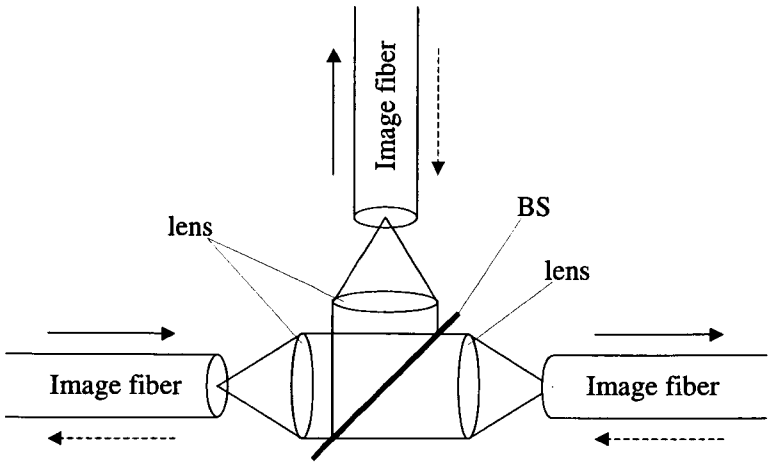

Fig. 4.1: Schematic diagram of an image-fiber branching by imaging lenses and a BS.

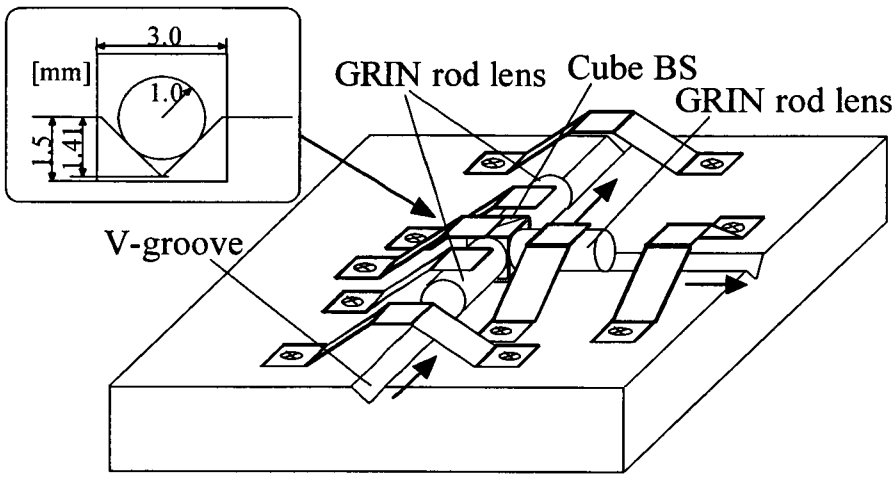

Fig. 4.2: Schematic diagram of an image fiber coupler which consists of GRIN rod lenses, cube BS, and V-grooves.

4.2. Design and implementation of an image fiber coupler

4.2.1 Construction of an image fiber coupler

To realize one-to-many and/or many-to-many data links such as space-CDMA systems described in Chapter 2, image fiber couplers which branch image fibers are needed. The output of image fiber can be branched simply by using BSs and lenses which image one endface onto other endfaces of the image fibers as schematically shown in Fig. 4.1. However, the compact and reliable assembly and ease of optical alignment are required to achieve cost-effectiveness. Figure 4.2 schematically shows a proposed image fiber coupler using GRIN rod lenses, a miniature cube BS,

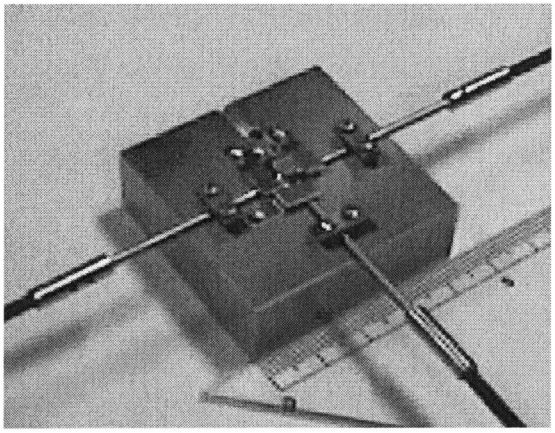

Fig. 4.3: Photograph of an image fiber coupler connecting three branches of image fibers.

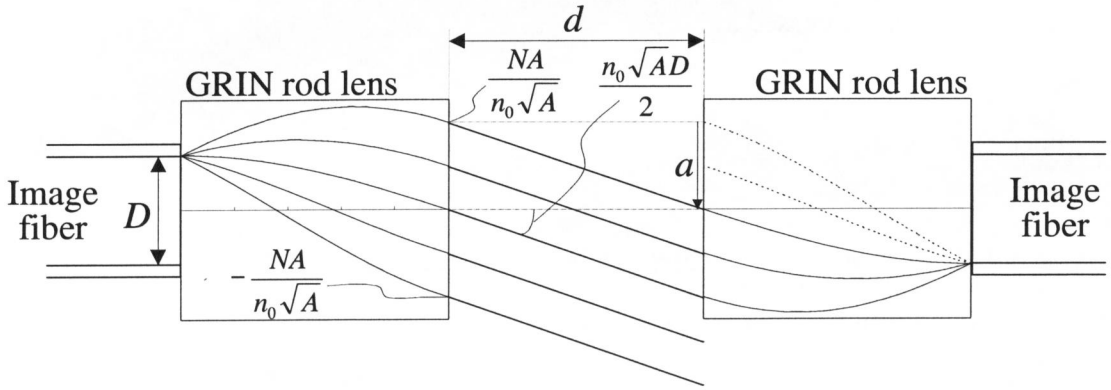

Fig. 4.4: Parameters of an imaging lens system coupling image fiber branches.

and V-grooves [19]. The component sizes in the fabricated image fiber coupler are shown in the inset. A photograph of a fabricated image fiber coupler connecting three branches of image fibers is shown in Fig. 4.3. All the components are of off-the-shelf and commercially available. This imaging lens system has the focal points on the end surfaces of the GRIN lenses. Therefore, optical alignment with image fibers can be achieved simply by butt-joints on the V-grooves.

4.2.2 Parameter design of image fiber coupler

In this subsection, the proposed image fiber coupler is analyzed theoretically, and the required parameter conditions such as NA, lens diameter, and size of BS are clarified. Figure 4.4 schematically shows the imaging system and parameters of each component. Here, we use GRIN rod lenses of 0.25 in pitch. 0.25-pitch GRIN rod lenses are inexpensively supplied as standardized specifications. Furthermore, focal points are on the end surfaces regardless of distance between

GRIN rod lenses d, at which a cube BS with edge length d is sandwiched. Ray matrix of GRIN lens of 0.25 in pitch is expressed as

$$M = \begin{bmatrix} 0 & \dfrac{1}{n_0\sqrt{A}} \\ -n_0\sqrt{A} & 0 \end{bmatrix} \tag{4.1}$$

where n_0 and A are on-axis refractive index and squared gradient constant, respectively. Incident light from a core in an image fiber of input side (left side in Fig. 4.4) is collimated by the GRIN rod lens. Radius of the beam is $\mathrm{NA}/n_0\sqrt{A}$ where NA is numerical aperture of the image fiber. The angle of the beam θ is expressed as

$$\tan\theta = -n_0\sqrt{A}r_1 \tag{4.2}$$

where r_1 is radial position of the incident light. If the light is incident from outermost cores, the angle takes the maximum value $\theta_{\max}$ expressed as

$$\tan\theta_{\max} = -\frac{n_0\sqrt{A}D}{2}. \tag{4.3}$$

This angle of the beam causes lateral shift of incident light a on the next GRIN lens (right side in Fig. 4.4) and, consequently, vignetting loss. A condition to suppress the vignetting loss at outermost point less than 3 dB (Condition 1) can be expressed as

$$D < \frac{4n_1}{\left(n_0\sqrt{A}\right)^2\left(d/0.4\right)} \cdot \mathrm{NA} \tag{4.4}$$

where n_1 is the refractive index of the cube BS sandwiched between the GRIN rod lenses. If the cube BS is small enough, the beam with some angle reflects on the surfaces of the cube BS, and it causes ghost and flare. To prohibit the reflection by the cube BS (Condition 2), a condition expressed below has to be satisfied.

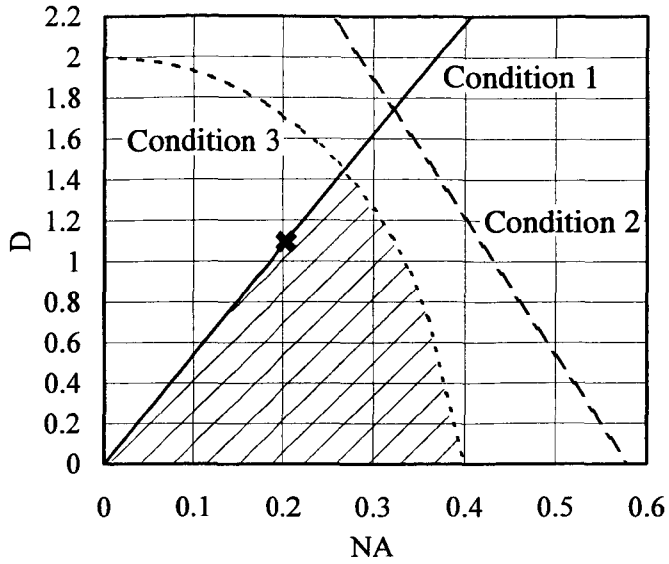

Fig. 4.5: Possible domain of NA and Picture diameter D of image fibers coupled by an image fiber coupler using GRIN rod lens (n_0 = 1.564, SQRT(A) = 0.2466, r_1 = 1.0 mm) and a cube BS (d = 3.0 mm, n_1 = 1.515).

$$D < \frac{n_1}{n_0\sqrt{A}}\left(1-\frac{2\mathrm{NA}}{n_0\sqrt{A}d}\right). \tag{4.5}$$

In addition to these Conditions 1 and 2, the GRIN rod lens of input side has to have larger NA than that of the image fiber at any incident points (Condition 3). This condition is express as

$$D < 2\sqrt{r_0^2-\left(\frac{NA}{n_0\sqrt{A}}\right)^2} \tag{4.6}$$

where r_0 is the radius of the GRIN rod lens. In the test image fiber coupler, GRIN rod lenses fabricated by Nippon Sheet Glass (S20S025N063N, n_0 = 1.564, $\sqrt{A}$ = 0.2466 mm^{-1}, r_0 = 1.0 mm) were used. The edge length d of the cube BS (BK7, n_1 = 1.515) is 3 mm. The conditions expressed by Eqs. (4.4), (4.5), and (4.6) for the test image fiber coupler are plotted in Fig. 4.5. The parameters NA and D of image fibers branched by the coupler have to be in the shadowed domain to satisfy Conditions 1, 2, and 3. Image fibers prepared to be branched by the image fiber coupler have 10^4 cores. NA and image diameter are 0.2 and 1.1 mm, respectively as denoted by a cross in Fig. 4.5. Conditions 1, 2, and 3 expressed by Eqs. (4.4), (4.5), and (4.6) can be rewritten as follows.

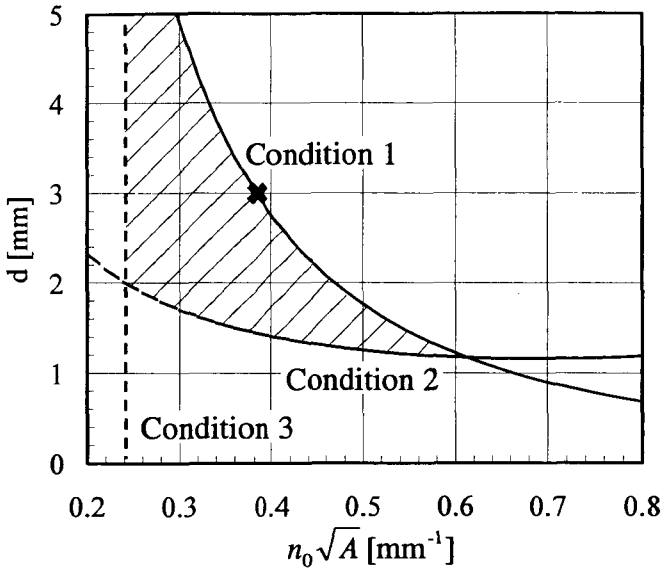

Fig. 4.6: Possible domain of the size of cube BS d and GRIN-rod-lens parameter n_0SQRT(A) of image fiber couplers which can branch image fibers (NA = 0.2, D = 1.1 mm).

Condition 1:

$$d < 0.4 \cdot \frac{4n_1 \mathrm{NA}}{D} \cdot \frac{1}{\left(n_0\sqrt{A}\right)^2}. \tag{4.7}$$

Condition 2:

$$d > \frac{2n_1 \mathrm{NA}}{n_0\sqrt{A}\left(n_1 - n_0\sqrt{A}D\right)}. \tag{4.8}$$

Condition 3:

$$n_0\sqrt{A} > \frac{\mathrm{NA}}{\sqrt{r_0^2 - \left(D/2\right)^2}}. \tag{4.9}$$

By using the parameters NA and D of the prepared image fibers, Condition 1, 2, and 3 can be plotted as shown in Fig. 4.6. Here, it is assumed that the cube BS is made of BK7 (n_1 = 1.515) and the radius of the GRIN rod lens r_0 = 1.0 mm. The parameters d and $n_0\sqrt{A}$ of image fiber couplers which branch the prepared image fiber have to be in the shadowed domain to satisfy Conditions 1, 2, and 3. By using this graph of Fig. 4.6, proper type of GRIN rod lenses and size of cube BSs can be selected. The parameters of the fabricated image fiber coupler are denoted by a cross in the figure.

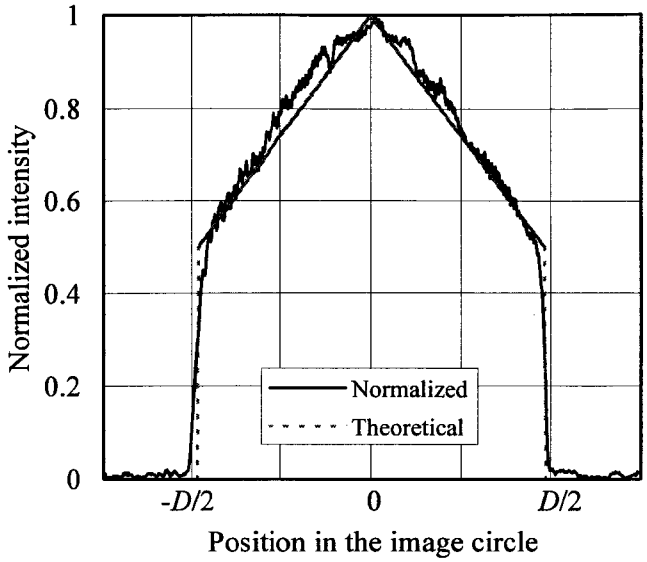

Fig. 4.7: Vignetting loss characteristics of an image fiber coupler Theoretical data and experimental data.

4.3 Experimental characterization

4.3.1 Vignetting loss

The fabricated image fiber coupler with the prepared image fibers was evaluated experimentally. Expected vignetting loss at outermost points is 3 dB because the parameters of the image fibers is just on the bound of Condition 1 in Fig. 4.5. Figure 4.7 shows measured vignetting loss. Theoretical values are also shown by dotted lines. It is noted that the experimental result agrees well with the theoretical values. To restrict the vignetting loss, parameter point of image fibers have to be farther from the bound of Condition 1.

4.3.2 Contrast degradation

To evaluate the resolution performance, United States Air Force (USAF) test chart images transmitted by the image fiber with and without the image fiber coupler were compared. In Fig. 4.8, the measured contrast is shown as a function of spatial frequency in lp/mm. Some contrast degradation was observed in spite of the high contrast of the GRIN rod lenses and the cube BS. It should be noted that this degradation is not caused by the image fiber coupler but by image fiber connection itself. Light from one core in the input image fiber is imaged on several cores in the next

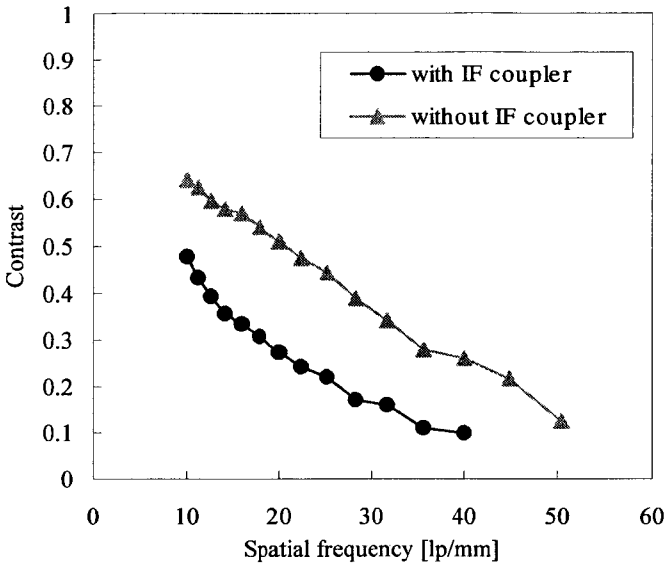

Fig. 4.8: Contrast degradation due to an image fiber coupler.

image fiber. One-to-one connection between the cores is difficult to achieve. The degradation caused by this "misalignment" is inherent to the connection of image fibers.

4.4 Applications of image fiber couplers

Image fiber coupler is needed to realize image fiber based one-to-many and/or many-to-many data links such as space-CDMA systems. However, it is useful in other applications. This section describes a novel structure of an image fiber based optical interconnect module and 2-D optical amplifier systems using EDIFA as applications which use the image fiber couplers not to branch image fibers.

4.4.1 Optical alignment in image fiber based 2-D parallel optical interconnect modules

Schematic diagram of our proposed image fiber based 2-D parallel optical interconnect module using an image fiber coupler is shown in Fig. 4.9 [26]. In this module, the image fiber coupler is used for optical alignment. Since optical signals from VCSEL array and PD array can be observed by an camera via the image fiber coupler, the optical alignment can be achieved visually. The optical alignment is achieved as follows [26]. The VCSEL array and the lens of the transmitter are optically aligned by directly connecting a camera to the output end of the image fiber and visually

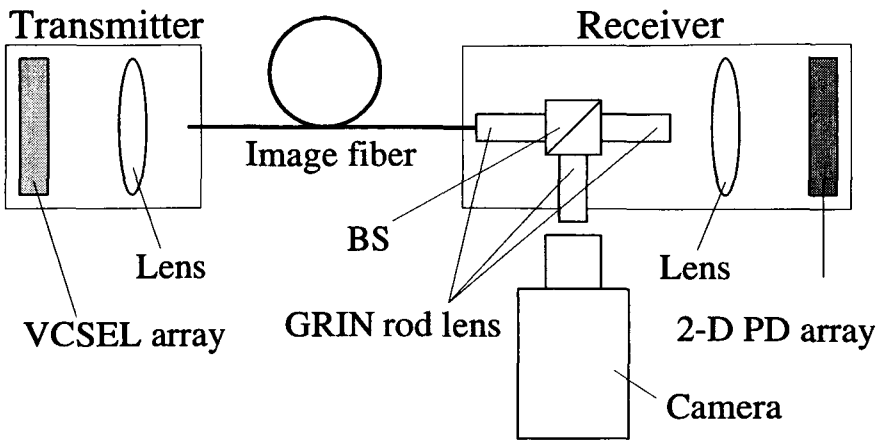

Fig. 4.9: Schematic diagram of an image fiber based 2-D parallel optical interconnect module using an image fiber coupler for optical alignment.

monitoring the output image. After aligning the transmitter, the output end of the image fiber is butt-jointed to a GRIN rod lens on a V-groove, because the focal points of the GRIN rod lens are on its end surfaces. The PD array and the lens in the receiver are optically aligned by using camera to simultaneously monitor the VCSEL and PD arrays. Optical signals that propagate through the image fiber are reflected by the PD array and observed by the camera. By injecting a forward current into the PD array, it operates as an array of light-emitting diodes (LEDs). Therefore, an image that results from the superimposing of incident optical signals from the VCSEL array and light emitted from the PD array can be viewed through the image fiber coupler by using the camera. The PD array and the lens are so adjusted that each optical signals falls on its corresponding target. It should be noted that the structure and alignment method are so simple that cost-effective optical interconnection modules are possible to be realized [26]. Details of the optical alignment and transmission experiments using the modules will be described in Chapter 6.

4.4.2 2-D optical amplifier systems using erbium-doped image fibers

Erbium-doped image fiber amplifiers (EDIFAs) have been investigated to realize 2-D optical amplifier systems [20]. In this system, image fiber couplers are usefully applied. EDIFAs can be used to compensate branching loss in 2-D parallel image fiber networks. Additionally, they are applicable in image processing and 2-D optical data processing systems. Figure 4.10 schematically shows pumping method for an EDIFA. In the pumping method, an image fiber coupler is used to multiplex signal beam and pump beam. All the cores of the EDIFA are pumped by the pumping method. Therefore, not only discrete optical spots but also spatially continuous images can be

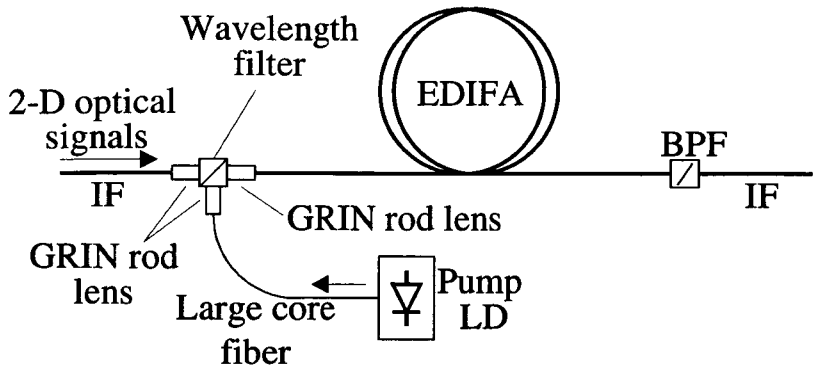

Fig. 4.10: Pumping method using an image fiber coupler for an EDIFA.

amplified. The pump beam is launched from a large core fiber which has the same diameter as that of the EDIFA. The output end of the large core fiber is imaged on the input end of the EDIFA through the image fiber coupler with cube wavelength filter. Details of the pumping method and characteristics of fabricated test EDIFAs will be described in Chapter 5.

4.5 Conclusions

Design, characteristics, and applications of image fiber couplers using GRIN rod lenses were described. The proposed image fiber coupler has the features including compact and reliable assembly and ease of optical alignment. Image fiber couplers are useful not only for image-fiber branching but for many other applications such as optical alignment of image fiber based optical components and wavelength coupling. This investigation will help the development of future image fiber optical systems including 2-D parallel optical interconnects.

Chapter 5

Erbium-doped image fiber amplifier (EDIFA)

5.1 Introduction

Some 2-D parallel optical interconnect systems that interconnect several 2-D opto-electronic devices have been tested previously [22-23]. In these systems, branching loss is one of the most serious problems, because the 2-D optical signals are branched repeatedly to enable data links between many devices. Therefore, a 2-D optical amplifier is needed to compensate for this loss. The 2-D optical amplifiers can be used in the same way as conventional Er-doped fiber amplifiers (EDFAs) in optical communication systems, and they also compensate for transmission loss. Additionally, 2-D optical amplifiers are applicable in image-processing and 2-D optical-data-processing systems. They will thus become key devices in future optical computing systems.

In this chapter, a 2-D Er-doped image-fiber amplifier (EDIFA) is described [20]. Section 5.2 describes applications of 2-D optical amplifiers. The EDIFA is compared with a conventional 2-D optical amplifier based on a semiconductor optical amplifier having a vertical-cavity surface-emitting laser structure. Pumping methods for the EDIFA are also proposed. Section 5.3 gives the specifications of the fabricated test EDIFAs. In Section 5.4, the measured gain characteristics of the test EDIFAs are presented. In Section 5.5, the measurements are compared with the characteristics of a single-core reference Er-doped fiber pulled from the same core preform. Finally, ways to achieve higher-gain EDIFAs are suggested.

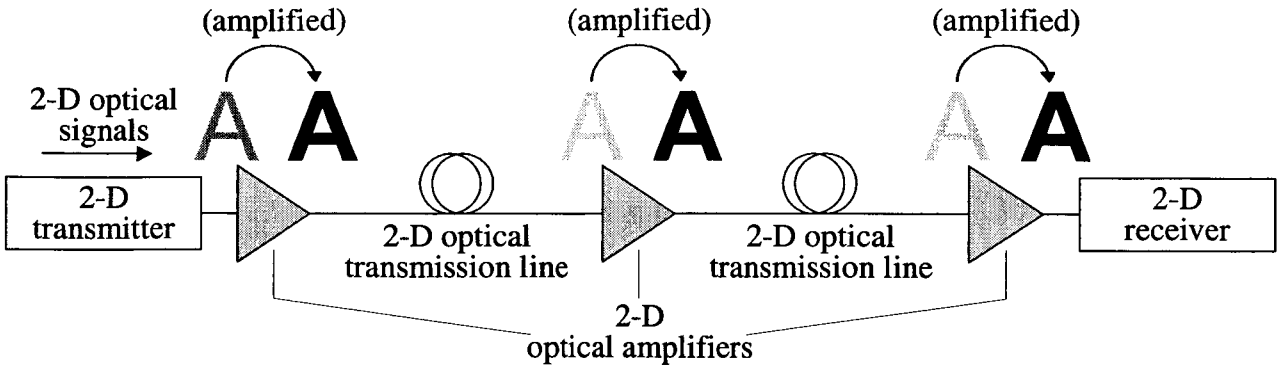

Fig. 5.1: Generic 2-D parallel optical data link with 2-D optical amplifiers.

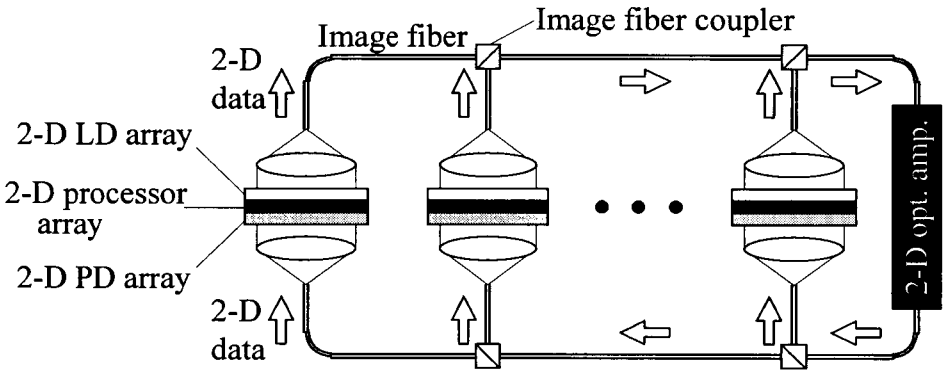

Fig. 5.2: Image-fiber-based 2-D parallel optical bus system with 2-D optical amplifier interconnecting 2-D processor arrays.

5.2 Two-dimensional optical amplifier

5.2.1 Applications of two-dimensional optical amplifiers

Image-fiber-based 2-D parallel optical interconnect systems have previously been investigated, in which 2-D optical signals are multiplexed and transmitted through an image fiber. [11]. A few other 2-D parallel optical interconnect systems using free-space optics have been also demonstrated [23]. In these systems, branching loss is one of the most serious problems because 2-D optical signals have to be split or tapped along data link that connects many terminals. A 2-D optical amplifier seems to be an ideal way to compensate for this loss. Figure 5.1 schematically shows a generic 2-D parallel optical data link with 2-D optical amplifiers. The 2-D optical signals are amplified in parallel by the amplifiers. 2-D optical amplifiers can be used in the same way as conventional EDFAs in optical communication systems, and they also compensate for transmission loss. Figure 5.2 shows an example of an image-fiber-based 2-D parallel optical bus system with a 2-

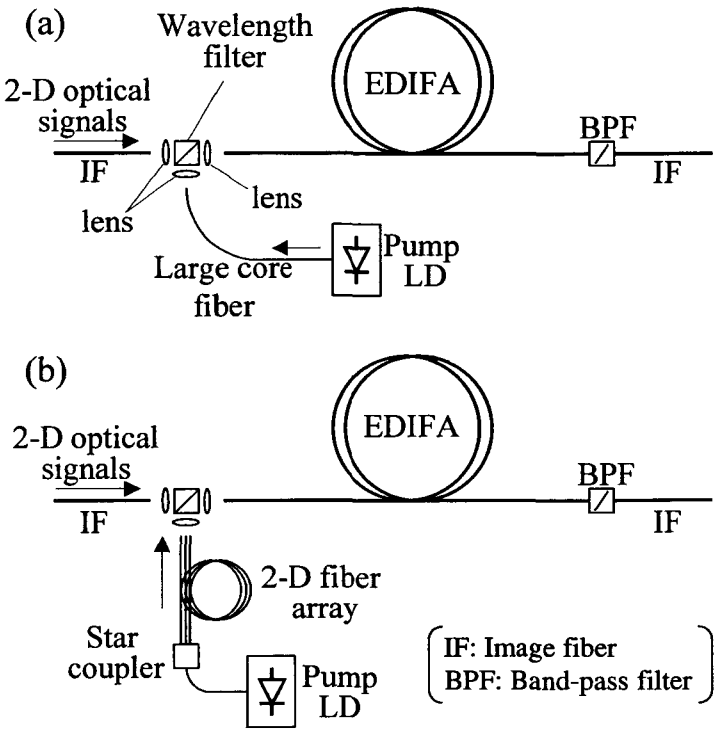

Fig. 5.3: Pumping methods for EDIFAs in forward pumping: (a) all cores are pumped, (b) pump power concentrated on signal beams.

D optical amplifier interconnecting 2-D processor arrays. In addition to these network systems, 2-D optical amplifiers are applicable in image-processing and 2-D optical-data-processing systems. They will thus become key devices in future optical computing systems.

5.2.2 EDIFA and pumping methods

Semiconductor optical amplifiers (SOAs) with a VCSEL structure would be one possible candidate for 2-D optical amplifiers[51], [52]. A VCSEL-based SOA itself has advantages including the minimal insertion loss and the polarization insensitivity. Its high suitability for 2-D integration is also attractive from the viewpoint of 2-D optical systems. However, SOAs have some drawbacks, including a low output saturation power and low gain compared to fiber-based optical amplifiers. 2-D optical signals can be amplified only on the spatially discrete points where VCSEL based SOAs are arranged.

Compared to VCSEL-based SOAs, our proposed 2-D EDIFAs can amplify 2-D optical signals independently of its array size and geometric configuration. Furthermore, EDIFAs can directly amplify 2-D optical signals of spatially continuous images. Therefore, it should also be applicable to optical computing requiring cascade logic operation [1], and to Fourier optics, such as pattern-

recognition-based on optical correlation in space [53]. The EDIFAs should also achieve a higher output saturation power and gain than VCSEL based SOAs.

Figure 5.3 schematically shows pumping methods for EDIFAs. In Fig. 5.3(a), all the EDIFA cores are pumped. Therefore, not only discrete optical spots but also spatially continuous images are amplified. The pump beam is launched from a large-core fiber that has the same diameter as the EDIFA. The output end of the fiber is imaged on the input end of the EDIFA through a wavelength filter used to multiplex signal and pump beams. However, a high number of cores requires an extremely high pump power. When the 2-D optical signal is optical spots, the pumping method shown in Fig. 5.3(b) can be used, where the pump beams are launched from a 2-D fiber array [39-42]. The pump power is concentrated on the optical signal beams only. In Fig. 5.3, the pumping methods are explained in forward pumping. However, backward and bi-directional pumping can also be applied in the same way.

5.3 Test EDIFA and its characteristics

5.3.1 Test EDIFA

A 0.8- and a 3.0-m-long EDIFA are prepared. The doping concentrations were approximately 500 ppm for the 0.8-m fiber and 1000 ppm for the 3.0-m fiber. Al was codoped in the core preform with a 0.1% concentration. The specifications are summarized in Table 5.1. The Er-dopant in the core changes the viscosity of the preform, resulting in bubbles in the EDIFAs during the drawing process. To avoid this problem, the viscosity of the cladding was balanced by tailoring the concentration of fluorine, and the viscosity of the cladding was matched to that of the cores. Figures 5.4(a) and (b) show the cross-sectional view of the 0.8-m-long EDIFA and the optical signals after propagation, respectively. Some dark spots still remained due to the bubbles. To eliminate bubbles completely requires optimizing the dopants concentrations. This will be a next subject to be studied.

Table 5.1: Specifications of fabricated EDIFAs

Parameter	Specification
Number of pixels	3,000
Fiber diameter	630 μm
Picture diameter	590 μm
Core diameter	4.5 μm
Spacing between pixels	9.0 μm
NA	0.25

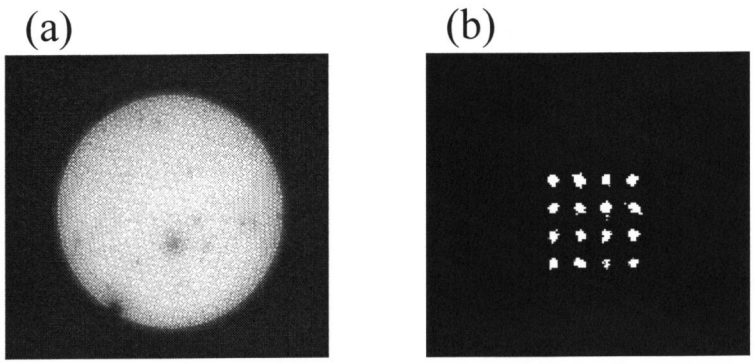

Fig. 5.4: (a) Cross section of 0.8-m-long EDIFA and (b) output signals after propagation through the 0.8-m EDIFA.

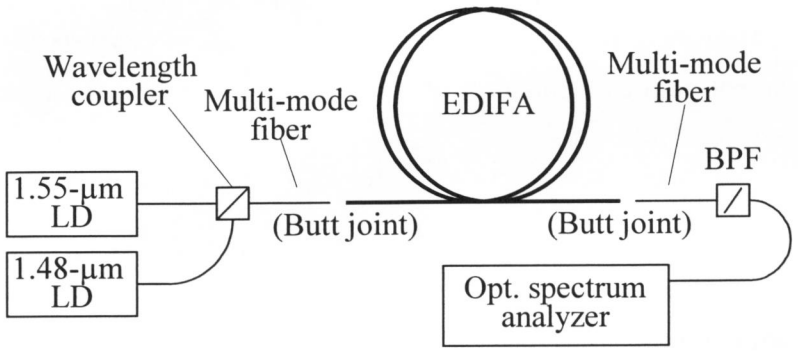

Fig. 5.5: Experimental setup for measuring EDIFA gain characteristics.

5.3.2 Experimental results

For measuring the gain characteristics of the test EDIFAs, the experimental setup shown in Fig. 5.5 was used to simplify the pumping. Signal (1.55 μm) and pump (1.48 μm) beams were launched from a multi-mode fiber (62.5/125 μm) butt-jointed on the input endface of the EDIFAs. The signal and pump beams from the multi-mode fiber propagated through about 30 cores of the EDIFAs. After the propagation, the beams were launched into a multi-mode fiber. The signal power was measured with an optical spectrum analyzer.

The measured gains for the 0.8- and 3.0-m-long EDIFAs are shown in Figs. 5.6(a) and (b), respectively. The gains were measured by changing the power of the signal and pump beams. Here, the gain G is defined as the ratio of the output-signal power with pumping to the output-signal power without pumping

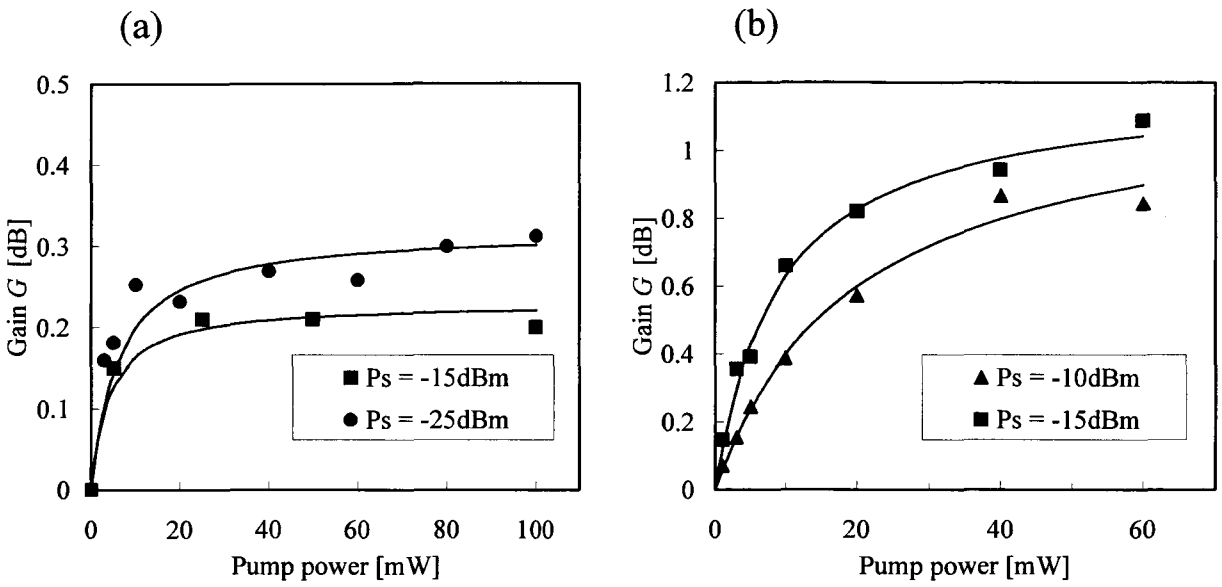

Fig. 5.6: EDIFA signal gain as a function of input pump power: (a) 0.8 m and (b) 3.0 m (P_s = signal power).

$$G = \frac{P_s(\text{with pumping})}{P_s(\text{without pumping})}. \tag{5.1}$$

This gain is thus independent of the loss at the input end of the EDIFAs (see Appendix C). We used this definition because the loss at the input end varies slightly depending on where the multi-mode fiber is butt-jointed. This loss variation is caused by a variation in the number of cores, which transmit the signal-beam, depending on the butt-joint position. Figure 5.6 also shows the theoretical gain predictions [54]. In the calculations, the propagation loss of the signal and pump beams were neglected because the EDIFAs were short. With this assumption, the measured gains vs. the pump power characteristics agree with the theoretical predictions. The gains saturated at less than 0.4 and 1.2 dB, respectively. We have to note that pumping efficiency was low because the EDIFA cores are multi-moded at 1.55 and 1.48 μm.

5.3.3 Discussion

For comparison, we also prepared a single-mode, single-core Er-doped fiber using the same core preform as that for the 3.0-m-long EDIFA. The core diameter, the relative-index difference, the cutoff wavelength, and the length of the reference fiber were 2.9 μm, 2.9%, 1.4 μm, and 10 m. The

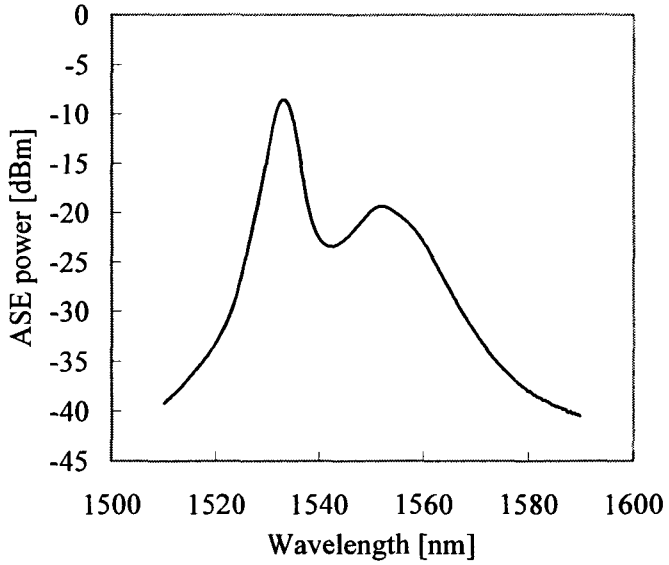

Fig. 5.7: ASE spectrum measured using reference optical fiber.

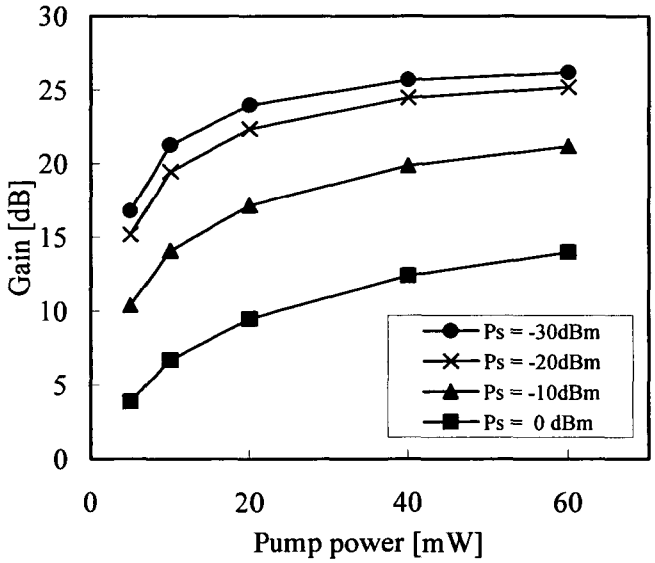

Fig. 5.8: Signal gain of reference optical fiber as a function of input pump power (P_s = signal power).

amplified spontaneous emission (ASE) spectrum of the reference fiber is shown in Fig. 5.7. The gain peaked 1533 and 1552 nm, and the corresponding 3-dB bandwidths were 4.5 nm (574 GHz) and 13.4 nm (1.67 THz). The gain characteristics of the reference fiber are shown in Fig. 5.8. Here, the characteristics of the reference fiber was normally measured without using the definition Eq. (5.1).

The reference fiber had a gain of over 20 dB for its length of 10 m regardless of using dopants to control the viscosity of cladding and cores. Enhancing the EDIFA gain requires optimizing the

EDIFA parameters. The dopant concentrations used to control the viscosity need to be optimized to eliminate bubbles completely, and longer EDIFAs need to be fabricated. Furthermore, the core parameters have to be designed so that the EDIFAs are single-mode at 1.48 μm to increase the pumping efficiency. Pulling an EDIFA up to 10 m would enable a gain of over 20 dB.

5.4 Conclusion

In this chapter, EDIFA based 2-D optical amplifiers have been demonstrated experimentally. Pumping methods were also discussed. To achieve higher gain, the dopant concentrations used to control the viscosity need to be optimized to eliminate bubbles and to pull longer EDIFAs. Furthermore, the core parameters need to be designed so that the EDIFAs are single-mode at a 1.48-μm wavelength to increase the pumping efficiency. The proposed EDIFA will open up new applications of image fibers to long-distance 2-D optical interconnects, including those for remote sensing in non-human-friendly environments, such as battlefields.

Chapter 6

Experimental demonstrations of 2-D parallel optical interconnects based on space-CDMA

6.1 Introduction

Image fiber is a potential fiber-based optical interconnect medium. Some experimental demonstrations of image-fiber based optical interconnects have been reported [4-8]. In these demonstrations, however, image fibers were used only for point-to-point connection with one transmitter and one receiver, and multiple access of one-to-many connection remains to be developed. One method to realize the 2-D multiple access is to use a network switch [9]. Another is to employ multiplexing schemes [10]. Space-CDMA studied in Chapter 2 is one important candidate for multiplexing 2-D parallel optical signals [11], [12]. In the space-CDMA scheme, bit-signals in 2-D parallel data are encoded using 2-D spatial orthogonal code called OOSPs, and multiplexed. The receivers can decode only an intended parallel signal by correlating the received pattern with the corresponding OOSP [11]. By using the space-CDMA scheme, a number of optical 2-D channels can be established simultaneously with individual clock speed, and asynchronous transmission is possible.

This chapter describes several experimental demonstrations of image fiber optic 2-D parallel optical interconnects based on space-CDMA. Section 6.2 shows experiments of space-CDMA systems in which 2-D optical signals are generated by use of Xe lamps and spatial light modulators (SLMs) [24]. In the experiment, four channels of 64-bit (8 × 8) parallel optical signals are multiplexed and transmitted through an image fiber. Experimental demonstrations of transmission through a 100-m-long image fiber [25] and decoding using prethresholding method which is

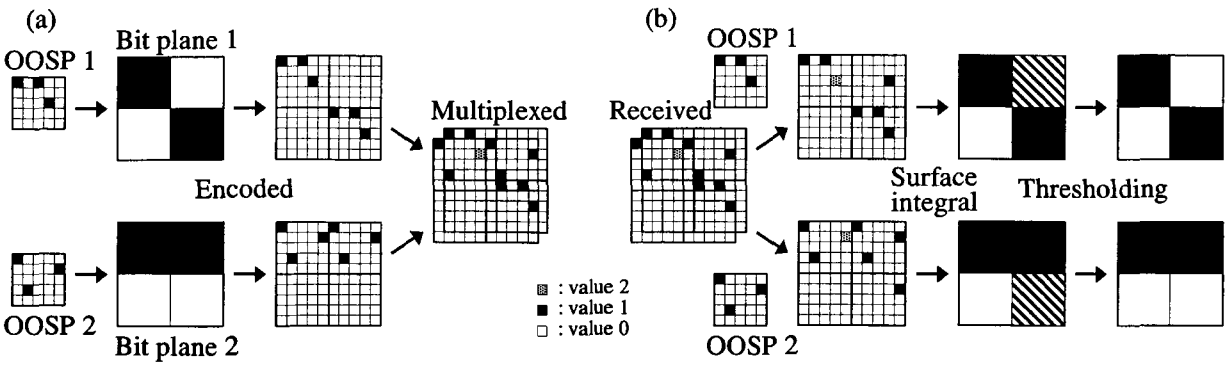

Fig. 6.1: Schematic diagrams depicting (a) spatial encoding and (b) spatial decoding.

theoretically investigated in Chapter 2 are also described [12]. In Section 6.3, high-speed space-CDMA system using 2-D VCSEL/PD arrays is described [26], [27]. In the experiment, 512-Mbps 2-D parallel transmission using 8 × 8 VCSEL/PD arrays is demonstrated. Two spatially encoded four-bit (2 × 2) parallel optical signals are emitted from the VCSEL arrays and transmitted through image fibers. After the multiplexing/demultiplexing operations, the two parallel signals are individually retrieved. Bit-error-rate (BER) performance and tolerance of lateral misalignment are given. The transmitter/receiver structure and the optical alignment method are also described.

6.2 Space-CDMA system using SLM

6.2.1 Concept of space-CDMA

In this subsection, the concept of space-CDMA, which was described in Chapter 2, is briefly summarized. The spatial encoding process is schematically shown in Fig. 6.1(a) [11]. In this example, two 2 × 2-pixel binary input bit-planes are encoded with two 5 × 5 OOSPs (weight w = 3) into a 10 × 10 multiplexed encoded pattern. These OOSPs are mutually orthogonal, so that it is possible to demultiplex these patterns, even if they are multiplexed with some shifts. The spatial decoding process is schematically shown in Fig. 6.1(b). The receiver correlates the received pattern with its own OOSP. The input bit-plane is regenerated after thresholding operation on the correlation output.

Each OOSP can be expressed in matrix notation as

$$\mathbf{E}^{(q)} = \begin{bmatrix} e_{11}^{(q)} & e_{12}^{(q)} & \bullet & \bullet & \bullet & e_{1M}^{(q)} \\ e_{21}^{(q)} & e_{22}^{(q)} & \bullet & \bullet & \bullet & e_{2M}^{(q)} \\ \bullet & \bullet & \bullet & & & \bullet \\ \bullet & \bullet & & \bullet & & \bullet \\ \bullet & \bullet & & & \bullet & \bullet \\ e_{M1}^{(q)} & e_{M2}^{(q)} & \bullet & \bullet & \bullet & e_{MM}^{(q)} \end{bmatrix}, \tag{6.1}$$

where the matrix elements $e_{i,j}^{(q)}$ take binary values of 0 or 1, and each value corresponds to each chip pixel of the qth OOSP. The number of binary 1s in the matrix is the weight w of the OOSPs. The value M is the size of OOSPs (or M^2 is called the spreading factor). The orthogonality of OOSPs can be achieved under two constraints:

(1) Signature patterns must be distinguishable from any space-shifted versions of themselves in the 2-D plane.

(2) Any two different signature patterns in a set must be distinguishable from one another, even if any vertical and/or horizontal space shifts exist in the 2-D plane.

Here, the possibility of encoded-pattern rotation after transmission is ruled out. These constraints require that autocorrelation must be much higher than the correlation side lobes, and any peaks in the cross-correlation function must be much lower than the peak for the autocorrelation function. These requirements can be expressed in binary discrete correlation forms as:

$$\sum_{i=1}^{M}\sum_{j=1}^{M} e_{i,j}^{(q)} e_{i+k,j+l}^{(q)} \begin{cases} = w & \text{for } k = l = 0 \\ \le \lambda_a & \text{for } 1 \le k,l \le M-1 \end{cases} \tag{6.2}$$

and

$$\sum_{i=1}^{M}\sum_{j=1}^{M} e_{i,j}^{(q)} e_{i+k,j+l}^{(q')} \le \lambda_c \quad \text{for } q \ne q', 0 \le k,l \le M-1. \tag{6.3}$$

Here, λ_a and λ_c are called autocorrelation constraint and crosscorrelation constraint, respectively [11].

6.2.2 Optical implementation and experimental setup

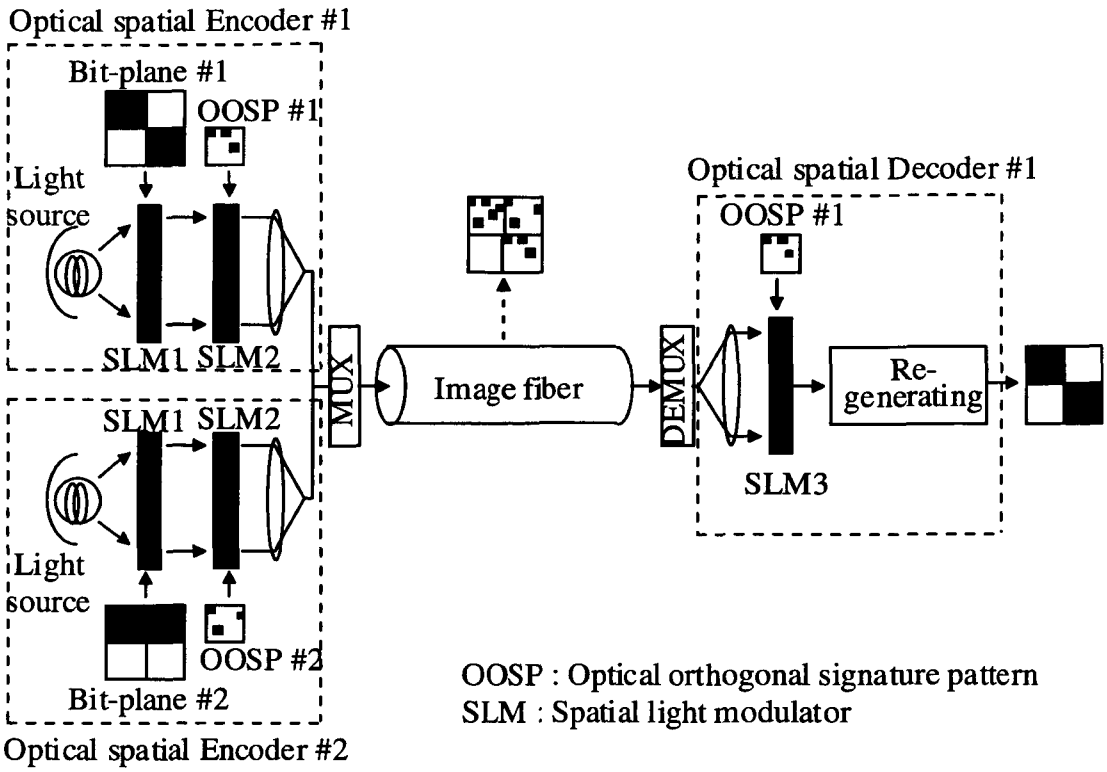

Fig. 6.2: Optical implementation of a space-CDMA network. MUX, multiplexer; DEMUX, demultiplexer.

Parallelism of optical computations is exploited for the spatial encoding and decoding. Figure 6.2 schematically shows the optical implementation of the optical space-CDMA network. The transmitter consists of an optical spatial encoder. The receiver consists of an optical spatial decoder and a thresholding device. An image fiber is used as the transmission medium which has a large number of cores in a common cladding. The encoder and decoder consist of SLMs.

In the encoder, an input bit plane and OOSP are addressed electrically on the SLM1 and SLM2, respectively. By reading out SLM1 and SLM2 in order with the light beam, the encoding for all bits is optically done in parallel. The SLM1s can be replaced by VCSEL arrays easily to increase the system throughput. The encoded patterns are superimposed by MUX, and the multiplexed bit plane is launched into an image fiber and transmitted in parallel. At the receiver side, the multiplexed bit plane is broadcast to every decoder by DEMUX. In Fig. 6.2, there is only one decoder. The decoder performs in parallel the correlations of all bits of the received one and its own OOSP addressed on the SLM3. After performing the surface-integral and thresholding, the intended input bit plane is regenerated.

The experimental setup is based upon the optical implementation shown in Fig. 6.2. The optical

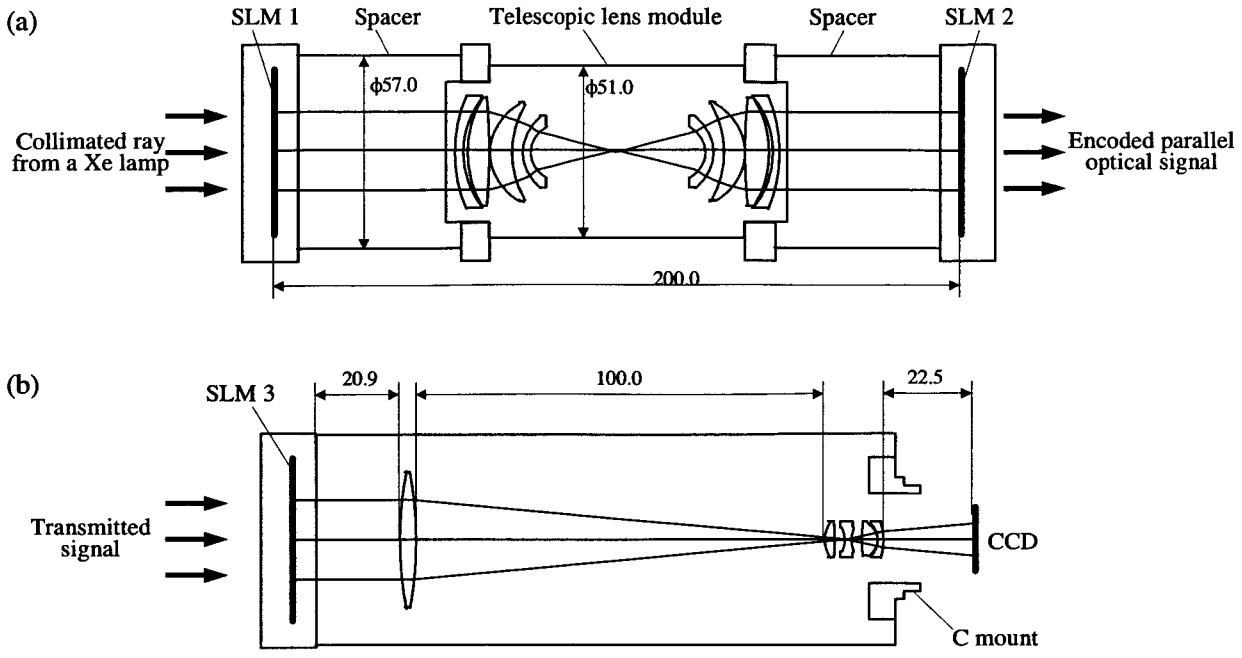

Fig. 6.3: Schematic diagrams of (a) an optical spatial encoder module and (b) an optical decoder module.

spatial encoders and decoders were fully modularized to improve the performance. The encoder module is schematically shown in Fig. 6.3(a). In this module, commercial twisted-nematic liquid-crystal (LC) SLMs are used. The bit plane to be transmitted and the OOSP are displayed in 20 × 20 mm squares on SLM1 and SLM2, respectively. The collimated beam from the Xe lamp which has an intensity of 10 mW/cm^2 is intensity-modulated by passing through the SLMs. The average value of the contrast ratio between ON and OFF was measured to be approximately 50:1. The bit plane on SLM1 is imaged to OOSP on SLM2. A telescopic lens system was employed to suppress vignetting loss in off-center areas. The encoded parallel optical signals are multiplexed, demagnified, and imaged on the input end of an image fiber. The decoder module is shown in Fig. 6.3(b). The magnified signal from output end of the image fiber is imaged onto SLM3, and the correlation with the OOSP addressed on SLM3 is carried out. The correlated output from SLM3 is demagnified and imaged on a CCD device and the image data are loaded into video memory in a desktop computer. The surface-integral and thresholding operations are performed on this video memory at the video rate (30 frame/s). All the modules and the magnifier/demagnifier lens systems were packaged in cylinders, and, consequently, stray light was shut out. The aberration was small enough because the lens systems were specially designed for the system. The four encoder modules are used as shown in Fig. 6.4.

Silica-based test image fibers were fabricated. The fabrication process is as follows. A preform

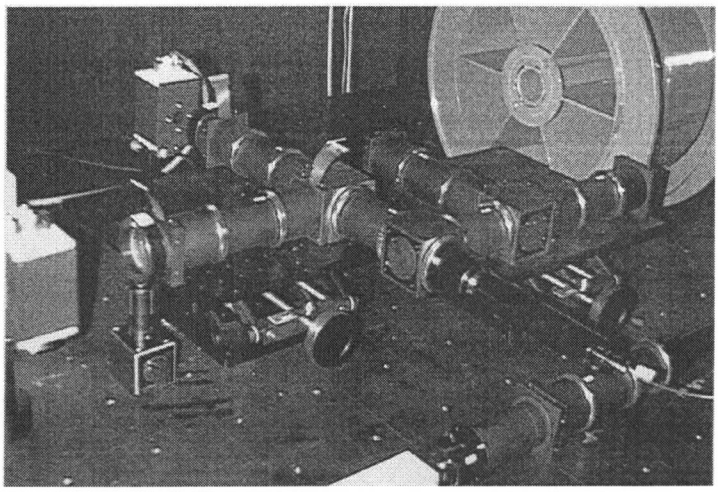

Fig. 6.4: Optical spatial encoder modules.

Table 6.1: Specifications of the test image fiber for four- channel, 8 × 8 bit, 2-D parallel transmission experiment

Parameter	Specification
Length	9 m
Number of pixels	30,000
Fiber diameter	850 μm
Picture diameter	790 μm
Minimum bending radius	80 mm
Numerical aperture	0.4
Spacing between pixels	4.4 μm
Core diameter	2.6 μm
Core material	GeO_2-SiO_2
Cladding material	F-SiO_2

rod has a number of core fiber rods that are aligned in a silica tube. The preform is heated and drawn into an image fiber. This fabrication method is more suitable for manufacturing long image fibers compared with that of the conventional multi-component image fibers. several image fibers up to 100-m in lengths have been fabricated.

6.2.3 Four-channel, 8 × 8 bit, 2-D parallel transmission experiment

This subsection shows experimental demonstration of four-channel multiplexing of 64-bit (8 × 8) 2-D paralel transmission based on space-CDMA. A 9-m-long image fiber was used in this experiment. In Table 6.1, the specifications of the test image fiber are summarized. It has 3×10^4 cores. The measured contrast value was larger than 0.4 for spatial frequency of less than 40 lp/mm.

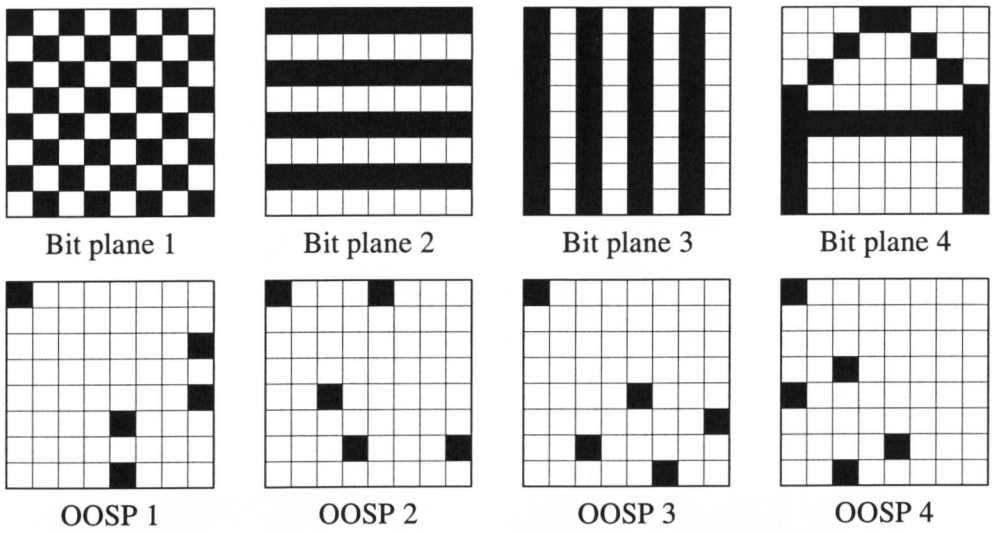

Fig. 6.5: Prepared bit planes and OOSPs.

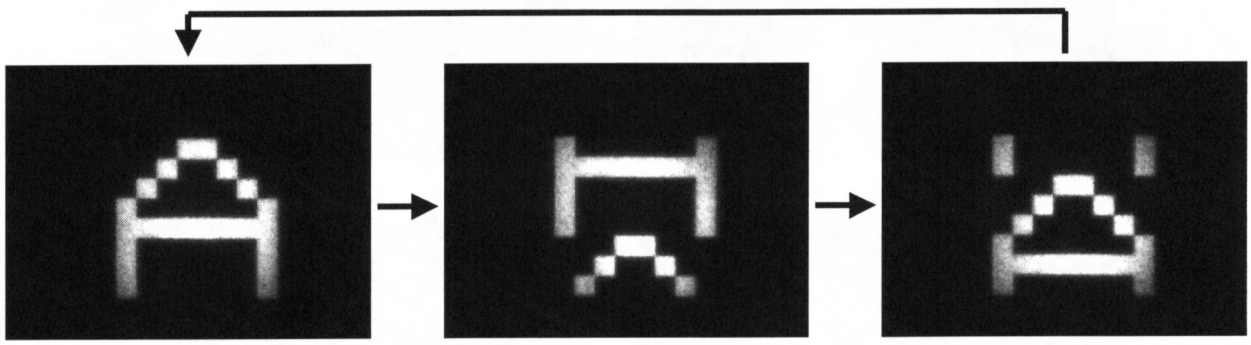

Fig. 6.6: Bit plane 4 before the encoding process.

Four 8 × 8 bit-planes and the 8 × 8 OOSPs used in the experiment are shown in Fig. 6.5. In these bit-planes, only Bit plane 4 is transmitted at the video-rate in which the character "A" moves upward as shown in Fig. 6.6. Each pixel of these Bit planes 1, 2, 3, and 4 is encoded by OOSPs 1, 2, 3, and 4, respectively. The multiplexed and transmitted image is shown in Fig. 6.7. It should be noted that these four bit planes are multiplexed with some vertical and horizontal shifts of 10 to 30 μm. It was experimentally confirmed that this misalignment does not affect receivers in decoding process even if the spatial shifts are larger because of the orthogonality of OOSPs.

Each receiver can recover the intended bit plane by correlating the received signal with the OOSP counterpart, followed by the thresholding process to cut off interference noise. The images decoded with OOSPs 1, 2, 3, and 4 are shown in Figs. 6.8(a), (b), (c), and (d), respectively. For example, Table 6.2 shows the values of the decoded Bit plane 2 without the normalization described below. The values in boldface correspond to 1, and the values in lightface represent 0. Each value of

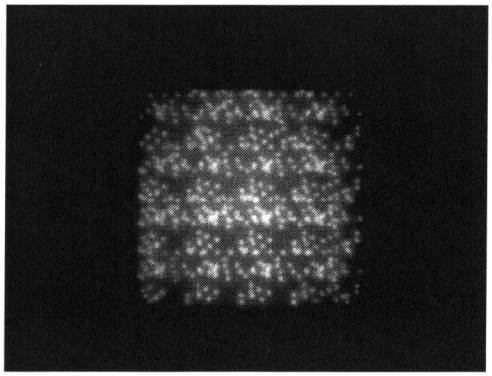

Fig. 6.7: Encoded and multiplexed bit planes after propagation through an image fiber.

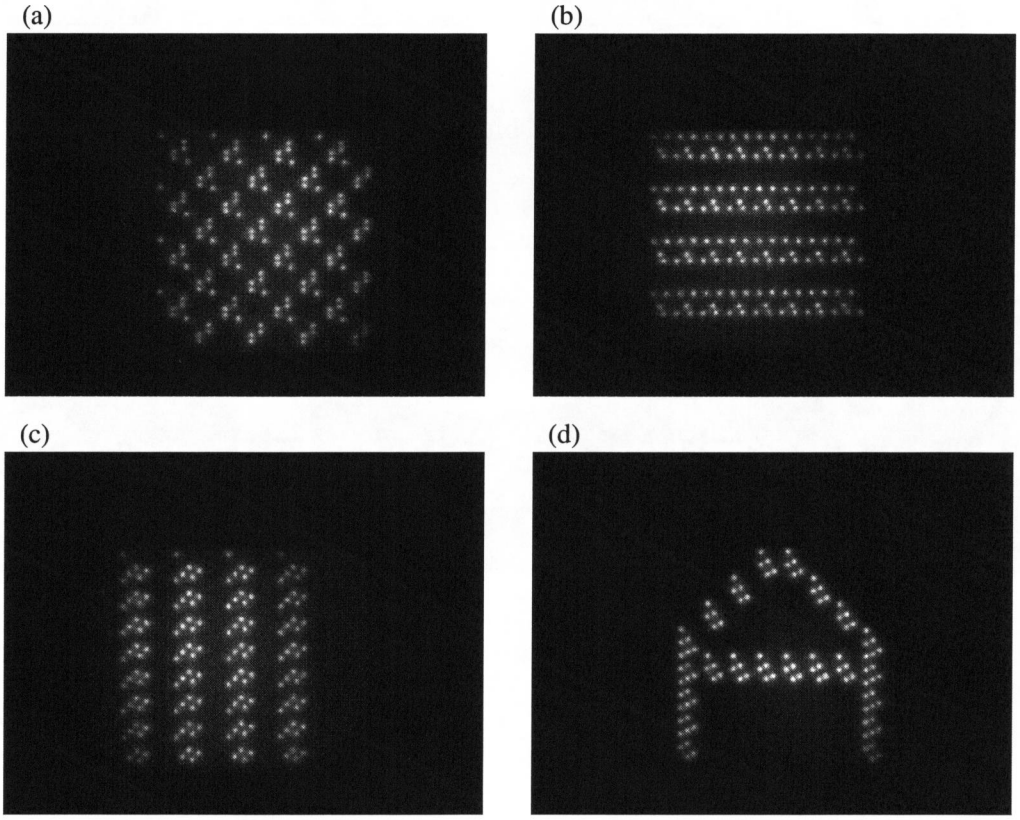

Fig. 6.8: Image after the correlation process with (a) OOSP 1, (b) OOSP 2, (c) OOSP 3, and (d) OOSP 4.

Table 6.2: Bit plane 2 decoded with OOSP 2 without normalization[a]

Two-dimensional intensity distribution on Bit plane 2							
0.12	**0.17**	**0.28**	**0.33**	**0.33**	**0.21**	**0.16**	**0.07**
0.11	0.22	0.34	0.43	0.37	0.26	0.11	0.50
0.23	**0.40**	**0.64**	**0.76**	**0.74**	**0.50**	**0.29**	**0.12**
0.17	0.36	0.63	0.83	0.72	0.45	0.19	0.09
0.28	**0.46**	**0.81**	**1.00**	**0.93**	**0.60**	**0.34**	**0.15**
0.16	0.31	0.50	0.68	0.59	0.39	0.18	0.10
0.19	**0.32**	**0.50**	**0.57**	**0.58**	**0.41**	**0.25**	**0.12**
0.07	0.14	0.21	0.27	0.24	0.18	0.09	0.06

[a]The entries in boldface correspond to values for 1; the entries in lightface correspond to values for 0.

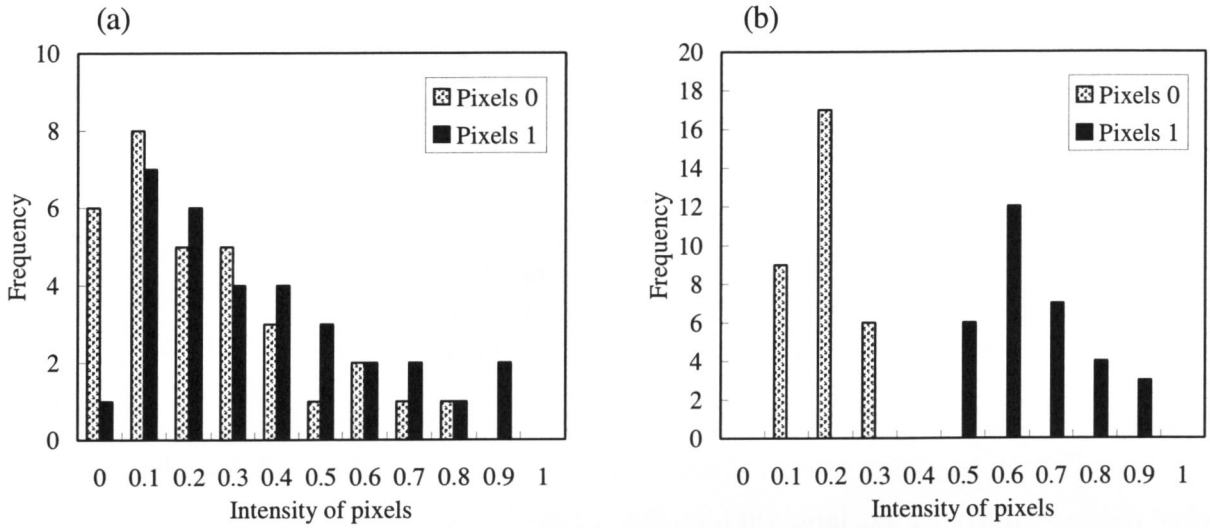

Fig. 6.9: Intensity distribution of bit plane 2 decoded with OOSP 2 (a) without and (b) with normalization.

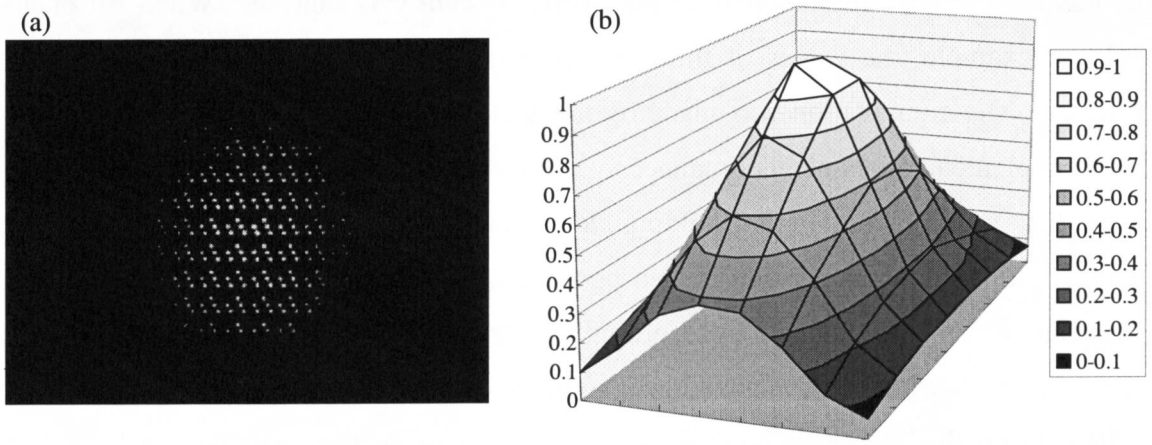

Fig. 6.10: Intensity distribution of bit plane 2 decoded with OOSP 2 (a) without and (b) with normalization.

these bit planes is obtained by the surface integral of the pixel values. The minimum value of 1 must be larger than the maximum value of 0 to be properly decoded by thresholding. However, the minimum value of 1 which is 0.07 is not larger than the maximum value of 0 which is 0.83 in Table 6.2. Any thresholding level can not be set without errors. The intensity distribution of the pixels 0 and 1 are shown in a histogram of Fig. 6.9(a). From this figure, it is also clear that it is impossible to distinguish the pixels 1 from 0.

The error will be presumably due to the 2-D nonuniformity of transmission characteristics. A uniform plain pattern (all pixels are 1) is encoded by OOSP 2 and transmitted. The pattern and its intensity distribution after the transmission through the image fiber are shown in Figs. 6.10(a) and (b), respectively. While the 2-D intensity distribution before the transmission is flat enough, that

Table 6.3: Bit plane 2 decoded with OOSP 2 with normalization[a]

Two-dimensional intensity distribution on Bit plane 2							
1.00	**0.65**	**0.79**	**0.65**	**0.71**	**0.59**	**0.83**	**0.59**
0.21	0.34	0.27	0.26	0.23	0.30	0.20	0.20
0.82	**0.68**	**0.71**	**0.58**	**0.64**	**0.61**	**0.79**	**0.59**
0.28	0.25	0.15	0.24	0.18	0.26	0.23	0.30
0.93	**0.68**	**0.77**	**0.66**	**0.74**	**0.65**	**0.81**	**0.69**
0.32	0.33	0.18	0.26	0.20	0.25	0.22	0.39
0.93	**0.63**	**0.67**	**0.56**	**0.70**	**0.59**	**0.81**	**0.74**
0.26	0.20	0.15	0.22	0.12	0.22	0.18	0.39

[a]The entries in boldface correspond to values for 1; the entries in lightface correspond to values for 0.

after the transmission decreases toward the off-center area. This is due to the transfer function of the image fiber and the objective lenses at both ends of the image fiber.

To compensate the nonuniformity of the intensity, a normalization was made in which the pixel values of the correlated output in the decoder was normalized by the values of the plain pattern so that the nonuniformity of the intensity of the overall system was canceled. When Bit plane 2 was decoded, for example, the values of the intensity distribution in Fig. 6.10(b) were used for the compensation. The computation was made by the desktop computer in this experiment, however, this can be implemented in a parallel manner by using a thresholding processor array, in which each processor has an individual thresholding level and operates in parallel. Simple optical implementation of the compensation is also possible by putting a filter after the SLM3, which is more transparent at the off-center area according to the two dimensional curve in Fig. 6.10(b). Table 6.3 shows the result with the normalization. The histogram of the intensity distribution is shown in Fig. 6.9(b). From this figure, it is apparent that the error-free transmission can be achieved by setting the thresholding level to 0.4.

6.2.4 100-long transmission experiment

This subsection describes experimental demonstration of a record distance (100 m) image fiber transmission of four-channel multiplexed 2-D signals. The distance is a giant leap from previous experiments with several m-long image fibers and facilitates the application to future 2-D optical interconnects. A test 100-m-long image fiber was prepared for this experiment. This image fiber has 3×10^4 cores, and picture diameter is 800 μm. The core diameter and the spacing between the cores are 3.0 μm and 4.4 μm, respectively. Four 2 × 2 bit planes and the 8 × 8 OOSPs used in the experiment are shown in Fig. 6.11. Bit planes 1, 2, 3, and 4 are encoded by OOSPs 1, 2, 3, and 4, respectively, as shown in Fig. 6.11. The multiplexed bit plane after 100-m-long propagation is shown in Fig. 6.12. The receiver recovered the intended bit plane by correlating the received signal

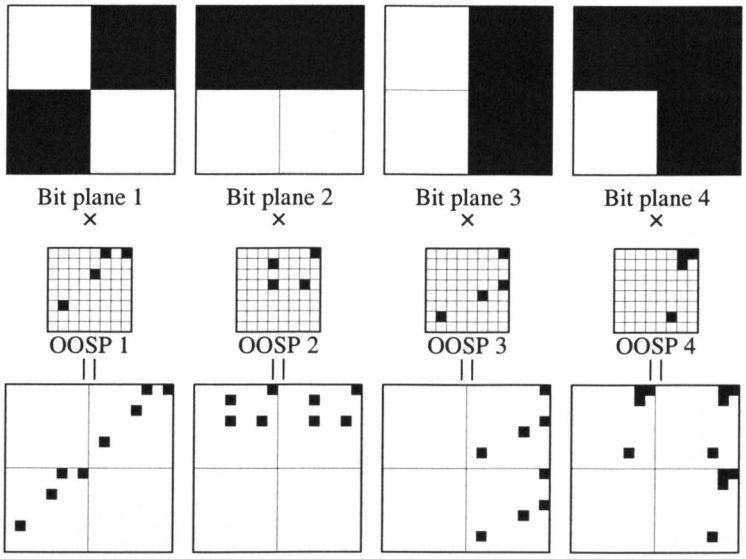

Fig. 6.11: Prepared bit planes and OOSPs for 100-m-long transmission experiment.

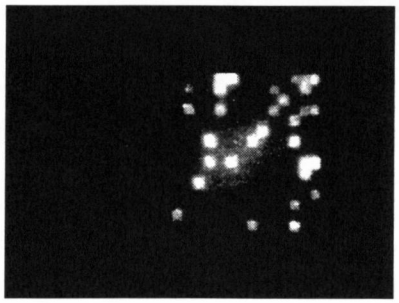

Fig. 6.12: Encoded and multiplexed bit planes after propagation through image fiber.

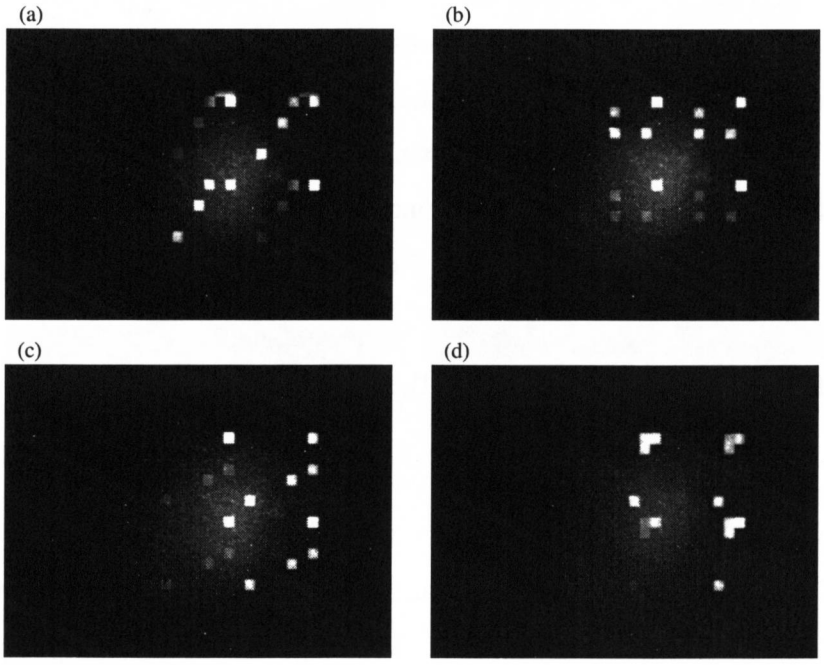

Fig. 6.13: Images after correlation process with OOSPs. (a) Correlated with OOSP 1. (b) Correlated with OOSP 2. (c) Correlated with OOSP 3. (d) Correlated with OOSP 4.

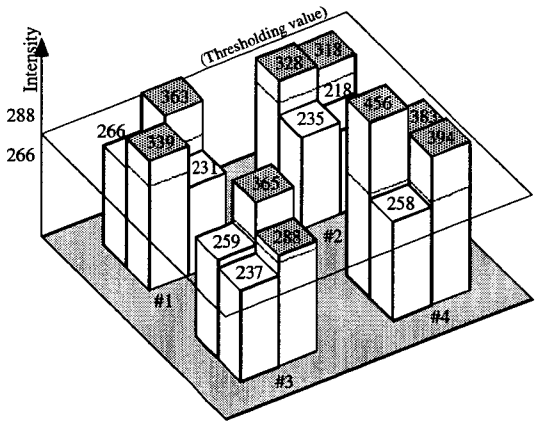

Fig. 6.14: Intensity distribution of pixels after correlation process.

Table 6.4: Specifications of the test image fiber for prethresholding experiment

Parameter	Specification
Length	2.6 m
Number of pixels	100,000
Fiber diameter	3200 μm
Picture diameter	3000 μm
Minimum bending radius	500 mm
Numerical aperture	0.2
Spacing between pixels	9 μm
Core diameter	6.8 μm
Core material	GeO_2-SiO_2
Cladding material	F-SiO_2

with the OOSP counterpart, followed by the thresholding process to cut off the interference noise. The images correlated with OOSPs 1, 2, 3, and 4 are shown in Figs. 6.13(a), (b), (c), and (d), respectively. Each value of bit planes was obtained by the surface integral of the pixel values as shown in Fig. 6.14. The shaded values correspond to the value 1. All the bit planes were correctly recovered by setting the threshold between 266 and 288.

6.2.5 Experiment of prethresholding method

The efficiency of the prethresholding method, which was theoretically investigated in Section 2.5, was experimentally verified. The experimental setup was based on the optical implementation shown in Fig. 6.2. A 2.6-m-long image fiber which has 10^5 cores was used in this experiment. The specifications of the image fiber are summarized in Table 6.4. Four input Bit planes 1 to 4 in Fig. 6.15 were encoded with the four OOSPs 1 to 4 in Fig 2.2(a), respectively. The multiplexed encoded bit plane after propagation through an image fiber is shown in Fig. 6.16. In this experiment, the

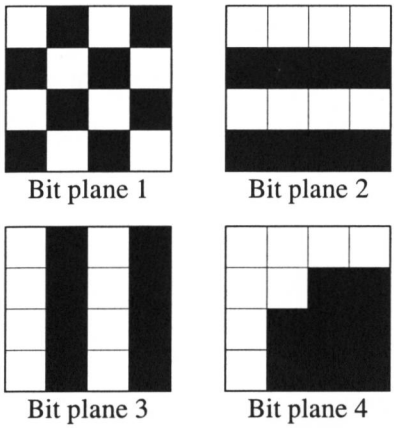

Fig. 6.15: Bit planes to be multiplexed.

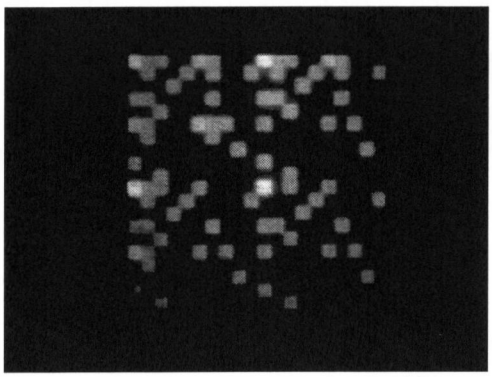

Fig. 6.16: Encoded and multiplexed bit planes after propagation through and image fiber.

(a)

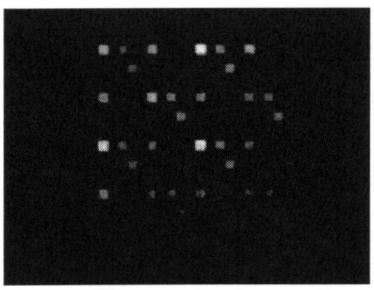

(b)

0.421	0.341	1	0.390
0.123	0.034	0.225	0.029
0.121	0.033	0.242	0.025
0.256	0.439	0.209	0.168
0.034	0.236	0.035	0.162
0.028	0.202	0.031	0.173
0.715	0.169	0.841	0.140
0.130	0.032	0.198	0.028
0.124	0.034	0.171	0.032
0.210	0.108	0.118	0.097
0.032	0.110	0.033	0.095
0.027	0.094	0.030	0.075

(c)

1	1	1	1
1	0	1	0
1	0	1	0
1	1	1	1
0	1	0	1
0	1	0	1
1	1	1	1
1	0	1	0
1	0	1	0
1	1	1	1
0	1	0	1
0	1	0	1

Fig. 6.17: (a) Correlation output with OOSP 1. (b) Normalized intensity of the correlation output. (c) Prethresholded result.

prepared multiplexed pattern was displayed on one encoder because of the lack of four encoders. The decoded output correlated with OOSP 1 and its normalized intensity distribution are shown in Figs. 6.17(a) and (b), respectively. In Fig. 6.17(b), each pixel in 4 × 4 matrix has three bright spots which correspond to the three chip pixels in a OOSP 1 shown in Fig. 6.17(a). The shaded values

correspond to a level of intensity of 0, and the others correspond to other intensity levels (1–4). Figure 6.17(c) is the result of the prethresholding that can be achieved when the prethresholding level Th' is set to $0.036 < Th' < 0.094$. It is clear from Fig. 6.17(c), that the input bit plane can be regenerated correctly when the thresholding level is set to $1 < Th < 3$.

6.2.6 Discussions

One of the most important factors which decide the system performance is the spatial resolution of the system. The length of parallel data format in a channel, that is, the size of bit planes and the size of OOSPs are restricted by the resolution. Additionally, as the size of OOSP is increased, the number of OOSPs can be increased. The spatial resolution of the system is especially decided by the resolution of image fibers. The image fiber used in the experiment of Subsection 6.2.3 has a picture diameter of D = 0.79 mm. The diameter can be increased to as large as 3 mm. However, the minimum bending radius also increases to about 0.5 m and the yield degrades because of an increase in the number of broken pixels in a large image circle at the same time. The picture diameter is limited by physical constraints due to the minimum bending radius and the yield. When image fibers are used for parallel transmission, generally the 2-D signal patterns are arranged so as to be inscribed in the image circle. If the picture diameter increases to 3 mm, a diameter 3.8 (3/0.79) times as large as the current image fiber is achievable.

Taking into account the fact that the parallel data format in latest central processing units is 32 bit or 64 bit, the data format of 64 bit (8 × 8) in this experiment is enough for interconnecting processors and other devices. If the same 8 × 8 data format is used with the image fiber described above, OOSPs as large as (30 × 30) are available. The possible number of OOSPs N for $\lambda_a = 1$ is bounded by [11]

$$N \le \frac{M^2 - 1}{w(w-1)}. \tag{6.4}$$

For example, if M = 30 and w = 12, we can construct only less than six OOSPs.

2-D CDMA has many similar characteristics to those of conventional time-domain CDMA [32]-[35]. The OOSPs in 2-D CDMA can also be regarded as an extension of the code which is used in the time-domain CDMA, or so-called optical orthogonal codes (OOCs) [36]. In the early stage of the study, OOCs were investigated with the autocorrelation constraint $\lambda_a = 1$ [37]. It has been reported, however, that the number of OOCs can be increased by relaxing the autocorrelation constraint to $\lambda_a > 1$ [55]. Actually, we used the OOSPs with $\lambda_a = 4$ to construct enough OOSPs

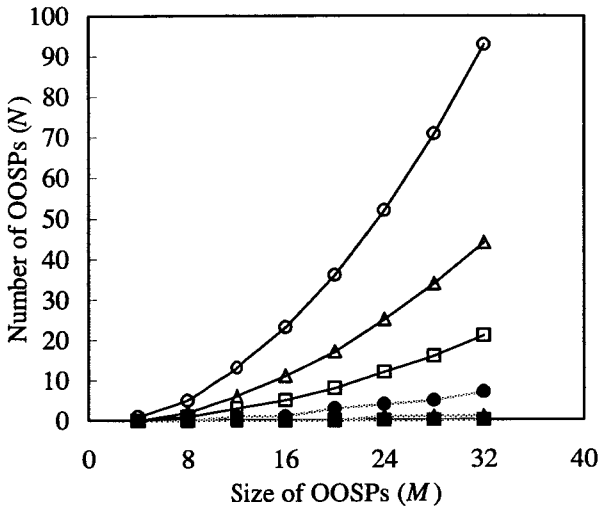

Fig. 6.18: Upper bound on the number of OOSPs N that can be constructed with a size of M.

in this experiment. Recently, an upper bound for the OOSPs with $\lambda_a > 1$ was reported by Yang and Kwong [38]. According to their paper, the number of OOSPs is bounded by

$$N \le \frac{(M^2-1)\lambda_a}{w(w-1)}. \tag{6.5}$$

λ_a has to be, however, smaller than or equal to w. Figure 6.18 shows the comparison of the two upper bounds Eqs. (6.4) and (6.5) versus the size of OOSPs for different values of the weight w. This figure shows that much more OOSPs can be constructed by relaxing the autocorrelation constraint λ_a to be larger than unity. To increase the transmission capacity of the space-CDMA system, improving the design of OOSPs is as important as improving the spatial resolution of the system.

In the experiments in this section, slow LC-type SLMs and Xe lamps for addressing the data bit planes and a CCD as a detector was used. These slow devices can, however, be replaced by 2-D VCSEL arrays and PD arrays. The proposed normalization described above can be achieved by setting the thresholding level properly in the processor arrays following the PD arrays. In the experiment above, the bit-plains were displayed in 20 × 20 mm squares on SLMs and had to be demagnified to be launched into the image fibers. The large vignetting loss shown in Fig. 6.10 was caused mainly by the demagnification. However, we can decrease this vignetting loss by using VCSEL arrays because the pitch size of VCSEL array is as small as 250 μm. If larger matrix size of VCSEL/PD arrays can be used, all SLMs and some imaging lenses can be removed by displaying OOSPs on VCSEL arrays directly, and, consequently, more simplified and cost-effective system

implementation can be achieved. However, we have to use some imaging lenses at both ends of the image fiber. In general, imaging lens system is hard to be miniaturized. One possibility is to introduce micro-optics using graded index (GRIN) rod lenses. Another important candidate is to use fiber optic plate (FOP) taper, which was proposed by Li et al [56]. In case of using this FOP taper, the vignetting loss does not occur and normalization in decoding process will not be needed. This construction using VCSEL/PD arrays will allow us to transmit at a frame rate at least up to several hundred mega-frames per second and even more. This high-speed space-CDMA system using 2-D VCSEL/PD arrays will be described in next section.

6.3 High-speed space-CDMA system using 2-D VCSEL/PD arrays

6.3.1 Optical implementation

Figure 6.19 shows schematically space-CDMA system implementation by use of 2-D VCSEL/PD arrays. A transmitter consists of a 2-D VCSEL array and a SLM. In the transmitter, an OOSP is addressed electrically on the SLM. Reading out the SLM with 2-D optical data from the VCSEL array allows the optical encoding in parallel. The encoded optical signals are transmitted by an image fiber in parallel and multiplexed by an image-fiber coupler [19]. A receiver consists of a SLM, a 2-D PD array , and a thresholding circuit array. The correlations of the received multipexed optical signals and an OOSP is performed on a SLM, and the correlated optical signals are detected

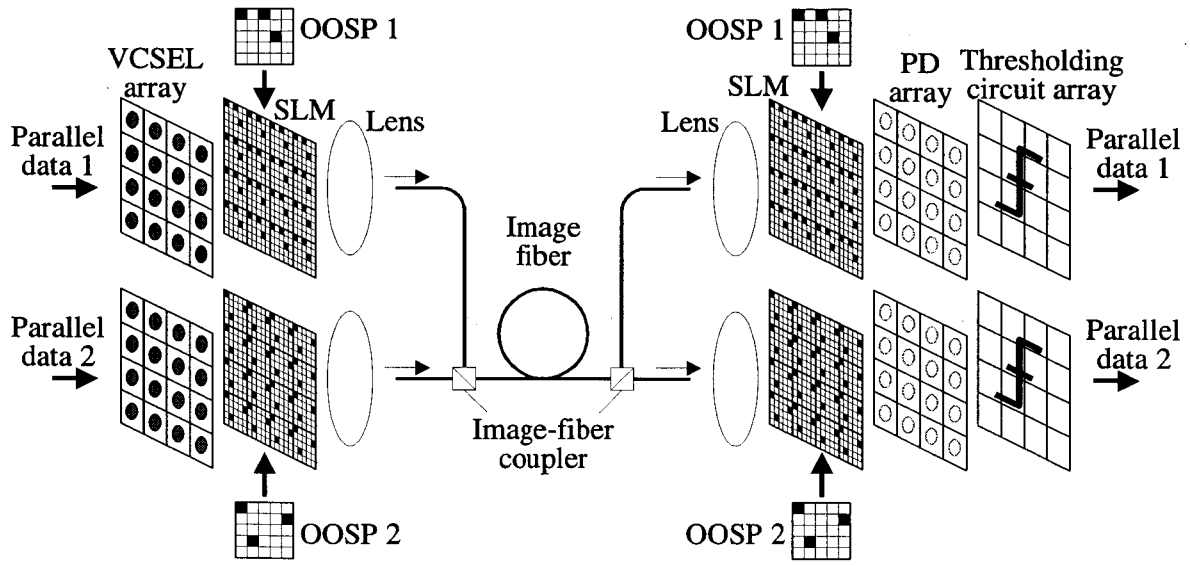

Fig. 6.19: Space-CDMA system implementation by use of VCSEL/PD arrays.

by the PD array. The intended parallel data are regenerated after a thresholding operation on the correlation output.

Space-CDMA system can also be implemented by more simplified and cost-effective construction. In such a way, that encoded parallel signals are generated by electronic encoders and displayed directly on VCSEL arrays. Encoded and multiplexed optical signals are directly detected by PD arrays, and both correlation and thresholding processes are performed electronically. The electronic encoders and decoders can simply be constructed by fan-in/fan-out circuits and switches which pick out the lines of chip pixels of addressed OOSPs. This implementation needs large matrix size of 2-D VCSEL/PD arrays, which is decided by the product of the array size of 2-D data and OOSPs. However, supposing that we can use processor array chips [1], the electronic encoder/decoder do not restrict the throughput of the system because of the simple construction. In the experiment of this section, this simple implementation is employed.

6.3.2 Transmitter/receiver modules and its performance

In this section, transmitter and receiver modules and its perfomance is described. The setup of the modules in a construction of 1-to-1 optical link is shown in schematic form in Fig. 6.20. Specifications of each component are as follows. The elements of the 8 × 8 VCSEL array have an 850-nm wavelength and are arranged at a pitch of 250 μm [57]. Each detector in the 8 × 8 PD array has a of 58 μm diameter and the detectors are arranged at a pitch of 250 μm. Number of cores, picture diameter, and spacing between cores for the image fiber are 5×10^{-4}, 1020 μm, and 4.4 μm, respectively. Length of the image fiber is 1 m. Magnification ratio of the imaging lenses is 0.3. The lens system consisting of three GRIN rod lenses and a beam splitter (BS) is used for optical alignment, which has the same construction as an image fiber coupler described in Chapter 4. Since

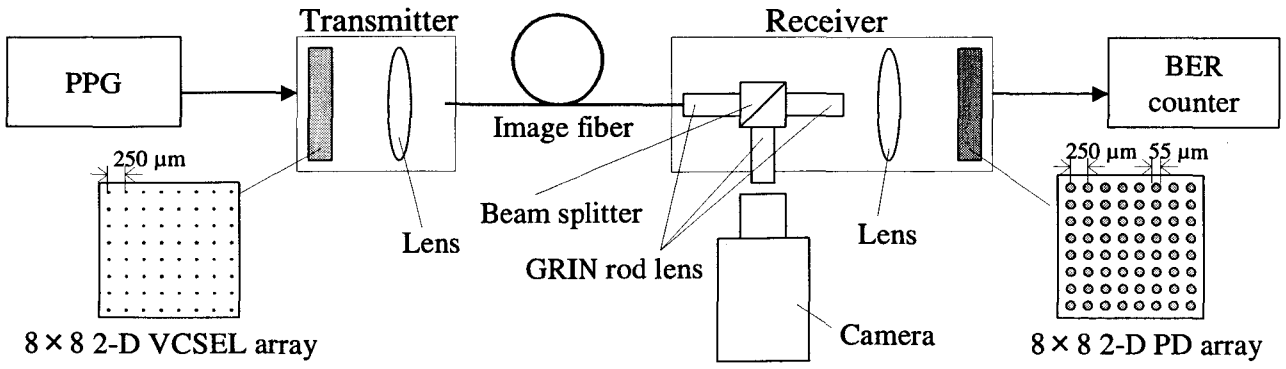

Fig. 6.20: Experimental setup of 2-D parallel optical interconnect using an image fiber and 2-D VCSEL/PD arrays.

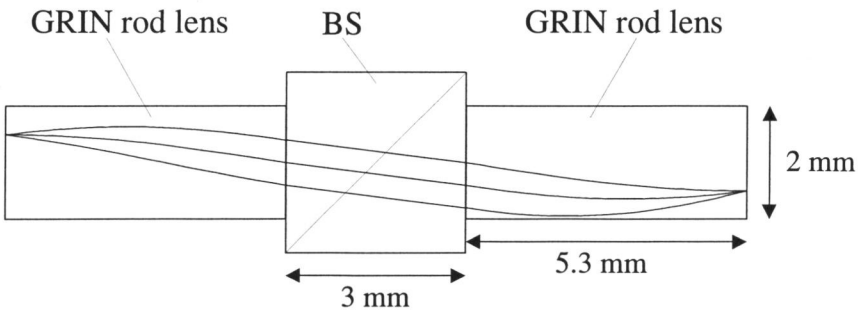

Fig. 6.21: Diagram of imaging system which consists of GRIN rod lenses and a BS.

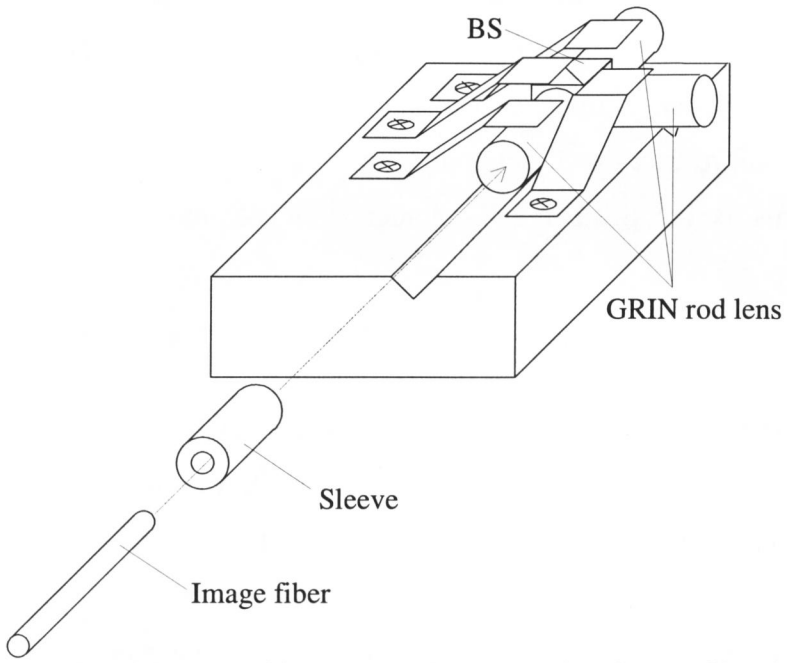

Fig. 6.22: Assembly of GRIN rod lenses, a cube BS, and an image fiber in the receiver.

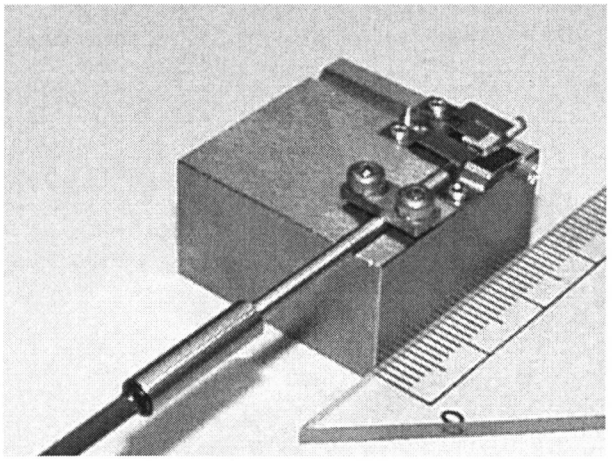

Fig. 6.23: Photograph showing the lens system in the receiver with an image fiber.

optical signals and the PD array can be observed by camera via the BS, optical alignment can be achieved visually. Figure 6.21 is a schematic diagram of the lens system. The size of each component is also shown in the figure. The focal points of the lens system are on the end surfaces

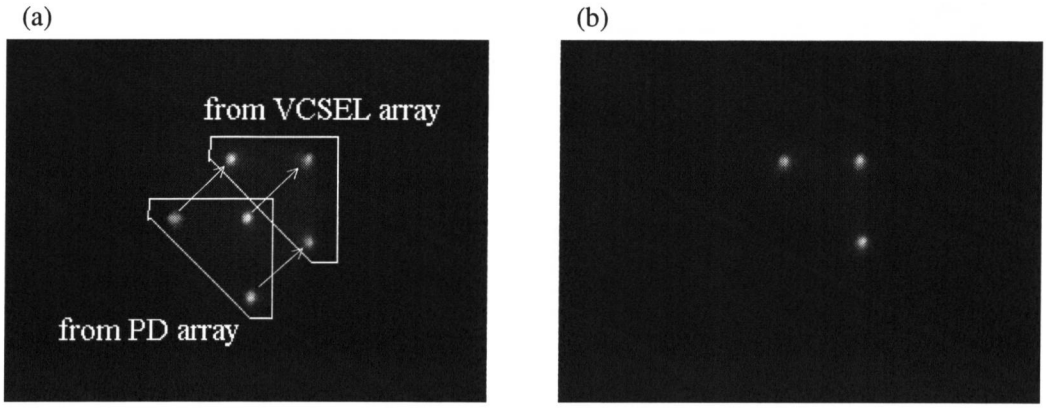

Fig. 6.24: Process of visually aligning VCSEL and PD arrays. Before (a) and after (b) optical alignment.

of the GRIN rod lenses. The lenses, beam splitter, and the receiver end of the image fiber are passively fixed on V-grooves as shown in Fig. 6.22. The image fiber is inserted in a sleeve so that its optical axis can be aligned with that of the GRIN rod lenses. The BS is sandwiched between the GRIN rod lenses. A photograph of the lens system in the receiver is shown in Fig. 6.23.

Optical alignment is achieved as follows. The VCSEL array and the lens of the transmitter are optically aligned by directly connecting a camera to the output end of the image fiber and visually monitoring the output image. After aligning the transmitter, the output end of the image fiber is butt-jointed to a GRIN rod lens on a V-groove, because the focal points of the GRIN rod lens are on its end surfaces. The PD array and the lens in the receiver are optically aligned by using camera to simultaneously monitor the VCSEL and PD arrays. Optical signals that propagate through the image fiber are reflected by the PD array and observed by the camera. By injecting a forward current into the PD array, it operates as an array of LEDs. Therefore, an image that results from the superimposing of incident optical signals from the VCSEL array and light emitted from the PD array can be viewed through the BS by using the camera. The PD array and the lens are so adjusted that each optical signals falls on its corresponding target, as shown in Fig. 6.24. We confirmed that each component was aligned at its optimum position by using the method of alignment described above. It should be noted that the structure and alignment method are so simple that cost-effective optical interconnection modules are possible to be realized.

To evaluate the performance of the modules, transmission experiments was made without multiplexing using space-CDMA. In the experiment, only four (2 × 2) neighboring channels were modulated for simplicity in the evaluation of crosstalk between neighboring channels. Figure 6.25 shows the intensity profile for two neighboring optical signals on the output end-surface of the image fiber. The spacing between the optical signals in the image fiber was 75 μm because the

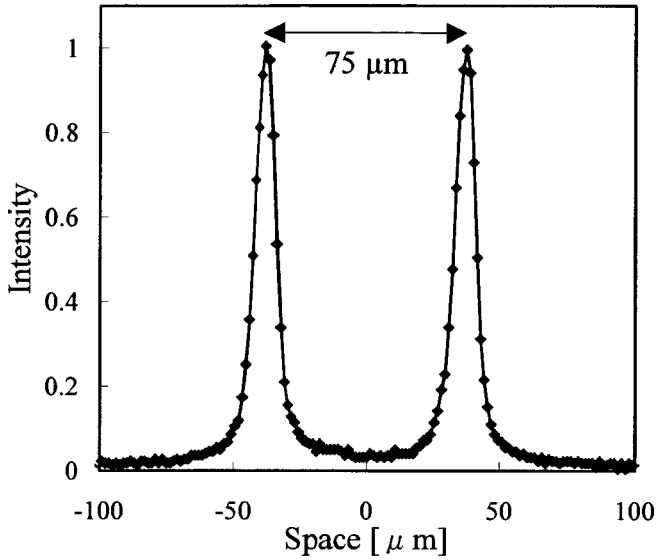

Fig. 6.25: Intensity profile of two neighboring optical signals on the output end-surface of the image fiber.

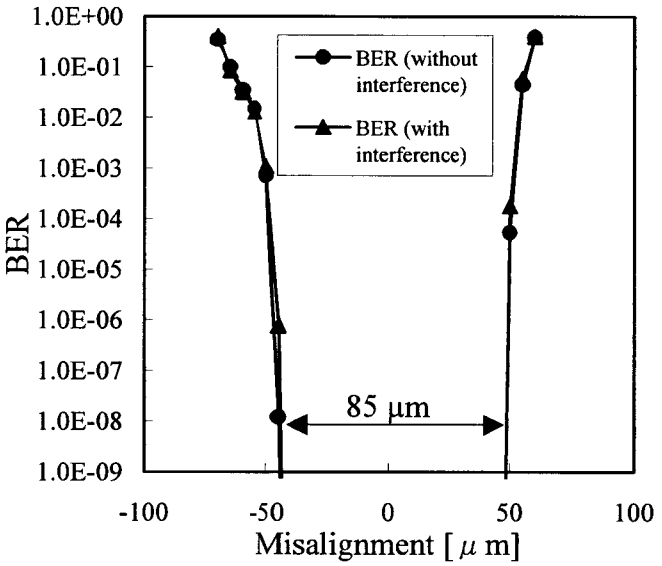

Fig. 6.26: BER performance against spatial shifts in the position of the PD array for transmission with and without interference.

optical signals from the VCSEL array of 250 μm in pitch was imaged with the magnification ratio of 0.3 on the input end of the image fiber. Crosstalk from an adjacent channel was at –34 dB, and this was measured by monitoring the output current of neighboring PDs. We used a nonreturn-to-zero (NRZ) 2^9-1 pseudorandom binary sequence (PRBS) 15 Mb/s signal to modulate one of the VCSELs and modulated the other three VCSELs by using the inverse of the signal. The BER was less than 10^{-9} when the average output power of each VCSEL was 1 mW.

Next, we shifted the PD array from its optimum position, in the direction of the line between

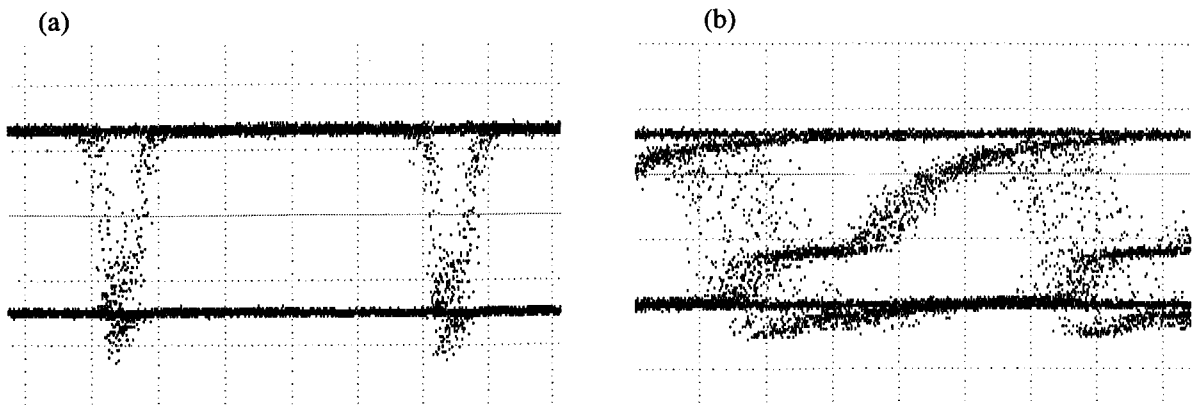

Fig. 6.27: Eye patterns when a serial data stream was transmitted without encoder/decoder. ((a) 100 Mbps/ch, PRBS 2^{11}-1 and (b) 1 Gbps/ch, PRBS 2^{23}-1)

neighboring PDs. The measured result is shown in Fig. 6.26. The BER when only a single VCSEL was modulated (all other channels were OFF) is also plotted for reference. From the result, tolerance to misalignment for a BER of 10^{-9} was 85 μm. Larger tolerance can be made possible by defocusing the optical spots on the PD array and thus sacrificing coupling efficiency. It should be noted that no significant difference between the BERs for single channel and four-channel transmission was observed. Crosstalk from adjacent channels is thus sufficiently suppressed for effective parallel transmission.

Transmission experiment up to 1 Gbps/ch was also performed. Eye patterns of 100-Mbps/ch (PRBS 2^{11}-1) and 1-Gbps/ch (PRBS 2^{23}-1) data streams obtained after the transmission through the image fiber by using only one pixel of the VCSEL/PD arrays are shown in Figs. 6.27(a) and (b), respectively. The transmitter and receiver modules showed error-free transmission at a speed of up to 1 Gbps/ch (BER < 10^{-9}).

6.3.3 Experimental setup

The experimental setup of space-CDMA system is shown in Fig. 6.28. A couple of four-bit (2×2) parallel signals are generated by a pulse pattern generator (PPG) and a fan-out circuit. Each signal channel is encoded by a spatial encoder on which OOSPs are addressed. We used OOSPs with a code size of 4 × 4. Therefore, the total number of chip pixels is 64 (8 × 8). The 8 × 8 VCSEL arrays mounted on transmitter modules 1 and 2 are driven by the chip signals from the encoders. The length of each image fiber is 1 m.

The encoded optical signal patterns from the VCSEL arrays are transmitted through the image fibers. The optical signals from the output ends of the image fibers are multiplexed by an image

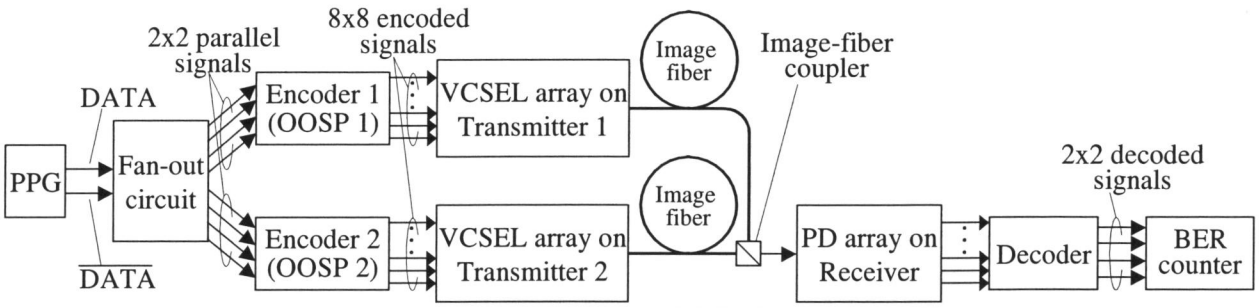

Fig. 6.28: Experimental setup of space-CDMA system using image fibers and VCSEL/PD arrays.

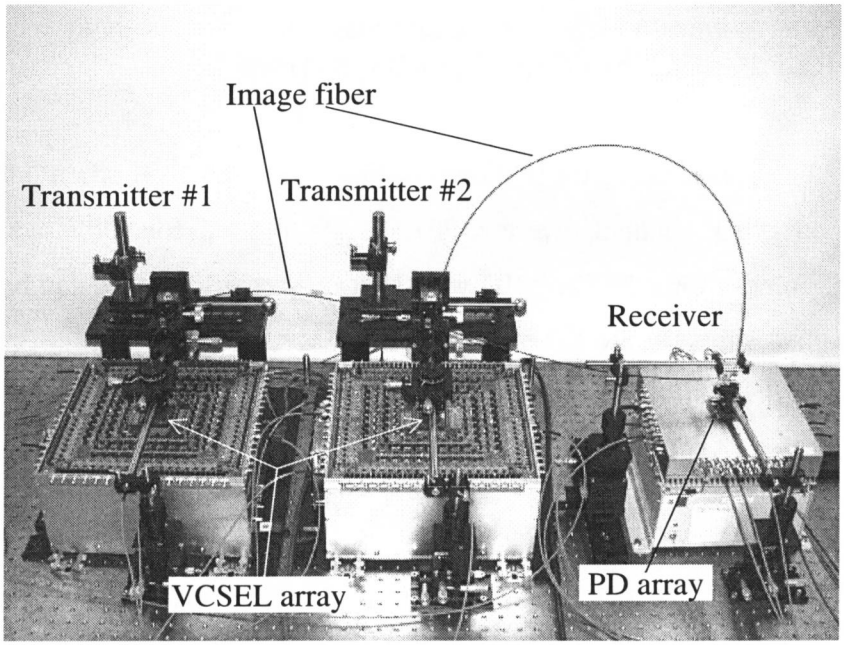

Fig. 6.29: A photograph showing two transmitters and a receiver with VCSEL/PD arrays for space-CDMA experiment.

fiber coupler which was described in Chapter 4. The multiplexed optical signals are detected by the 8 × 8 PD array. The decoder correlates, in parallel, all bits of the received signals and addressed OOSPs. After the correlation and thresholding operation in the decoder, the intended 2 × 2 signals are retrieved. Figure 6.29 shows a photograph of the two transmitters and the receiver connected by the image fibers.

6.3.4 Experimental results

The transmitter and receiver modules showed error-free transmission at a speed of up to 1 Gbps/ch as described above. However, the bandwidth of the prepared encoders and decoder was several tens of Mbps. Therefore, we performed space-CDMA transmission at a speed of 64

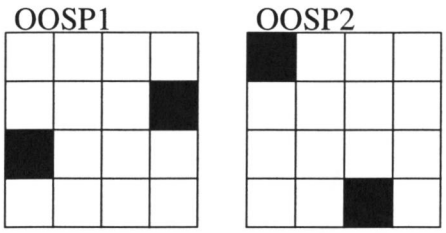

Fig. 6.30: Prepared OOSPs with code size of 4 × 4.

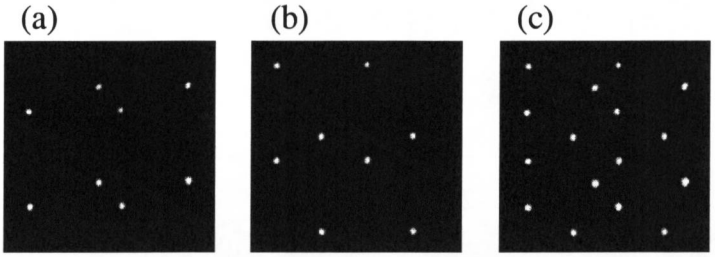

Fig. 6.31: 2 × 2 optical signals encoded by (a) OOSP 1 and (b) OOSP 2 after propagation through 1-m-long image fibers. (c) Encoded and multiplexed optical signals.

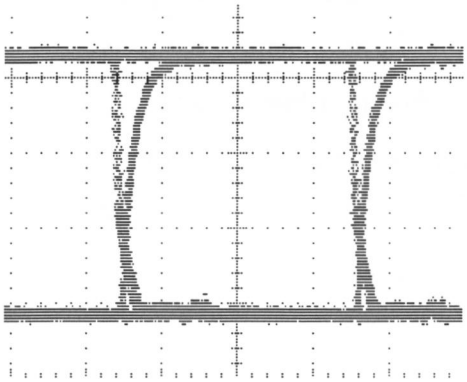

Fig. 6.32: Observed eye pattern of Ch-1 of transmitter #1.

Mbps/ch. Figure 6.30 shows the prepared OOSPs which are mutually orthogonal [11]. The code size and code weight are 4 × 4 and 2, respectively. Figures 6.31(a) and (b) show optical signals encoded by OOSP 1 and OOSP 2 after propagation through the image fibers. Each optical spot corresponds to a chip pixel of the OOSPs. The optical signals multiplexed by an image fiber coupler are shown in Fig. 6.31(c). The spot diameter was about 20 μm.

The data signal for one channel was NRZ 2^{11}-1 PRBS 64 Mbps and its inverted data were used for the other seven channels to observe the crosstalk effect. The eye pattern of an output signal of the decoder is shown in Fig. 6.32. The BER was less than 10^{-9} when the average output power of each VCSEL was 0.4 mW. Any influence of the crosstalk on the BER performance was not observed.

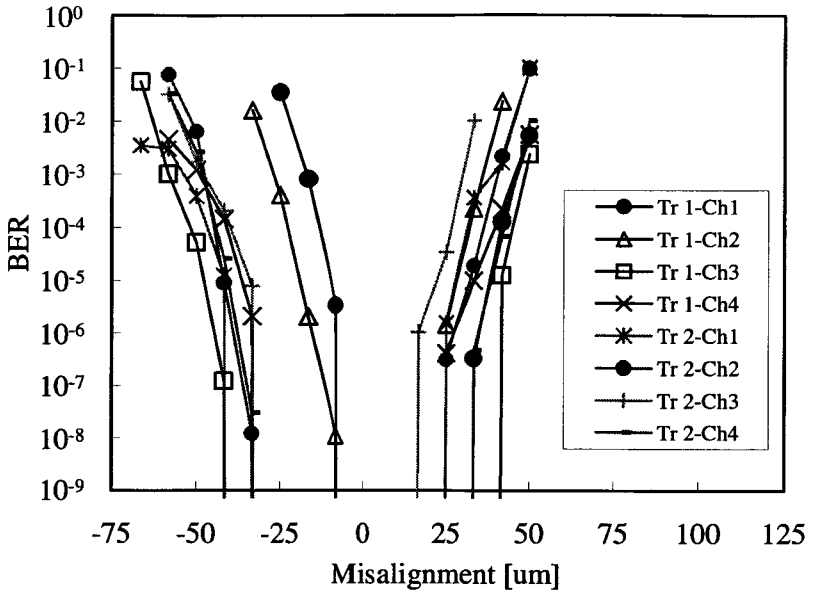

Fig. 6.33: BER performance versus lateral misalignment of PD array.

Next, we offset the PD array from its optimum position in the direction of the line linking neighboring PDs. The BER of eight channels (4 bits × 2 transmitters) versus this lateral misalignment of the PD array is shown in Fig. 6.33. The misalignment tolerance for a BER of 10^{-9} was 25 μm, which is large enough for the practical fabrication of interconnection modules.

6.4 Conclusion

In this chapter, several experimental demonstrations of image fiber optic 2-D parallel optical interconnects based on space-CDMA was described. Section 6.2 showed experiments of space-CDMA systems in which 2-D optical signals were generated by use of Xe lamps and SLMs. In the experiment, four channels of 64-bit (8 × 8) parallel optical signals were multiplexed and transmitted through an image fiber. Experimental demonstrations of transmission through a 100-m-long image fiber and decoding using prethresholding method were also described. In Section 6.3, high-speed space-CDMA system using 2-D VCSEL/PD arrays was described. In the experiment, 512-Mbps 2-D parallel transmission using 8 × 8 VCSEL/PD arrays was demonstrated. Two spatially encoded four-bit (2 × 2) parallel optical signals were emitted from the VCSEL arrays and transmitted through image fibers. After the multiplexing/demultiplexing operations, the two parallel signals are individually retrieved.

In the experiment using VCSEL/PD arrays, the total throughput was 512 Mbps (64 Mbps/ch × 8

ch). The transmission speed per channel was 64 Mbps/ch, which was limited only by the processing speed of electronic circuits of the encoders and decoder. However, the data bit rate can be further increased by employing high-speed logic circuits such as emitter-coupled logic (ECL). Furthermore, the number of parallel channels can be increased by using VCSEL/PD arrays with a larger array size. This improvement should increase the throughput to more than several tens of Gbps. The transmission distance in our experiment was limited by the length of the prepared image fibers. However, by using longer image fibers with improved crosstalk characteristics, we can achieve transmission distance of over 100 m [25].

Chapter 7

Conclusions

This thesis has investigated image fiber optic 2-D parallel optical interconnects based on space-CDMA.

In Chapter 1, the background of this thesis has been reviewed, and the outline of the thesis has been provided.

In Chapter 2, the interference noise of 2-D orthogonal code, namely, OOSPs which is used in space-CDMA scheme has been theoretically evaluated. Probability density function of the interference noise has been derived. Multiplexing characteristics of the space-CDMA system have been investigated from a aspect of bet errors caused by the interference noise. BER performance has been calculated in terms of the decision threshold, the code length, the code weight, and the number of users.

In Chapter 3, the transmission characteristics of image fibers has been investigated. At first, 2-D parallel optical transmission media including image fibers, 2-D fiber arrays, and lens systems were compared, and the advantages and drawbacks were studied. Image fiber skew characteristics has also been investigated. The time-of-flight difference between individual cores over the whole area of an image circle has been measured for the first time using a novel skew measurement method. It has also been shown that the skew of an image fiber increases by bending. The theoretical and experimental analysis have revealed that the bending-induced skew depends neither on the radius of curvature nor the shape of the curve but it depends only on the number of turns it is wound.

In Chapter 4, image-fiber branching device, namely, image fiber coupler has been proposed. This image fiber coupler has several features including compact and reliable assembly and ease of optical alignment. The image fiber coupler has been developed using GRIN rod lenses, a miniature cube BS, and V-grooves. Required lens parameter conditions such as NA, lens diameter, and size of BS have been clarified by theoretical analysis. Vignetting loss and contrast degradation characteristics has been experimentally investigated.

In Chapter 5, EDIFA-based 2-D optical amplifier and its pumping method have been proposed. Test EDIFAs were fabricated, and its gain characteristics were measured. The gain of a 3.0-m-long test EDIFA saturated at less than 1.2 dB. However, a reference single-mode, single-core fiber which had pulled from the same core preform as that for the EDIFA had a gain of over 20 dB. To achieve higher gain of EDIFA, it has been pointed out that: (i) dopant concentrations used to control viscosity need to be optimized to eliminate bubbles and to pull longer EDIFAs; and (ii) core parameters need to be designed so that the EDIFAs are single-mode at a 1.48 μm wavelength to increase pumping efficiency.

In Chapter 6, several experimental demonstrations of image fiber optic 2-D parallel optical interconnects based on space-CDMA have been presented. Four channels of 64-bit (8 × 8) parallel optical signals were multiplexed and transmitted through an 9-m-long image fiber using a experimental space-CDMA system in which Xe lamps and SLMs were used to generate 2-D optical signals. Transmission experiment through a 100-m-long image fiber has also been demonstrated, in which four-channel-multiplexed 4-bit (2 × 2) parallel signals have been transmitted. To achieve higher-speed transmission, a space-CDMA system using 2-D VCSEL/PD arrays has been constructed. Using the system, 512-Mbps 2-D parallel transmission has been demonstrated. Two spatially encoded four-bit (2 × 2) parallel optical signals have been emitted from the VCSEL arrays and transmitted through image fibers.

The interconnect systems considered in this thesis provide asynchronous multiple-access data links of 2-D optical signals for inter-chip to inter-cabinet interconnections and 2-D processor arrays systems. Space-CDMA allows 2-D optical signals to be transmitted and accessed simultaneously with no waiting time in an asynchronous manner. Image fiber has been used as a direct-image transmission medium conventionally. However, the investigations through this thesis indicated its usability as a 2-D optical data transmission medium. The theoretical evaluations and experimental demonstrations have revealed its performance to transmit 2-D optical signals at the transmission speed of 1 Gbps/ch. The transmission speed in the demonstrations was limited by electronic circuits. In the experimental demonstrations, 8 × 8 (64-bit) VCSEL/PD arrays were used. However, image fiber itself can accommodate over 10^3 optical channels because 5 × 10^4-cores image fiber used in the experiments uses only 2 % cores if one optical channel is transmitted by one core. The other 98 % cores are used to suppress crosstalk. Therefore, a total throughput of 1 Tbps will be possible using VCSEL/PD arrays with larger matrix size and higher speed electronic circuits.

Through this research, I have clarified the validity of the image fiber-optic 2-D parallel optical interconnects based on space-CDMA. I hope that this research will make great contributions toward the future high-throughput 2-D parallel interconnect systems.

Appendix

Appendix A

Derivation of Eq. (2.15)

In this Appendix, the upper bound for the interference signal I_1 in prethresholding scheme is derived. As shown in Fig. 2.7(c), the interference signal on the first user I_1 takes on integer value 0 to w. We can express these interfering chip pixel position as $p1, p2, \ldots, pw$. When $I_1 = 0$ ($pi = 0$ for all i), the probability $\Pr(I_1 = 0)$ can be expressed as

$$\Pr(I_1 = 0) = {}_wC_0 \left(1 - \frac{w^2}{2M^2}\right)^{N-1}. \tag{A.1}$$

When $I_1 = 1$, there are ${}_wC_1$ ways of interfering chip position. If the position of hit is at $p1$ ($p1 = 1, pi = 0$ for $2 \le i \le w$), the probability of the hit $\Pr(p1 = 1)$ can be expressed as

$$\Pr(p1 = 1) = 1 - q_c^{N-1}, \tag{A.2}$$

where q_c is the probability that one OOSP does not overlap a specific chip position. This can be written as

$$q_c = 1 - \frac{w}{2M^2}. \tag{A.3}$$

The probability that there is no overlap on the other chip positions, i.e., $\Pr(pi = 0)$ for $2 \le i \le w$, is due to the number of OOSPs which overlap on $p1$. For example, if all N - 1 interfering OOSPs overlap on $p1$, there are no overlaps on the other chip position, i.e., $\Pr(pi = 0)=1$ for $2 \le i \le w$.

However, if the number of overlaps on $p1$ is smaller than N - 1, the probability Pr(pi = 0) is smaller than one. Therefore, the probability of I_1 = 1 can be expressed as

$$\Pr(I_1 = 1) \leq {}_wC_1\left(1 - q_c^{N-1}\right). \tag{A.4}$$

When I_1 = 2, there are ${}_wC_2$ ways of interfering chip position. The probability of hit on the first chip position $p1$ is $1 - q_c^{N-1}$. The probability of hit on the second chip position $p2$ is due to the number of overlaps on $p1$. If the number of overlaps on $p1$ is one, the probability of hit on $p2$ is $1 - q_c^{N-2}$, and if the number of overlaps on $p1$ is two, the probability is $1 - q_c^{N-3}$. Hence $1 - q_c^{N-2}$ in maximum. The probability of no hits on the other chip position can be up to one as described above. Therefore,

$$\Pr(I_1 = 2) \leq {}_wC_2\left(1 - q_c^{N-1}\right)\left(1 - q_c^{N-2}\right). \tag{A.5}$$

In general, the probability of $I_1 = i$ $(1 \leq i \leq w)$ can be expressed as

$$\Pr(I_1 = i) \leq {}_wC_i \prod_{m=1}^{i}\left(1 - q_c^{N-m}\right) \qquad \text{for } 1 \leq i \leq w. \tag{A.6}$$

The PDF for I_1 can be written as

$$P_{I_1}(I_1) \leq \sum_{i=1}^{N-1}\left\{ {}_wC_i \prod_{m=1}^{i}\left(1 - q_c^{N-m}\right)\right\}\delta(I_1 - i) \tag{A.7}$$

where the symbol Π denotes the product.

Appendix B

Numerical explanation of the condition $|CW/n_1| << 1$

In this appendix, we numerically explain the condition $|CW/n_1| << 1$. From Eq. (3.6), when an

image fiber is wound by m turns and by bending radius R', the tensile stress W on the most stressed position $r = D/2$ can be written as

$$W = \frac{2\pi mD/2}{2\pi mR'}E = \frac{D}{2R'}E. \tag{B.1}$$

Therefore, the condition can be expressed as

$$\left|\frac{CW}{n_1}\right| = \left|\frac{CED}{2n_1R'}\right| = 0.106 \times \frac{D}{R'}. \tag{B.2}$$

Here we approximately assumed $n_1 = 1.5$. In general, the picture diameter of an image fiber D is smaller than 3 mm and the minimum bending radius is lager than 30 mm. Therefore, obviously the condition $|CW/n_1| << 1$ is satisfied generally.

Appendix C

Explanation of Eq. (5.1)

In this Appendix, the definition of gain G expressed by Eq. (5.1) is explained. If an EDFA is short enough and unevenness of pumping along the fiber can be neglected, gain G_1 is generally expressed as [12]

$$G_1 = \frac{P_{out}}{P_{in}} = \exp\left[\{\gamma(P_p) - \alpha\}L - \beta\right] \tag{C.1}$$

where P_{out} and P_{in} are output and input signal power of the EDFA, respectively. γ, α, L, and β are the amplification factor for unit length, the loss factor due to absorption and scattering, the length of the EDFA, and the loss at input end, respectively. γ is a function of input pump power P_p. The gain G_1 expressed by Eq. (C.1) can be rewritten as follows:

$$\begin{aligned} G_1 &= \exp(-\alpha L - \beta)\cdot \exp\{\gamma(P_p)\cdot L\} \\ &= C_1 \exp\{\gamma(P_p)\cdot L\} \ . \end{aligned} \tag{C.2}$$

Here, C_1 is a coefficient independent of P_p. From Eq. (5.1), the gain defined by Eq. (5.1) can be expressed written as

$$\begin{aligned} G &= \frac{P_s(\text{with pumping})}{P_s(\text{without pumping})} \\ &= \frac{\exp[\{\gamma(P_p)-\alpha\}L - \beta]P_{in}}{\exp[\{\gamma(0)-\alpha\}L - \beta]P_{in}} \\ &= \exp[\{\gamma(P_p)-\gamma(0)\}L] \\ &= C_2 \exp\{\gamma(P_p)\cdot L\} \ . \end{aligned} \tag{C.3}$$

Here, C_2 is a coefficient independent of P_p. As shown in Eq. (C.3), G is independent of the loss at input end β. Additionally, G is proportional to G_1. Therefore, we can use the definition Eq. (5.1) to test the qualitative gain characteristics of EDFAs and EDIFAs.

Bibliography

[1] M. Ishikawa, "Optoelectronic parallel computing system with reconfigurable optical interconnection," in *SPIE Critical Review Series, Optoelectronic Interconnects and Packaging*, R. T. Chen and P. S. Guilfoyle, eds. Bellingham, WA: SPIE Press, 1996, vol. CR62, pp. 156-175.

[2] F. A. P. Tooley, S. M. Prince, M. R. Taghizadeh, F. B. McCormick, M. W. Derstine, and S. Wakelin, "Implementation of a hybrid lens," *Appl. Opt.*, vol. 34, no. 28, pp. 6471-6480, 1995.

[3] K. Hamanaka, "Optical bus interconnection system using Selfoc lenses," *Opt. Lett.*, vol. 16, no. 16, pp. 1222-1224, 1991.

[4] H. Kosaka, M. Kajita, Y. Li, and Y. Sugimoto, "A two-dimensional optical parallel transmission using a vertical-cavity surface-emitting laser array module and an image fiber," *IEEE Photon. Technol. Lett.*, vol. 9, no. 2, pp. 253-255, 1997.

[5] T. Maj, A. G. Kirk, D. V. Plant, J. F. Ahadian, C. G. Fonstad, K. L. Lear, K. Tatah, M. S. Robinson, and J. A. Trezza, "Interconnection of a two-dimensional array of vertical-cavity surface-emitting lasers to a receiver array by means of a fiber image guide," *Appl. Opt.*, vol. 39, no. 5, pp. 683-689, 2000.

[6] D. M. Chiarulli, S. P. Levitan, P. Derr, R. Hofmann, and B. Greiner, "Demonstration of a multichannel optical interconnection by use of imaging fiber bundles butt coupled to optoelectronic circuits," *Appl. Opt.*, vol. 39, no. 5, pp. 698-703, 2000.

[7] Y. Li, J. Ai, and J. Popelek, "Board-level 2-D data-capable optical interconnection circuits using polymer fiber-image guides," *Proc. IEEE*, vol. 88, no. 6, pp. 794-805, 2000.

[8] M. Nakamura and K. Kitayama, "High-speed 2-D parallel optical interconnects using image fibers with VCSEL/PD arrays," *IEICE Trans. Electron.*, vol. E84-C, no. 3, pp. 282-287, 2001.

[9] S. Nishimura, T. Kudoh, H. Nishi, K. Tasho, K. Harasawa, S. Akutsu, S. Fukuda, and Y. Shikichi, "A high-speed, highly-reliable network switch for parallel computing system using optical interconnection," *IEICE Trans. Electron.*, vol. E84-C, no. 3, pp. 288-294, 2001.

[10] M. Kajita, K. Kasahara, T. J. Kim, D. T. Neilson, I. Ogura, I. Redmond, and E. Schenfeld,

"Wavelength-division multiplexing free-space optical interconnect networks for massively parallel processing systems," *Appl. Opt.*, vol. 37, no. 17, pp. 3746-3755, 1998.

[11] K. Kitayama, "Novel spatial spread spectrum based fiber optic CDMA networks for image transmission," *IEEE J. Selected Areas in Commun.*, vol. 12, no. 4, pp. 762-772, 1994.

[12] M. Nakamura and K. Kitayama, "System performances of optical space code-division multiple-access-based fiber-optic two-dimensional parallel data link," *Appl. Opt.*, vol. 37, no. 14, pp. 2915-2924, 1998.

[13] M. Nakamura, T. Otsubo, and K. Kitayama, "Skew characteristics of image fiber for high-speed 2-D parallel optical data link," *IEEE/OSA J. Lightwave Technol.*, vol. 18, no. 9, pp. 1214-1219, Sep. 2000.

[14] M. Nakamura and K. Kitayama, "Image fiber-optic 2-D parallel optical interconnects based on space-CDMA (invited paper)," *SPIE Photonics WEST*, Optoelectronics'99, Optoelectronic Interconnects VI (San Jose, California), Jan. 1999, / *Proc. SPIE*, vol. 3632, Optoelectronic Interconnects VI, J. P. Bristow and S. Tang, eds. (SPIE Press, Bellingham, Wash., 1999), pp. 331-338.

[15] M. Nakamura, T. Otsubo, and K. Kitayama, "Image fiber skew characteristics," *SPIE Photonics WEST*, Optoelectronics 2000, Optoelectronic Interconnects VII (San Jose, California), Jan. 2000, / *Proc. SPIE*, vol. 3952, Optoelectronic Interconnects VII; Photonics Packaging and Integration II, M. R. Feldman, R. L. Li, W. B. Matkin, and S. Tang, eds, (SPIE Press, Bellingham, Wash., 2000), pp. 66-73.

[16] M. Nakamura, K. Kitayama, Y. Igasaki, and K. Kaneda, "Visual alignment using image fiber micro-optics for long-distance, ultra-high throughput space-CDMA based 2-D parallel optical data link," *The 5th International Conference on Massively Parallel Processing Using Optical Interconnections* (MPPOI'98, Las Vegas, Nevada), pp. 229-236, Jun. 1998.

[17] M. Nakamura and K. Kitayama, "Visual alignment using image fiber coupler for ultra-high throughput space-CDMA based 2-D parallel optical data link," *3rd Optoelectronics and Communications Conference* (OECC'98, Chiba, Japan), 13A2-6, pp. 28-29, Jul. 1998.

[18] M. Nakamura and K. Kitayama, "Image fiber coupler using graded index lenses," *International Topical Workshop on Contemporary Photonic Technologies* (CPT2000, Tokyo, Japan), Tc02, pp. 75-76, Jan. 2000.

[19] M. Nakamura and K. Kitayama, "Image fiber coupler design and its performance," *SPIE Photonics WEST*, Optoelectronics 2001, Optoelectronic Interconnects VIII (San Jose, California), Jan. 2001 / *Proc. SPIE*, vol. 4292, Optoelectronic Interconnects VIII, S. Tang, Y. Li, eds. (SPIE Press, Bellingham, Wash., 2001), pp. 123-130.

[20] M. Nakamura, K. Kitayama, N. Shamoto, and K. Kaneda, "Two-dimensional erbium-doped image fiber amplifier (EDIFA)," *IEEE J. Select. Topics Quantum Electron.*, vol. 7, no. 3, pp. 434-438, May/Jun. 2001.

[21] M. Nakamura and K. Kitayama, "Two-dimensional erbium-doped image fiber amplifier (invited paper)," *The 5th World Multi-Conference on Systemics, Cybernetics and Informatics* (SCI2001, Orlando, Florida), Jul. 2001.

[22] K. Kitayama, M. Nakamura, Y. Igasaki, and K. Kaneda, "Image fiber-optic two-dimensional parallel links based upon optical space-CDMA: Experiment," *J. Lightwave Technol.*, vol. 15, no. 2, pp. 202-212, 1997.

[23] D. T. Neilson and E. Schenfeld, "Plastic modules for free-space optical interconnects," *Appl. Opt.*, vol. 37, no. 14, pp. 2944-2952, 1998.

[24] M. Nakamura, K. Kitayama, Y. Igasaki, and K. Kaneda, "Four-channel, 8 × 8, two-dimensional parallel transmission by use of space-code-division multiple-access encoder and decoder modules," *Appl. Opt.*, vol. 37, no. 20, pp. 4389-4398, 1998.

[25] M. Nakamura, K. Kitayama, Y. Igasaki, and K. Kaneda, "Space-CDMA based 2D parallel optical transmission over record length (100 m) long image fibre," *IEE Electron. Lett.*, vol. 34, no. 11, pp. 1126-1127, May 1998.

[26] M. Nakamura and K. Kitayama, "High-speed 2-D parallel optical interconnects using image fibers with VCSEL/PD arrays," *IEICE Trans. Electron.*, vol. E84-C, no. 3, pp. 282-287, Mar. 2001.

[27] M. Nakamura, K. Kitayama, Y. Igasaki, N. Shamoto, and K. Kaneda, "Image fiber optic space-CDMA parallel transmission experiment using 8 x 8 VCSEL/PD arrays," *Appl. Opt.*, vol. 41, no. 32, pp. 6901-6906, Nov. 2002.

[28] M. Nakamura, K. Kitayama, Y. Igasaki, and K. Kaneda, "Error-free transmission in optical space -CDMA for 2-D parallel data links," *1997 International Topical Meeting on Optics in Computing* (OC'97, Incline Village, Nevada), OThD9, pp. 212-214, Mar. 1997.

[29] M. Nakamura, K. Kitayama, Y. Igasaki, and K. Kaneda, "Four multiplexed, 8x8-bit 2-D Parallel transmission based upon Space-CDMA," *The 4th International Conference on Massively Parallel Processing Using Optical Interconnections* (MPPOI'97, Montreal, Canada), pp. 202-208, Jun. 1997.

[30] M. Nakamura, K. Kitayama, Y. Igasaki, and K. Kaneda, "Visual alignment using image fiber micro-optics for long-distance, ultra-high throughput space-CDMA based 2-D parallel optical data link," *The 5th International Conference on Massively Parallel Processing Using Optical Interconnections* (MPPOI'98, Las Vegas, Nevada), pp. 229-236, Jun. 1998.

[31] M. Nakamura and K. Kitayama, "Error-free transmission of image fiber-optic 2-D parallel interconnection using VCSEL/PD arrays: experiment," *Optical Fiber Communication Conference and Exhibit 2000* (OFC2000, Baltimore, Maryland), ThK2-1, pp. 159-161, Mar. 2000.

[32] P. Prucnal, M. A. Santoro, and T. R. Fan, "Spread spectrum fiber-optic local network using optical processing," *IEEE J. Lightwave Tech.*, LT-4, no. 5, pp. 547-554, 1986.

[33] S. Tamura, S. Nakano, and K. Okazaki, "Optical code-multiplex transmission by gold sequences," *IEEE J. Lightwave Tech.*, vol. LT-3, pp. 121-127, 1985.

[34] J. A. Salehi, "Emerging optical code-division multiple access communications systems," *IEEE Network*, vol. 3, no. 2, pp. 31-39, 1993.

[35] P. E. Green, Jr., Fiber optic networks, New Jersey: Prentice-Hall, Inc., 1993.

[36] J. A. Salehi, "Code division multiple-access techniques in optical fiber networks - Part I: Fundamental principles," *IEEE Trans. Commun.*, vol. 37, no. 8, pp. 824-833, 1989.

[37] J. A. Salehi and C. A. Brackett, "Code division multiple-access techniques in optical fiber networks - Part II: Systems performance analysis," *IEEE Trans. Commun.*, vol. 37, no. 8, pp. 834-842, 1989.

[38] G. Yang and W. C. Kwong, "Two-dimensional spatial signature patterns," *IEEE Trans. Commun.*, vol. 44, no. 2, pp. 184-191, 1996.

[39] K. Koyabu, F. Ohira, and T. Yamamoto, "Fabrication of two-dimensional fiber arrays using microferrules," *IEEE Trans. on Componen., Pack., and Manu. Tech.*, vol. 21, no. 1, pp. 11-19, 1998.

[40] J. M. Sasian, R. A. Novotny, M. G. Beckman, S. L. Walker, M. J. Wojcik, and S. J. Hinterlong, "Fabrication of fiber bundle arrays for free-space photonic switching systems," *Opt. Eng.*, vol. 33, no. 9, pp. 2979-2985, 1994.

[41] A. Sasaki, T. Baba, and K. Iga, "Put-in microconnectors for alignment-free coupling of optical fiber arrays," *IEEE Photon. Technol. Lett.*, vol. 4, no. 8, 1992.

[42] C. M. Miller, "A fiber-optic-cable connector," *Bell Syst. Tech. J.*, vol. 54, no. 9, pp. 1547-1555, 1975.

[43] S. Kawai, Y. Li, and T. Wang, "Skew-free optical interconnections using fiber image guides for petabit-per-second computer networks," *Jpn. J. Appl. Phys.*, vol. 37, no. 6B, pp. 3754-3758, 1998.

[44] A. P. Kanjamala and A. F. J. Levi, "Subpicosecond skew in multimode fibre ribbon for synchronous data transmission," *Electron. Lett.*, vol. 31, no. 16, pp. 1376-1377, 1995.

[45] N. Kashima, "Influence of fiber parameters on skew in single-mode fiber ribbons," *J.*

Lightwave Technol., vol. 15, no. 10, pp. 1858-1864, 1998.

[46] J. Sakai and T. Kimura, "Birefringence and polarization characteristics of single-mode optical fibers under elastic deformations," *IEEE J. Quantum Electron.*, vol. QE-17, no. 6, pp. 1041-1051, 1981.

[47] A. Kirk, A. Goulet, H. Thienpont, N. McArdle, K. Brenner, M Kuijk, P. Heremans, and I. Veretennicoff, "Compact optical imaging system for arrays of optical thyristors," *Appl. Opt.*, vol. 36, no. 14, pp. 3070-3078, 1997.

[48] N. McArdle and M. Ishikawa, "Analysis of GRIN rod and conventional optical systems for imaging of two-dimensional optoelectronic device arrays," *Optics in Computing*, 1997 Tech. Dig. Ser., (OSA, Washington, DC, 1997), pp. 36-38.

[49] J. Ai and Y. Li, "Polymer fiber image guide optical circuits that incorporate free-space add-drop components," *Appl. Opt.*, vol. 38, no. 29, pp. 6167-6175, 1999.

[50] J. Ai, J. Popelek, and Y. Li, "Beam-splitting ball lens: a new integrated optical component," *Opt. Lett.*, vol. 24, no. 21, pp. 1478-1480, 1999.

[51] C. Tombling, T. Saitoh, and T. Mukai, "Performance predictions for vertical-cavity semiconductor laser amplifiers," *IEEE J. Quantum Electron.*, vol. 30, no. 11, pp. 2491-2499, 1994.

[52] R. Lewén, K. Streubel, A. Karlsson, and S. Rapp, "Experimental demonstration of a multifunctional long-wavelength vertical-cavity laser amplifier-detector," *IEEE Photon. Technol. Lett.*, vol. 10, no. 8, pp. 1067-1069, 1998.

[53] J. W. Goodman, "Introduction to Fourier Optics," McGRAW-HILL Book Company, 1968.

[54] E. Desurvire, "Erbium-doped fiber amplifiers: principles & applications," New York: John Wiley and Sons, 1994.

[55] G.-C. Yang and T. Fuja, "Optical orthogonal codes with unequal auto- and cross-correlation constraints," *IEEE Trans. Inform. Theory*, vol. 41, pp. 96-106, 1995.

[56] Y. Li, T. Wang, H. Kosaka, S. Kawai, and K. Kasahara, "Fiber-image-guide-based bit-parallel optical interconnects," *Appl. Opt.*, vol. 35, no. 35, pp. 6920-6933, 1996.

[57] Y. Ohiso, Y. Kohama, and T. Kurokawa, "0.85-μm vertical-cavity surface-emitting laser array grown on GaAs and AlGaAs substrates by metal organic chemical vapor deposition," *Jpn. J. Appl. Phys.*, vol. 34, no. 11, pp. 6073-6078, 1995.

Abbreviations

1-D	One-dimensional
2-D	Two-dimensional
ASE	Amplified Spontaneous Emission
BER	Bit Error Rate
BS	Beam Splitter
CDMA	Code Division Multiple Access
ECL	Emitter-Coupled Logic
EDFA	Er-Doped Fiber Amplifier
EDIFA	Er-Doped Image Fiber Amplifier
FOP	Fiber Optic Plate
FWHM	Full Width at Half Maximum
GRIN	Graded Index
hcp	hexagonal close packed
IF	Image Fiber
LC	Liquid Crystal
LD	Laser Diode
LED	Light-Emitting Diode
lp	line pairs
NA	Numerical Aperture
NRZ	Nonreturn to Zero
OOC	Optical Orthogonal Code
OOSP	Optical Orthogonal Signature Pattern
PD	Photo Diode
PDF	Probability Density Function
PPG	Pulse Pattern Generator
PRBS	Pseudorandom Binary Sequence

SIR Signal-to-Interference noise Ratio

SLM Spatial Light Modulator

SOA Semiconductor Optical Amplifier

VCSEL Vertical-Cavity Surface-Emitting Laser

Related publications by the author

[Papers]

(1) M. Nakamura and K. Kitayama, "System performances of optical space code-division multiple-access-based fiber-optic two-dimensional parallel data link," *OSA Appl. Opt.*, vol. 37, no. 14, pp. 2915-2924, May 1998.

(2) M. Nakamura, K. Kitayama, Y. Igasaki, and K. Kaneda, "Four-channel, 8 × 8 bit, two-dimensional parallel transmission by use of space-code-division multiple-access encoder and decoder modules," *OSA Appl. Opt.*, vol. 37, no. 20, pp. 4389-4398, Jul. 1998.

(3) M. Nakamura, K. Kitayama, Y. Igasaki, and K. Kaneda, "Space-CDMA based 2D parallel optical transmission over record length (100 m) long image fibre," *IEE Electron. Lett.*, vol. 34, no. 11, pp. 1126-1127, May 1998.

(4) M. Nakamura, T. Otsubo, and K. Kitayama, "Skew characteristics of image fiber for high-speed 2-D parallel optical data link," *IEEE/OSA J. Lightwave Technol.*, vol. 18, no. 9, pp. 1214-1219, Sep. 2000.

(5) M. Nakamura and K. Kitayama, "High-speed 2-D parallel optical interconnects using image fibers with VCSEL/PD arrays," *IEICE Trans. Electron.*, vol. E84-C, no. 3, pp. 282-287, Mar. 2001.

(6) M. Nakamura, K. Kitayama, N. Shamoto, and K. Kaneda, "Two-dimensional erbium-doped image fiber amplifier (EDIFA)," *IEEE J. Select. Topics Quantum Electron.*, vol. 7, no. 3, pp. 434-438, May/Jun. 2001.

(7) M. Nakamura, K. Kitayama, Y. Igasaki, N. Shamoto, and K. Kaneda, "Image fiber optic space-CDMA parallel transmission experiment using 8 x 8 VCSEL/PD arrays," *OSA Appl. Opt.*, vol. 41, no. 32, pp. 6901-6906, Nov. 2002.

[Proceedings of international conferences]

(1) M. Nakamura, K. Kitayama, Y. Igasaki, and K. Kaneda, "Error-free transmission in optical space -CDMA for 2-D parallel data links," *1997 International Topical Meeting on Optics in Computing* (OC'97, Incline Village, Nevada), OThD9, pp. 212-214, Mar. 1997.

(2) M. Nakamura, K. Kitayama, Y. Igasaki, and K. Kaneda, "Four multiplexed, 8x8-bit 2-D Parallel transmission based upon Space-CDMA," *The 4th International Conference on Massively Parallel Processing Using Optical Interconnections* (MPPOI'97, Montreal, Canada), pp. 202-208, Jun. 1997.

(3) M. Nakamura, K. Kitayama, Y. Igasaki, and K. Kaneda, "Visual alignment using image fiber micro-optics for long-distance, ultra-high throughput space-CDMA based 2-D parallel optical data link," *The 5th International Conference on Massively Parallel Processing Using Optical Interconnections* (MPPOI'98, Las Vegas, Nevada), pp. 229-236, Jun. 1998.

(4) M. Nakamura and K. Kitayama, "Visual alignment using image fiber coupler for ultra-high throughput space-CDMA based 2-D parallel optical data link," *3rd Optoelectronics and Communications Conference* (OECC'98, Chiba, Japan), 13A2-6, pp. 28-29, Jul. 1998.

(5) M. Nakamura and K. Kitayama, "Image fiber-optic 2-D parallel optical interconnects based on space-CDMA (invited paper)," *SPIE Photonics WEST*, Optoelectronics'99, Optoelectronic Interconnects VI (San Jose, California), Jan. 1999, / *Proc. SPIE*, vol. 3632, Optoelectronic Interconnects VI, J. P. Bristow and S. Tang, eds. (SPIE Press, Bellingham, Wash., 1999), pp. 331-338.

(6) M. Nakamura and K. Kitayama, "Image fiber coupler using graded index lenses," *International Topical Workshop on Contemporary Photonic Technologies* (CPT2000, Tokyo, Japan), Tc02, pp. 75-76, Jan. 2000.

(7) M. Nakamura, T. Otsubo, and K. Kitayama, "Image fiber skew characteristics," *SPIE Photonics WEST*, Optoelectronics 2000, Optoelectronic Interconnects VII (San Jose, California), Jan. 2000, / *Proc. SPIE*, vol. 3952, Optoelectronic Interconnects VII; Photonics Packaging and Integration II, M. R. Feldman, R. L. Li, W. B. Matkin, and S. Tang, eds, (SPIE Press, Bellingham, Wash., 2000), pp. 66-73.

(8) M. Nakamura and K. Kitayama, "Error-free transmission of image fiber-optic 2-D parallel interconnection using VCSEL/PD arrays: experiment," *Optical Fiber Communication Conference and Exhibit 2000* (OFC2000, Baltimore, Maryland), ThK2-1, pp. 159-161, Mar. 2000.

(9) M. Nakamura and K. Kitayama, "Image fiber coupler design and its performance," *SPIE Photonics WEST*, Optoelectronics 2001, Optoelectronic Interconnects VIII (San Jose, California), Jan. 2001 / *Proc. SPIE*, vol. 4292, Optoelectronic Interconnects VIII, S. Tang, Y. Li, eds. (SPIE Press, Bellingham, Wash., 2001), pp. 123-130.

(10) M. Nakamura and K. Kitayama, "Two-dimensional erbium-doped image fiber amplifier (invited paper)," *The 5th World Multi-Conference on Systemics, Cybernetics and Informatics* (SCI2001, Orlando, Florida), Jul. 2001.